The Effect of CaO on Magnesium and Magnesium Calcium Alloys

Doctoral Thesis
(Dissertation)

to be awarded the degree
Doctor of Engineering (Dr.-Ing.)

submitted by

Björn Wiese M. Eng.

from Eckernförde, Germany

approved by the Faculty of Natural and Materials Science,
Clausthal University of Technology

Date of oral examination
09.05.2016

Dean:	Prof. Dr. rer. nat. Winfried Daum
Chairperson of the Examination Board:	Prof. Dr. rer. nat. Albrecht Wolter
Supervising tutor:	apl. Prof. Dr.-Ing. Rainer Schmid-Fetzer
Reviewer:	Prof. Dr.-Ing. Karl Ulrich Kainer

Acknowledgements

I am greatly thankful for the technical and scientific support from all colleagues at Helmholtz-Zentrum Geesthacht.

Firstly, I would like to thank my supervisor Dr.-Ing. Norbert Hort, for giving me the opportunity to work on this topic, as well as for the guidance, patience and helpful discussions throughout my PhD.
The Federal Ministry for Economic Affairs and Energy (BMWi) for funding the project MagHyM 20K1107B (BMWi-Verbundprojekt MagHyM – Entwicklung und Charakterisierung von Mg-Al-Hybridwerkstoffen für Korrosions- und brandresistente Kabinenbauteile für Verkehrsflugzeuge), which provide me the frame for my doctoral thesis.

Many people contributed to my doctoral thesis over the last three years. Especially, I would like to thank:

- My reviewers, Prof. Dr.-Ing. Rainer Schmid-Fetzer at TU Clausthal (Institute of Metallurgy - Thermochemistry & microkinetics) and Prof. Dr.-Ing. Karl Ulrich Kainer Magnesium at Helmholtz Zentrum (Innovation Center MagIC) to supporting me in my doctoral thesis.
- My colleague, Dr. Chamini L. Mendis for co-reviewing the thesis, as well as for her comment, guidance, support and motivation.
- My colleague, Dr. Domonkos Tolnai for co-reviewing the thesis, as well as for his comment, guidance and support.
- Prof. Dr.-Ing. Rainer Schmid-Fetzer and Dr. Artem Kozlov from the TU Clausthal (Institute of Metallurgy - Thermochemistry & microkinetics) for the nice and successful collaboration on the thermodynamic calculations of the Mg-Ca-O system.
- The technicians, Gert Wiese, Petra Fischer, Günter Meister and Alexander Reichart, for all help in the labs.
- My Prof. from the Fachhochschule Flensburg, reviewer of the Bachelor and Master Thesis and now college, Prof. Dr.-Ing. Michael Dahms for his support, comment, rating and motivation.
- My bachelor student, Elias Sakkal, who worked with me on the BMWi project MagHyM.
- My colleagues, Juliano Soyama, Gabor Szakacs, Cesar Augusto Stüpp, Ricardo Buzolin, Marta Mohedano, Maria D. Constantino, Martin Holm, and some more, for the nice time and cooperation in the Helmholtz-Zentrum Geesthacht.

I wont to acknowledge the Deutsches Elektronen-Synchrotron (DESY) for the provision of synchrotron radiation facilities within the framework of three proposals at the PETRA III.
Proposals No. at DESY:

- I-20120285
- I-20120743
- I-20130330

However, on my way to this thesis, some non scientific history should be acknowledgement.

If I think about my school / training / study time, I remember three for my important teaching staffs:

- Jürgen Todt (teacher from the school).
- Mr. Ewen (teacher from vocational school), for the recommendation, that I should study mechanical engineering.
- Prof. Dr.-Ing. Michael Dahms, that he has aroused my interest in materials engineering.

Lastly, my family, without their support, I would not have come this far.

Danke Papa, dass Du für meine Schwester und mich, alles ermöglicht hast, was Dir möglich war. Auch wenn es für Dich als Alleinerziehender nicht immer einfach war.

Vielen Dank

ABSTRACT

CaO ist ein preiswerter Ersatz für Ca als Legierungselement in Mg-Legierungen. Als Legierungselement wird CaO bereits in den sogenannten ECO-Mg-Legierungen (Environment COnscious magnesium / Umweltbewusstes Magnesium) eingesetzt. In der Literatur wird berichtet, dass sich CaO in Mg auflöst. Jedoch besteht keine Theorie die das Auflösen von CaO in Mg erklärt. Der Effekt von Ca auf das Oxidationsverhalten von Mg ist seit längerer Zeit bekannt so wie im Zusammenhang mit den sogenannten ECO-Mg-Legierungen. Wie Ca oder CaO dabei in der Oxidschicht der Mg-Ca-Legierungen miteinander interagieren, konnte bisher noch nicht geklärt werden.

Diese Arbeit untersucht die Hypothese, dass die Stabilität von CaO und MgO in den gebräuchlichen Ellingham-Diagrammen nicht ausreichend dargestellt ist. Die experimentelle *in situ*-Synchrotron-Untersuchung während des Schmelzens und des Erstarrens in Verbindung mit thermodynamischen Berechnungen zeigen, dass das ΔG der Oxidation von Ca und Mg im gesamten Mg-Ca-O-System betrachtet werden muss und nicht nur die störchometrischen Reaktionen. Es zeigte sich bereits, dass Mg in der Lage ist, CaO im festen Zustand zu reduzieren, welches im Gegensatz zur allgemein beschreibenden Ansicht steht. Die *in situ*-Experimente wurden an dem Mg-xCaO und dem Mg-xCa-6CaO System durchgeführt. In diesen Experimenten konnte das Auflösungsverhalten der Phasen während des Aufschmelzens und die Phasenbildung während der Erstarrung verfolgt werden. Die Versuchsergebnisse der Erstarrungsreihenfolge konnten durch die thermodynamischen Berechnungen bestätigt werden. Diese Berechnungen wurden auf der Grundlage von verschiedenen Literaturwerten für die thermodynamischen Daten von CaO und MgO durchgeführt, um das ternäre Mg-Ca-O Phasendiagramme zu berechnen. Basierend auf den thermodynamischen Berechnungen wurde eine Theorie entwickelt, wie Ca in der Oxidschicht wirken könnte. Die Theorie stützt sich auf der Idee, dass sich ein Pilling-Bedworth-Verhältnis (PBV) aus der Kombination von MgO und CaO einstellt. Dieses beruht auf Annahme der Bildung einer Oxidschicht aus CaO auf reinem Mg (PBV > 1) und MgO auf reinem Mg (PBV < 1). Bei einem Volumenanteil von CaO höher als 0.49 in der Oxidschicht, berechnet sich ein PBV von > 1.

ABSTRACT

CaO is used as a cheap replacement for Ca addition to addition in Mg. CaO as an alloying element are used in the ECO-Mg (Environment COnscious magnesium) alloys. The CaO dissociation in Mg is reported in literature, but with out a theory that can which explain the dissociation of CaO in Mg alloys. The effect of Ca on the oxidation resistance was known for long time and also observed from ECO-Mg. However an explanation on how Ca or CaO is incorporated into the oxide layer of Mg-Ca has not been clarified.

This thesis investigate the hypothesis that the stability of CaO and MgO in the commonly used Ellingham diagram is not accurately described. The *in situ* synchrotron radiation diffraction experimental investigation of the melting and solidification and thermodynamic calculation show, that the change of Gibbs free energy ΔG must be considered for the entire Mg-Ca-O system and not only the stoichiometric reactions. This investigation shows that Mg reduces CaO even in solid state, which is the opposite of the commonly ascribed view. The *in situ* experiments were performed on the Mg-xCaO and Mg-xCa-6CaO systems. It was possible to follower the dissociation of the phases during melting and the phase formation during the solidification. The experimental results from the solidification sequence were used to validate the thermodynamic calculations. A number of different literature values of the thermodynamic data of CaO and MgO were used to calculate the ternary phase diagram Mg-Ca-O. Based on the thermodynamic calculations a theory was developed, on how Ca is incorporated in the oxide layer. The theory used the idea of a Pilling–Bedworth ratio (PBR) for CaO on pure Mg (PBR > 1) and the MgO on pure Mg (PBR < 1). At a volume fraction of CaO higher as 0.49 in the oxide layer forms with a PBR of > 1.

Contents

CHAPTER 1

Introduction

Ca increases the oxidation resistance of Mg alloys at elevated temperatures up to 645 $°C$ with a Ca concentration of 0.2 $wt.\%$. Investigations on the oxidation behaviour of Mg-Ca alloys report, an increase in the elevated temperature oxidation resistance but use different experimental set-up to investigate the oxidation of Mg-Ca alloys. The reasons behind this effect is not well understood. The Standard Gibbs free energy (ΔG) of CaO is higher than of MgO and should remain an inert oxide that enhance protection from the oxidation Mg. However, the investigations show that CaO is less stable than MgO in the Mg rich corner of the ternary Mg-Ca-O system, which change theoretical basis for the protective nature of CaO. The Pilling–Bedworth ratio (PBR) of Ca/CaO is lower than of Mg/MgO so that this cannot be used to explain the increase in oxidation resistance. The explanation for the improvement in high temperature oxidation is that Ca increase the density of the oxide layer, but the exact nature of this is not fully understood. The oxidation resistance and the mechanical properties at elevated temperature are important for the high temperature resistant Mg alloys. This can increase the temperature range for applications of Mg alloys. It will also give the opportunity make Mg products safer in the field of transportation where fires can occur.

An other approach is the use CaO as an cost efficiency alloying addition for Mg alloys, as a replacement for Ca. However, the investigation on *ECO-Mg (Environment COnscious magnesium)* do not provide a theory, which explain the dissociation of CaO in Mg alloys. However, investigations show that CaO dissociate up to a certain amount in Mg alloys,

which indicates also that the CaO is less stable than MgO in the Mg rich corner of the Mg-Ca-O system.

For the investigation of the phase transformation between a Mg alloy and CaO, standard technique e.g. differential scanning calorimetry (DSC) or differential thermal analysis (DTA) are not useful to follow the phase transformations. This technique using for the detection of the phase transformation the energy provides a good temperature resolution, but does not provide information on the phase evocation. If some phase transformation occur at a similar temperature, e.g. $CaO + 3Mg \longrightarrow MgO + 2Mg + Ca \longrightarrow MgO + Mg_2Ca$, it is not possible to distinguish between these reactions.

An experimental set-up that follow the phase transformations with a useful time and temperature resolution is the *in situ* experiments using X-ray synchrotron radiation diffraction. The results from this type of investigation provide the information involved during the dissociation of CaO during the heating and the effect of CaO on the solidification of Mg and Mg-Ca alloys. This shows the interaction between Mg and Ca and their oxides and which phases occur during this process, which help to understand the dissociation of CaO.

CHAPTER 2

Aims and objectives

Previous investigations show that CaO dissociate in the presence of molten Mg. These investigations show that CaO is reduced by Mg or Mg-Al alloys, but do not explain the exact mechanisms behind this reduction. Kondoh et al. [1] considered the role of Laves phases in the dissociation of CaO in Mg. This theory is based on the reduction of CaO by Mg and relates to the formation of the Laves phase Mg_2Ca. The enthalpy of mixing also play an important role together with the change in standard Gibbs free energy (ΔG) of the phase formation. The other problem with this theory is the large deviation between ΔG of MgO and CaO, the highest deviation was investigated by Gourishankar et al. [2]. Gourishankar et al. [2] investigated the MgO and the CaO positions in the Ellingham diagram and found that they should be interchanged, and use this change in Ellingham diagram to explain the protective effect observed in Mg-Ca alloys.

The aim of this work is to show the interactions between Mg and Ca and their oxides, when it occurs and its their roles during melting and solidification. The experimental investigation was conducted with *in situ* synchrotron radiation diffraction. This is used to determine the temperature range and the state (whether liquid or solid) in which the dissociation of CaO occurs and which phases form during this process. The experimental data is compared with the thermodynamic calculations to evaluate and to improve the thermodynamic parameters of the Mg-Ca-O system. The thermodynamic calculations are conducted in collaboration with the Institute of Metallurgy - Thermochemistry & Microkinetics group in TU Clausthal.

This will show:

- Information on the phases formation or transformation sequence driving the CaO dissociation.
- A different theory different from the effect of the ΔG, will be proposed to explain the CaO dissociation.

The *in situ* diffraction experiments were performed with Mg-xCaO and Mg-xCa-yCaO systems, which will provide an experimental basis the influence of CaO on Mg and Mg-Ca alloys. This will lead to a better understanding of the Mg-Ca-O system to understand the effect of Ca on the oxide layer formation and the way Ca protect Mg alloys.

CHAPTER 3

State of the Art

3.1 Magnesium with Calcium and Calcium Oxide

3.1.1 Magnesium

Magnesium (Mg) is classified as an alkaline earth metal. It is in the group 2 of the periodic table, like Be, Ca, Sr, Ba and Rd. In the periodic table it is listed with the atomic number 12 with a atomic weight of 24.31 u ($4.0359 \cdot 10^{-26}$ kg). The crystal structure of Mg is hexagonal close-packed (hcp) (Space group: P63/mmc) (Fig. 3.1) with a lattice parameters of $a = 0.32092$ nm and $c = 0.52105$ nm [3]. The ratio between a and c is 1.6236 which is close to the ideal ratio of 1.633 for a close-packed hexagonal structure. [3–5]

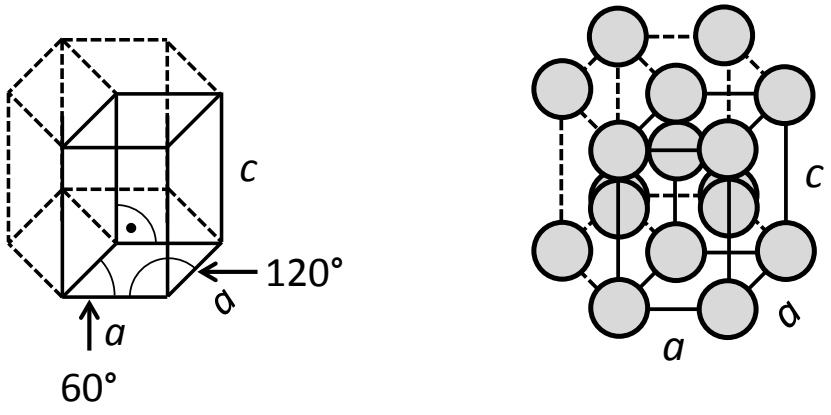

(a) Mg cell (b) Mg cell with atoms

Fig. 3.1: a) Unit cell of hcp Mg and b) Mg cell with atoms.

Properties of Mg in comparison with other metals are listed in Tab. 3.1 for room temperature (RT). Due to the crystal structure it is the difficult to deform Mg during processing, in comparison with metal of other crystal structures, e.g. body-centered cubic (bbc) or face-centered cubic (fcc). The homogeneous deformation require more than 5 independent slip systems as provided by von Mises [6], but Mg has only 3 slip systems and 2 are dependent at RT so deformation is accommodated by twinning. Above 225 $°C$ [4, 7] more slip systems are activated in Mg and the main deformation mechanism is no longer twinning. The low ductility of Mg at room temperature is related to the twining, due

low number of independent slip systems available. [3–5]

The following properties are considered to be disadvantageous for Mg in structural applications [3, 8]:

- Low elastic modulus compared with other structural metals (E),
- relatively low deformability (below 225 $°C$ [4,7]), limited cold workability and toughness,
- relatively low creep resistance,
- and relatively high corrosion rate (high chemical reactivity).

Tab. 3.1: Mg in comparison with other metals [9, 10]

Properties	Unit	Mg	Al	Ca	Ti	Fe
Density	$\frac{g}{cm^3}$	1.74	2.7	1.54	4.5	7.87
Melting point	$°C$	650	660	180	1670	1536
Hardness	HV	30-45	21-41	17	120-200	103
Tensile strength	MPa	98-245	39-117	55-115	290-740	192-245
Yield strength	MPa	90-230	10-98	14-85	180-390	98
Youngs modulus	GPa	45	68	20	112	206
Crystal structure		hcp	fcc	fcc	hcp	bbc

Mg, like many other metals, is used in alloyed state as pure Mg does not satisfy requirements of a structural metal. [10]

3.1.2 Mg-Ca alloys

Ca increases the strength of Mg alloys by grain refining, solution strengthening and dispersion strengthening by formation of the Laves phase Mg_2Ca [4, 11–13]. Ca also increase the deformability (rollability) with addition up to 0.3 $wt.\%$ [3].

Ca increased the oxidation resistance of Mg alloys at high temperatures up to 645 $°C$ with a Ca concentration of 0.2 $wt.\%$ [14]. The oxidation resistance and the mechanical properties at high temperature are important for high temperature Mg alloys, as this can increase the temperature range for Mg alloy applications. Ca additions will also make Mg products safer in field of transportation where fires can occur. [8]

The corrosion rate at ambient temperature increase with Ca [8, 15]. Compared with the corrosion rate, the effect of Ca on the density is low [5,8,16]. Ca addition > 0.8 $wt.\%$ can decrease the castability of Mg alloy. Ca increase the reaction between the steel moulds and the melt (tendency to stick), which decrease the usability of Mg-Ca alloys for die casting. With the increment of Ca the tendency to form hot cracks also increases. [3, 8]

However, the biggest advantage of Ca for alloying is the increase in mechanical properties at high temperature. For applications at high temperature, especially creep resistance is important. Mg and Ca form a temperature stable Laves phase Mg_2Ca. Ca in combination with other alloying elements also form stable phases. [3, 17, 18]

A relatively new field of Mg alloys is the use of Mg alloys as biodegradable materials. Ca is a important metallic trace element of the metabolism in a human body, followed by Mg which is also a metallic trace element in human body. This is the basis for the development of biodegradable materials based on the Mg-Ca system. According to Gu et al. [19, 20] and Rad et al. [16] the Mg-xCa alloy show good biocompatibility. The challenge for this type of alloys is to tailor the property profile on corrosion/degradation rates for a use as biodegradable implant material. [16, 19–21]

Commercially available Ca containing alloys are *ECO-Mg (Environment COnscious magnesium)* [22–24] prepared with CaO or *Non-flammable magnesium alloy* [25] containing Y in combination with Ca. It is also used in the MRI alloys (MRI 230D (Mg-Al-Ca-Sr-Sn) and MRI 153M (Mg-Al-Ca-Sr) alloys) developed by Dead Sea Magnesium Ltd. for high temperature applications [26].

3.1.3 Mg-Ca system

The early work on the Mg-Ca system was conducted by Barr [27] at 1911 and Páris [28] at 1937. These studies are revisited in the most recent studies. A collection of the relevant studies on the Mg-Ca system are shown in the Tab. 3.2. The Tab. 3.2 shows the significant points of the Mg-Ca system with phase formation temperatures.

Mg-Ca system forms a stable intermetallic phase, with C14 Laves structure a with chem-

Tab. 3.2: Selection of significant points of the Mg-Ca system from literature. (x) specified values, (y) experimental values from the graphs and (C) calculated values.

Reaction	Ca-content $[at.\%]$	T $[°C]$	Literature	Remarks
L → Mg (hcp)	0	650	Chase [29]	(x)
Melting	0	649.3	Aljarrah [30]	(C)
L → Ca (bcc)	100	842	Chase [29]	(x)
Melting	100	841.2	Aljarrah [30]	(C)
Ca (bcc) → Ca (fcc)	100	443	Chase [29]	(x)
allotropic transformation	100	442.5	Aljarrah [30]	(C)
L → Mg_2Ca + α-Ca (fcc)	69.14	446	Baar [27]	(y)
Eutectic	73.42	445	Páris [28]	(y)
	67	445	Haughton [31]	(y)
	73	442	Klemm [32]	(y)
	73	445	Nayeb-Hashemi [33]	(C)
	73	442	Aljarrah [34]	(C)
	-	445	Vosskühler [35]	(y)
L → Mg_2Ca + α Mg (hcp)	12.25	518	Baar [27]	(y)
Eutectic	11.05	525	Páris [28]	(y)
	10.49	517	Haughton [31]	(y)
	10.56	516	Vosskühler [35]	(y)
	10.5	516.5	Nayeb-Hashemi [33]	(C)
	10.56	514	Aljarrah [30]	(C)
	-	516	Nowotny [36]	(y)
L → Mg_2Ca	33.33	718	Baar [27]	(y)
Melting	33.33	725	Páris [28]	(y)
	33.33	714	Vosskühler [35]	(y)
	33.33	715	Nayeb-Hashemi [33]	(C)
	33.33	714	Aljarrah [30]	(C)

ical composition Mg_2Ca [32,37,38]. This intermetallic phase separate the Mg-Ca system to a double eutectic system (Fig. 3.2). The first investigation of Barr [27] and Páris [28] show a higher Ca content, than the current investigations. The stoichiometric composition Mg_2Ca was determined by Voßkühler [35] at 1937. The investigations on this system assume that that Mg_2Ca Laves phase is a point phase, but Nowotny et al. [36] and Klemm et al. [32] predict existence of range compositions for Mg_2Ca. However, this extended range is inconsistent, and discussed by Klemm et al. [32] in reference to Nowotny et al. [36]. Today thermodynamic calculations has been performed with the Mg_2Ca Laves phase with and without a composition range, but this is still under discussion. [30, 39–43]

The higher Ca content of Mg_2Ca from Baar [27] and Páris [28] shifted the Mg-Ca system to higher Ca contents. Recent studies [31, 32, 35] on Mg-Ca system takes in to account the melt loss of Ca. The composition of the samples are thus determined after the thermal treatment of the experiments. This was conducted by Voßkühler [35] and Haughton [31] and show, compared with the early investigations, a lower Ca content for the liquidus line. The investigation of Klemm et al. [32] confirm the results of Haughton et al. [31]. This is the reason that for calculations e.g. from Nayeb-Hashemi and Clark 1987 [33] and Agarwal et al. 1995 [34] the results form Baar [27] and Páris [28] were not considered, but the results of Vosskühler [35], Haughton [31] and Klemm [32] has been.

The maximum solid solubility of Ca in Mg was determined to be between 0.43 $at.\%$ (0.71 $wt.\%$) and 1.1 $at.\%$ (1.8 $wt.\%$) at the eutectic temperature of 516 $°C$. The solid solution of Ca in Mg is shown in Fig. 3.2(b) in the Mg rich side of the Mg-Ca system with experimental data and thermodynamic calculations (the full line are calculated with Pandat 8.1 with the PanMagnesium 8 database). Two regions of solid solution lines can be identified. The experimental results of Vosskühler [35] and Burke [45] are more reliable. Vosskühler's [35] investigation is based on a heat treatment of different alloy compositions under different temperatures. Burke's [45] investigations show comparable values of the solid solution, but his experimental method is different. He investigated the volume content of Mg_2Ca of number of Mg-Ca alloys after the heat treatment. The content of Ca is plotted with the volume content of Mg_2Ca and the interpolation at a

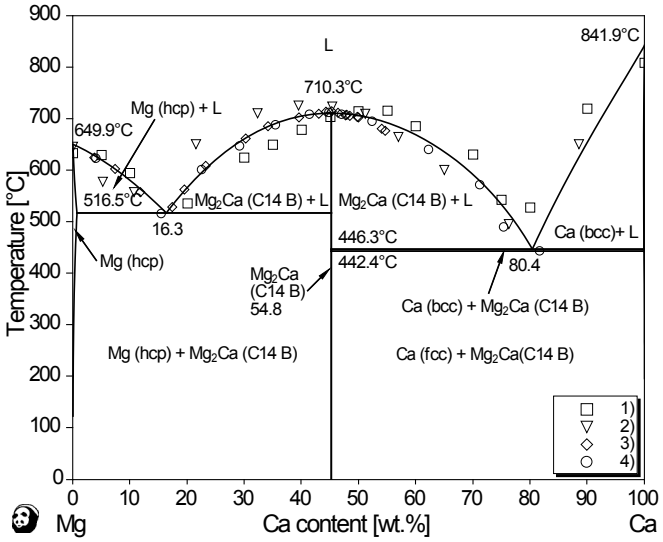

(a)

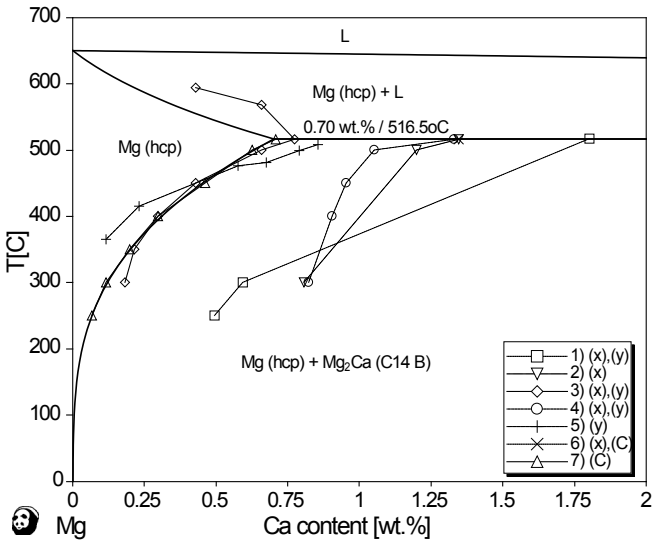

(b)

Fig. 3.2: *Mg-Ca* system phase diagram calculated with Pandat^{TM}8.1 software with PanMagnesium 8 database. a) in comparison with literature values for the liquid-line of 1) Baar [27], 2) Páris [28], 3) Vosskühler [35] and 4) Klemm [32]). b) in comparison with literature values of the solid state solubility of *Ca* in *Mg* from 1) Haughton [31], 2) Nowotny [36], 3) Vosskühler [35], 4) Bulian [44], 5) Burke [45], 6) Nayeb-Hashemi [33] and 7) Aljarrah [30] for a *Ca* concentration up to 2 *wt.*%. x) specified values, y) experimental values from the graphs and (C) calculated values. The full line are calculated with Pandat 8.1 with the PanMagnesium 8 database.

given temperature gives the maximum amount of Ca in solid solution.

Due to the high melt loss potential of Ca the production of alloys with a high content Ca of is difficult. This can explain the limited investigations on the Ca rich side of the Mg-Ca (50 to 100 $wt.\%$ Ca) system. Another reason for this is the high affinity of Ca to oxygen [27].

3.1.4 Physical properties of CaO

CaO is the oxide of Ca and it has the same crystal structure as MgO. The crystal structure is based on $NaCl$ (Space group: Fm-3m) with a lattice parameter of 0.48 nm. CaO, like MgO, is hydrophilic and reacts with H_2O to $Ca[OH]_2$. If CaO react to $Ca[OH]_2$ the density change from 3.32–3.35 g/cm^3 to 2.08–2.30 g/cm^3, this lead to an increase in volume by 2.75 times. [46] To dry $Ca[OH]_2$ to CaO a temperature of approximately 512 $°C$ [47] necessary. Dissociation of $Ca[OH]_2$ was first reported in 1956 [48] during this thermal dissociation process CaO_2 a peroxide or dioxide form. According to literature CaO_2 dissociate below 300 $°C$ [46]. The formation of CaO_2 is reported in the literature [48, 49] and the process of drying $Ca[OH]_2$ to produce CaO_2 is patented [50] for technical applications.

3.1.5 Interaction between CaO and MgO

According to the Ellingham diagram CaO is more stable than MgO at low temperatures [51,52], therefore, it is expected that CaO remains unreacted during melting of Mg. This means that in a simple binary reaction the standard Gibbs free energy ΔG is lower for CaO than for MgO at low temperatures, e.g. [51, 52]. Howerver, Gourishankar et al. [2] measured the enthalpies and ΔG for CaO and MgO. This work derived new values for the standard enthalpies of the formation at 298 K of CaO and MgO, namely, is -602 and -635 kJ/mol. This a deviation from the JANAF [52] $+33$ kJ/mol for CaO and -34 kJ/mol for MgO. This is important as MgO and CaO swap the positions in the Ellingham diagram. The Tab. 3.3 list different thermochemical values of CaO and MgO

based on the publications [2, 52–54].

Tab. 3.3: Different thermochemical values for CaO and MgO based on the literature Chase 1985 [52], Binnewies 2002 [53], Hillert 1989 [54] and Gourishankar 1993 [2].

Reference	[52] 1985	[53] 2002	[54] 1989	[2] 1993
CaO	-646345	-646489	-632143	-602000
MgO	-609536	-609220	-609635	-635000
	ΔG $[J/mol]$ at 298.15 K (25 $°C$)			

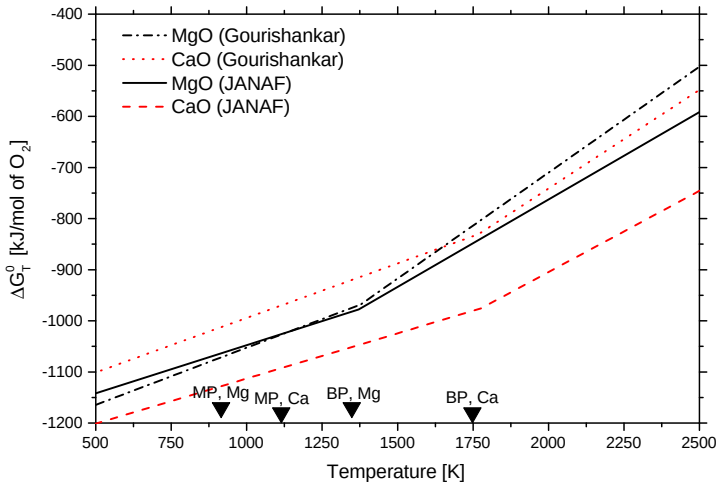

Fig. 3.3: Difference between in the ΔG for MgO and CaO from JANAF [52] and Gourishankar et al. [2] datas replotted in one Ellingham diagrams taken from Gourishankar et al. [2].

The idea to use CaO as an alloying addition for Mg alloys came from the group of Shae K. Kim in Korea [22, 23]. However, the publications from this group do not provide a theory, which explain the dissociation of CaO in Mg alloys. [14, 23, 55–65]

Investigations on the oxidation behaviour of Mg-Ca alloys report, an increase in the high temperature resistance but the quantitative effect on the experimental conditions [14, 59, 65]. These investigations use different experimental set-up to investigate oxidation of Mg-Ca alloys. The formation energy (ΔG) of CaO is higher than of MgO and should remain an inert oxide that enhance protection from the oxidation Mg. However, Gourishankar et al. [2] found that CaO is less stable than MgO, which change mechanism the protective associated with nature of CaO. The PBR of Ca/CaO is lower than of Mg/MgO so that this cannot be used to explain the increase in oxidation resistance. The explanation for

the increment of the high temperature oxidation is that Ca increase the density of the oxide layer, but the exact nature of this is not fully understood [65].

Kondoh et al. [1] proposed a calculation to explain the dissociation of CaO in Mg-Al alloys. They used the standard Gibbs free energy for the reaction between pure Mg and CaO Eq. 3.1 - 3.2 and Mg-Al and CaO using Eq. 3.3. This calculation take in to account of all the reaction products not just oxides from the oxidation of CaO. In this case Mg will reduce CaO and form MgO (Eq. 3.1) the change of ΔG is positive. However, this calculation does not take in to account the effect of enthalpy of mixing on the effect the actual phase formation. If the formation of Laves phases for Mg-CaO-system (Eq. 3.2) or Mg-Al-CaO-system (Eq. 3.3) was considered, the ΔG is lower than that for the starting condition. Kondoh et al. [1] calculated the standard Gibbs free energy from the Ellingham diagram values (Fig. 3.4(b)) for different temperatures, Fig. 3.4(b). They [1] used the thermodynamic data from Barin (1977) [51] and Knacke (1991) [66] in their calculations. Small deviations in the ΔG for the single phase formations change the ΔG for the system. However, the Tab. 3.3, it is not clear how large is the difference between MgO and CaO. Gourishankar et al. [2] proposed that they swap positions in the Ellingham diagram, Fig. 3.3.

$$Mg + CaO \Longrightarrow MgO + Ca + \Delta G \tag{3.1}$$

$$3 \cdot Mg + CaO \Longrightarrow MgO + Mg_2Ca + \Delta G \tag{3.2}$$

$$2 \cdot Al + Mg + CaO \Longrightarrow Al_2Ca + MgO + \Delta G \tag{3.3}$$

The melting point of pure CaO is 2327-2899 $^{\circ}C$ [46, 54, 68, 69, 71] and pure MgO is 2597-2827 $^{\circ}C$ [46, 54, 68, 69, 71]. In the binary MgO-CaO system the melting point decrease to an eutectic temperature of between $2280-2360$ $^{\circ}C$ [68, 70]. The calculated binary MgO-CaO system are illustrated in Fig. 3.5, from Serena et al. [67].

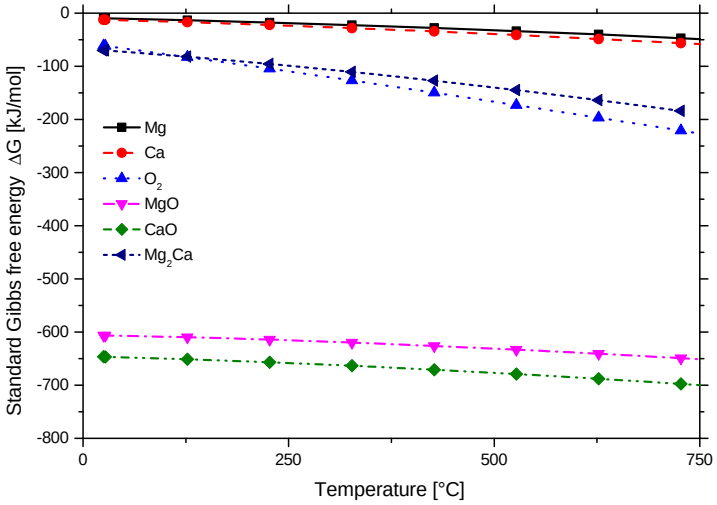

(a)

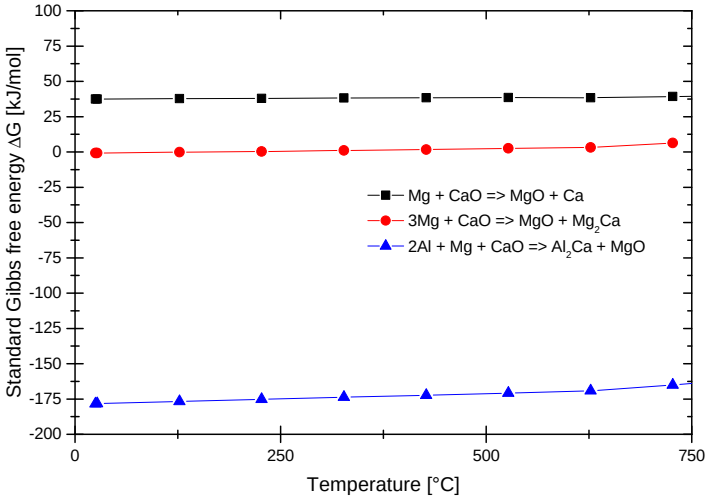

(b)

Fig. 3.4: Release of ΔG in (a) binary reactions and (b) the reaction that take in acount the formation of the Laves phases. Kondoh et al. [1].

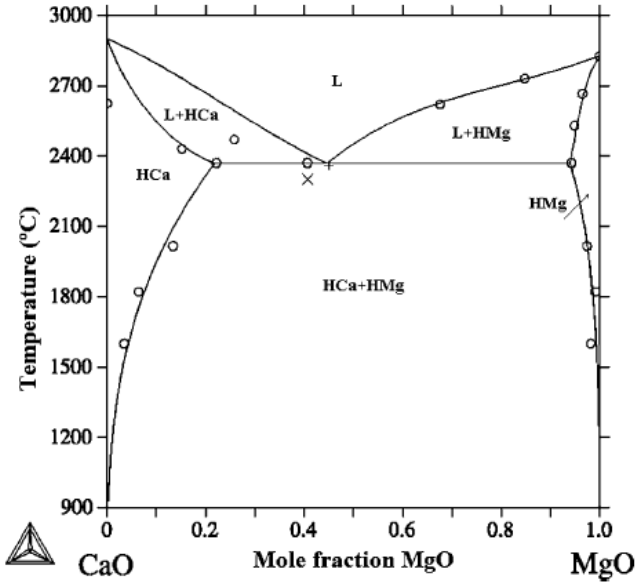

Fig. 3.5: The calculated binary MgO-CaO system from Serena et al. [67] with data from ∘ Doman et al [68], × Rankin and Merwin [69] and + Ruff et al. [70]. HCa = CaO as Halite and HMg = MgO as Halite.

3.2 High Temperature Oxidation

The definition of high temperature oxidation is oxidation at an elevated temperature without water. The region of high temperature oxidation start at a temperature T > 100 $°C$. In relation to corrosion at high temperature, the oxidation is defined as the reaction between a metal and oxygen. However, this is a technical definition and deviates from the chemical definition of oxidation. The high temperature oxidation includes not just O also other elements e.g. N or S and describes the oxidation of the metal to its ionized state [72, 73].

3.2.1 Ellingham diagram

The Ellingham or Richardson diagrams (in the following only Ellingham diagram) is a type of graph which shows the stability of compounds in relation to the partial pressure and temperature. The Ellingham diagrams provide information on the change in Gibbs free energy for oxidation (ΔG) (Fig. 3.6) of the reaction between a metal and the O, N or S (depending on the environment) as a function of temperature at a given pressure. Eq. 3.4 is the function for ΔG, which depend on the enthalpy (H) and the entropy (S). The H is a fixed value at a given temperature and pressure for a phase and describe the release of energy during the reaction between the metal and the oxygen. However, the change in ΔG depends on the $-T \cdot \Delta S$, if the temperature increases the ΔG decrease. This is related to the increase in entropy with the temperature. The ΔG can be plotted as a function of temperature in relation to the reference of 1 Mol e.g. O_2 or N_2 at 1 bar.

$$\Delta G = \Delta H - T \cdot \Delta S \tag{3.4}$$

The free energy at a given temperature (position in the diagram) gives information on the stability of oxide, nitride or sulphide in relation to the metal. Also the partial pressure can be included in the Ellingham diagram, which provide information in about the partial pressure range where the phases are stable. For an example the ΔG as a function of the

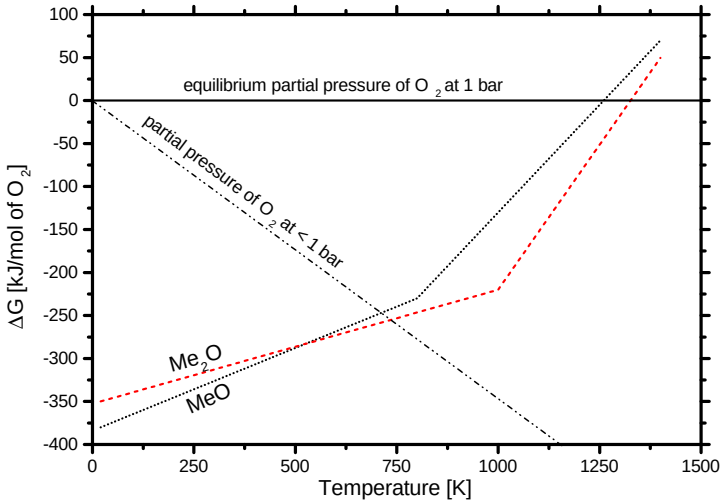

Fig. 3.6: Difference between in the ΔG of MeO and Me_2O plotted in one Ellingham diagram .

temperature for MeO and Me_2O are plotted in to a Ellingham diagram (Fig. 3.6). Up to a temperature of approximately 520 $°C$ MeO is more stable than Me_2O, due to the lower ΔG. Both oxides are show a linear increase in ΔG up to a phase change. The enthalpy (H) is depends on the phases present, if the oxide under goes a phase transformation, H and entropy (S) will change e.g. melting, vaporising etc. If a phase cross the zero line from the reference phase of 1 Mol of O_2 in this case, the reference phase (O_2) is more stable than the oxide. The reference line moves with the partial pressure. If the pressure < 1 bar the reference line moves down, as illustrated in Fig. 3.6, or pressure > 1 bar up.

3.2.2 Thermodynamics kinetics and their effect on reaction speed

The thermodynamics together with the kinetics determine the stability, sequence and structure of the oxide layers at high temperatures. [72, 74]

The thermodynamics is the driving force for the reaction. The first tool in the high temperature oxidation is the thermodynamics to estimate the stability of metals and oxides, for this purpose the Ellingham diagram is an important tool. However, this tool gives no information on the enthalpies of mixing in a system with more than one oxide. The change in enthalpy of mixing can change the structure of the oxide layer, if more than one oxide of one or more metals involved in the oxidation process. [72, 74]

The kinetics explains the speed of the oxidation, so that the kinetics define the growth rate of the oxide layer. Kinetic is defined as a combination of reaction speed and the mobility of the reacting species. [72]

ΔG is the driving force for a reaction, if the ΔG higher, then the reaction speed r increases. However, the ΔG is constant at a given temperature and only affected by the composition. [72]

The kinetics is a function of the temperature at constant free activation energy ΔG^a, shown in the Fig. 3.7. The reaction speed r increase with the temperature and also with a lower ΔG^a. If the ΔG too high the reaction is inhibited, this can reduce the possibility of this reaction. Under this condition a reaction will not occur, even if the reaction release a high amount of energy. The possibility for a reaction increases exponentially with the temperature. This relation is given by the Arrhenius function and describes, the relation between temperature and ΔG^a with the reaction speed r as follows: [72, 74]

$$r = r_0 \cdot e^{-\frac{\Delta G^a_{(mol)}}{R \cdot T}} \tag{3.5}$$

- r_0 Proportional constant of the reaction speed
- R Universal gas constant (8.314 $\frac{J}{K \cdot mol}$)
- $\Delta G^a_{(mol)}$ Change in free activation enthalpy per mol.

3.2.3 Diffusion during oxidation process

Diffusion in general describe the movement of atoms (e.g. ion or molecule). The diffusion is a thermally activated process that strongly depends on the temperature, this connection of temperature and diffusion rate is coupled by the Arrhenius function (Eq. 3.5). Quantitative diffusion is described by the Ficks law (Eq. 3.6) and it gives a value for atoms that move in one direction. Ficks law can only applied to binary systems, as the chemical activity can be different for each component in a system. Therefore the diffusion flux J by the chemical potential μ should be considered. [72, 74, 75]

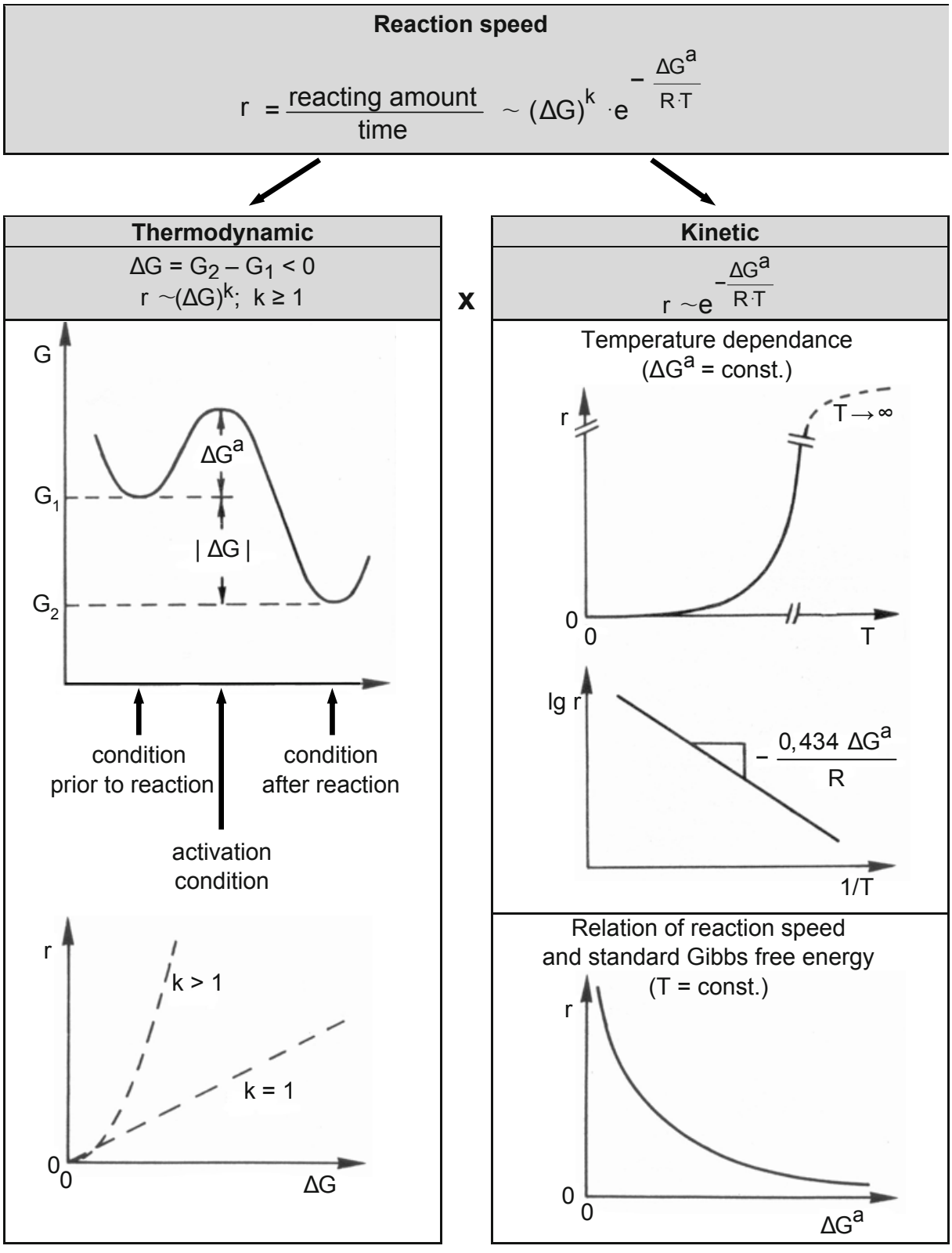

Fig. 3.7: Relation between thermodynamic and kinetic parameters on the reaction speed r and temperature related processes [72].

$$J = -D\frac{dc_D}{dx} = -D\frac{dc_D}{RT}\frac{d\mu}{dx} \tag{3.6}$$

- J Diffusion flux
- D Diffusion coefficient
- c_D Concentration
- x Distance
- μ Chemical potential

The diffusion is related to the distance an atom can travel in a given time through the bulk material. The classification of diffusion is defined by the system in which the diffusion occurs. Self diffusion occurs in a pure material or homogeneous system where a static movement of atoms occurs. In an inhomogeneous system the diffusion has a direction, and the local chemical composition change with the movement of the atoms. The second case is important in technical systems e.g. alloys or oxide layers. The driving force in a heterogeneous material is to minimize the energy by achieving a constant distribution of elements in the system. e.g. in alloys or oxide compositions. Depending on the stability of phases in such a heterogeneous system, it is possible that stable phases can form or grow, because this will result in a lower energy state than a constant distribution of elements. [72, 74]

In the case of oxidation the diffusion of O to the metal or metal to O play an important role in the oxidation speed of metals or alloys. If the oxide layer is dense and without cracks, it will inhibit further oxidation.

3.2.4 Pilling–Bedworth ratio

The theory on the oxide layer or protection layer formation on metals was established in 1923 by Pilling and Bedworth [76]. They invented an equation to estimate the oxidation

behaviour at high temperature. The Pilling–Bedworth ratio (PBR) explain the high temperature oxidation behaviour of different metals and their oxides [72,76]. The PBR is the ratio between the molar volume of oxide in relation to the molar volume of metal, shown in Eq. 3.7. The Eq. 3.7 represents the molar volume change through to the formation of the oxide at the interface to the metal. This volume change is used to explain possible stress generation in the oxide layer. The stress developed in this oxide layer can reach a maximum stress at a critical layer thickness. The calculated PBR indicate if tensile or compressive stress is expected in the oxide layer. For PBR < 1 a tensile stress is expected and the oxide layer cracks, this indicate that the oxide layer is not stable, as a result is not protective. If the PBR $= 1$ no stress occurs in the oxide layer and the layer is protective. Where PBR > 1 a compressive stress expected and the oxide layer is dense, this indicate that the oxide layer is stable and protective as a result. If the PBR $>> 1$ the compressive stress is to high and oxide chips will drop from the metal/oxide interface. These three cases are illustrated in the Fig. 3.8 Tab. 3.4 shows the PBR values of some metals [72, 74, 76].

- PBR Pilling–Bedworth ratio,
- M molar mass,
- n_m number of metal atoms per one molecule of the oxide,
- ρ density,
- V molar volume.

$$PBR = \frac{V_{oxide}}{V_{metal}} = \frac{M_{oxide} \cdot \rho_{metal}}{n_m \cdot M_{metal} \cdot \rho_{oxide}} \tag{3.7}$$

Change of weight for various PBR on the oxidation is shown in Fig. 3.9. The best oxide layer is dense and has a good interface between metal and oxide, this is the cases of PBR ≥ 1. Such a oxide layer reduces the oxidation speed with increased oxide thickness, this leads to a parabolic growth of the oxide layer. If the PBR $>> 1$ the oxide cracks and lets in

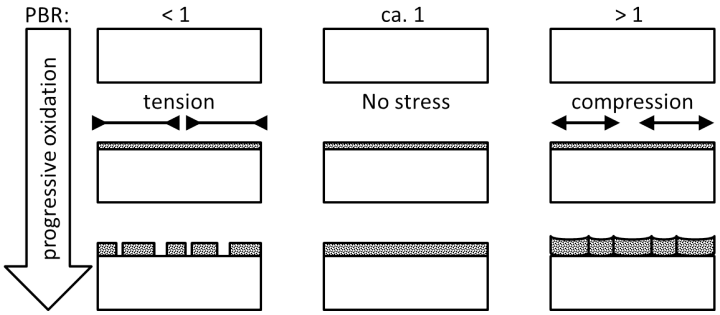

Fig. 3.8: Evolution of the oxide layer for PBR < 1, ≈ 1 and > 1 [72, 76].

Tab. 3.4: Pilling-Bedworth-Ration (PBR) of different metals with the PBR of the oxides of this metal [72, 76]. * Pilling and Bedworth from 1923 [76]. ** calculation based on crystallographic data from [77].

Oxide	CaO	MgO	Al_2O_3	ZrO_2	NiO	FeO	TiO_2
PBR	*0.78 / **0.63	*0.84 / **0.81	$Fe(Fe,Cr)_2O_4$. 1.28	1.65	1.65	1.7	1.73
Oxide	CoO	Cr_2O_3	$Fe(Fe,Cr)_2O_4$. $FeCr_2O_4$	SiO_2	Ta_2O_5	Nb_2O_5	
PBR	1.86	2.05	2.1	2.15	2.5	2.68	

oxygen, which can easily reach the metal, this lead to a parabolic oxidation at the begins with a strong increase in the oxidation speed after breaking off of oxide chips. Equally if the PBR < 1 the oxidation speed does not decrease, as the oxidation progresses cracks forms in the oxide layer and this let oxygen reach the metal. The oxidation behaviour in this case is a linear weight increase. The worst case for the oxidation under high temperature conditions is a linear weight loss. This happens when the oxide at this temperature is liquid or gaseous. The kinetics of oxide growth is mainly correlated with diffusion. When the oxide layer grows the oxidation speed decrease in the presence of dense oxide layer, as the O anion and the metal ions have to diffuse through the oxide layer driven by the ΔG of the reaction. [72, 73, 76, 78]

If the PBR $\neq 1$ this leads to a stress in the oxide layer and the base metal. For a PBR < 1 a tensile stress is observed in the oxide layer and compressive stress in the metal, if the PBR > 1 the stresses swap for oxide layer and the base metal. [72, 73, 79]

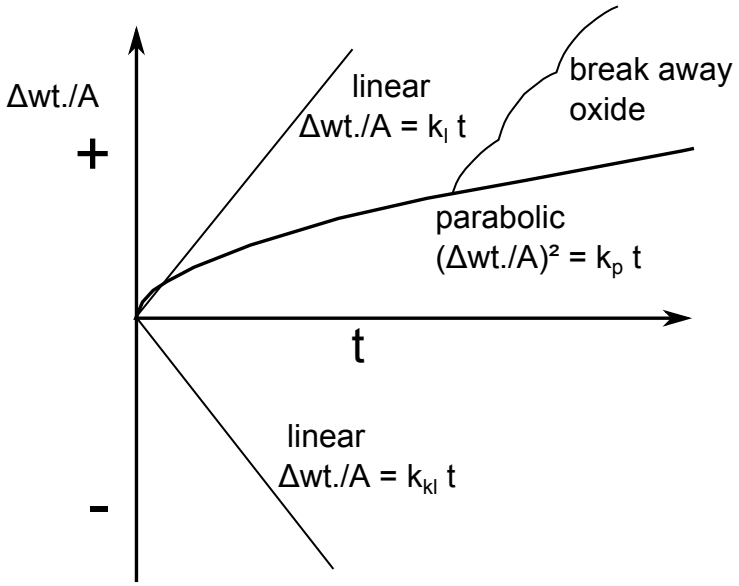

Fig. 3.9: The change in weight for three different cases of PBR during the oxidation process [72] for Mg (PBR < 1), Al (PBR > 1) and Ta (PBR $>> 1$).

3.2.5 Thermodynamic and kinetic related layer formation

The layer structure depends on the thermodynamic and kinetic processes, that takes over during the oxidation. The kinetic of the diffusion and the thermodynamic driving force determine the sequence of the oxide layer growth. The theory on parabolic growth of the oxide layer are proposed by Wagner [78] for a dense oxide layer. This theory can be applied for thin oxide layers, if the PBR < 1 but only at the initial state of oxidation. The Wagner model for a parabolic growth of a oxide layer for a metal oxide describes based on whether the layer grows on the metal side or on the gas side. The growth direction is based on the mobility the O_2 anions or metal cations through the oxide layer (Fig 3.10). The mobility of the anions and cations are related to the defect structure of the oxides. This directly influence the parabolic constant of growth k_p in the oxidation process (Fig. 3.9). The driving force according to Wagner for the oxide layer growth is the partial pressure of oxygen between metal-oxide interface and oxide-gas interface. [72–74, 78, 80]

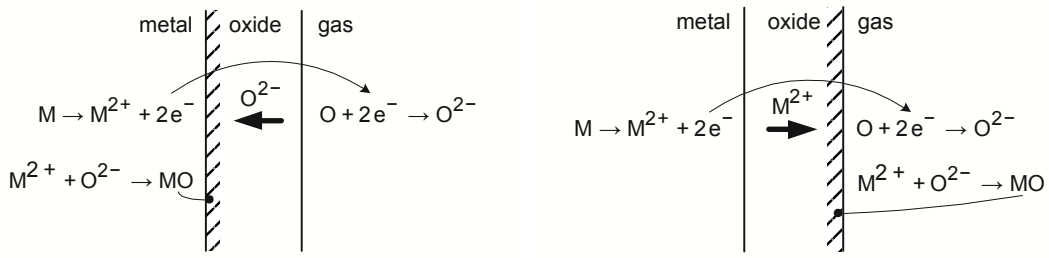

(a) A (b) B

Fig. 3.10: Wagner's model of oxide layer formation depending on the mobility of the O_2 anions or metal cations: a) faster mobility the O_2 anions and b) faster metal cations than the anions. [72, 78].

3.2.6 Oxidation of alloys

The oxidation of pure metals are governed by the factors described above, but in case of alloys additional effects needs to be take in to account. These additional effects for the oxidation of alloys are [72, 73]:

- Different alloying elements have a different attractions to O_2 ($\Delta G_A \neq \Delta G_B$).
- The activity and the concentration of alloying additions contributes to changes in ΔG of the system.
- Differences in diffusion coefficient ($D_A \neq D_B$).
- The oxide layer is composed of different oxides.

In the case of a binary system with the elements A and B most common the oxide layer forms as illustrated in Fig. 3.11. Fig. 3.11(a) shows the major contribution to the formation of the protective oxide from element B. Below the oxide layer the alloy become impoverished of B. This impoverishment plays no role if B diffuse fast and the oxide layer grows slowly. This ideal oxidation system works under the following conditions [72, 73]:

- B-oxide is more stable than A-oxide ($\Delta G_B < \Delta G_A$).
- The amount of B is high enough to form a protective layer.

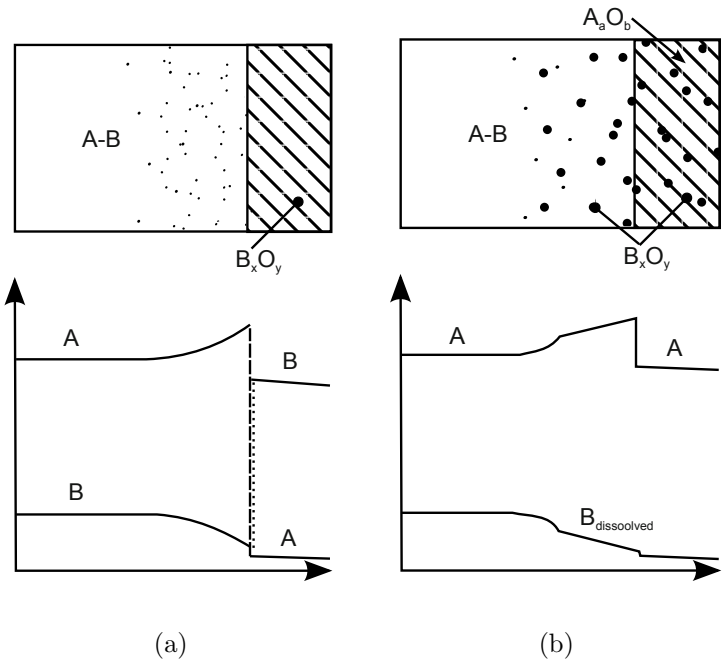

Fig. 3.11: The oxide layer formation on binary system with the alloying elements A and B: a) as protective B oxide layer and b) A oxide as protective layer with internal B oxide. [72]

The Fig. 3.11(b) shows the case that the B content is not high enough or close to the impoverishment limit of B, to form a protective layer. In this case major oxide layer composed of A, which grows faster and is less protective. If the activity of B (ΔG_B) high enough, to form B oxides, and the partial pressure for B lower is than that of A, B oxide form in and below the A oxide (internal oxide). [72, 73]

A collection of additional layer structures for A-B alloy system is described in Wood [73] and Anžel [81].

3.2.7 Protective oxide layer on alloys

In general most or all elements in an alloy contribute to the protective oxide layer formation. In metallic systems the miscibility of the oxide can result in forming different systems of oxides, as described below [72, 73]:

- No solid solution of the oxides (A_xO_y and B_zO_v),
- mixed oxide ($(A, B)_xO_y$)

- and formation of a new type of oxide (AB_2O_3 mainly form as spinel type oxide).

The oxide layer composition and sequence at a given temperature can be taken from a isothermal section of a phase diagram, when the oxidation processes reach the steady state condition [73]. When, a binary A-B alloy form of only B_xO_y oxide layer, Xu [79] proposed a method to calculate the PBR for this single oxide. When the system has more than one oxide, this method can not be applied.

3.2.8 Oxidation of Mg alloys on high temperature

The high temperature oxidation of Mg alloys is important during the casting or thermo-mechanical treatment. The general mechanism of high temperature oxidation is explained in Section 3.2. This section focus on the specific behaviour of Mg and Mg alloys at high temperature.

The oxidation of pure Mg at high temperatures does not form a protective layer (exlained in Section 3.2.4). Due to the lower volume of the MgO to the volume of the Mg, the oxide layer develops cracks and corrosive gases can react with Mg. Fournier et al. [82] observed that the growth of the oxide at 300 $°C$ follows the inverse logarithmic/parabolic law (similar to Fig. 3.8 b) with PBR ≈ 1). He reported that at and above 400 $°C$ the oxidation rate of Mg increases considerably. From 400 $°C$ Mg evaporates and forms MgO nodules on the surface by reacting with oxygen. Emley [4] concluded that up to 450 $°C$ Mg form a very thin protective layer or film, and above 450 $°C$ the layer become porous and no protective. It is important to protect Mg during high temperature processes, e.g. hot deformation or welding. The high reactivity of Mg means, that it can ignite and endanger the workers and the production line. In the case of Mg parts, the environment, the size, the shape, the exposed temperature and the exposure time determine if a Mg part maybe ignited. The time to ignition or if an alloy may be ignited depend on the alloy composition and the microstructure. [83–85]

The alloying elements can reduce the oxidation potential and increase the oxidation resistance of the solid and/or liquid Mg [86, 87]. Listed below are some alloying elements

which are reported to successfully reduce the oxidation and improve ignition resistance of Mg:

- Be [4, 65, 83, 84, 88–90, 90–92]
- Ca [4, 14, 55, 59, 86, 88, 93, 94]
- CaO [14, 22–24, 56–58, 61–63, 65, 94]
- Rare earth elements e.g.: Nd [83, 95, 96], Gd [86, 97], Ce [86, 98], Pr [86], Sm [86], Dy [86], Er [86] and in mischmetal [91]
- Y [55, 86, 97–100]
- Sr, Si and La [86]
- Zn, Sn, Ni, Cu, In, Ag and Tl [83].

However, an explanation on how these alloying elements are incorporated into the oxide layer of the Mg alloys has not proposed. Some theories exist on the effect of these alloying elements on the ignition resistance, which are not verified or are contradictory between investigations.

The improvement in the ignition resistance is explain by the formation of thermodynamically stable oxide phases containing alloying elements with a PBR > 1 [83, 86, 87]. This is similar to the high temperature oxidation of metals, as described in Section 3.2.4. For rare earth addition this concept can be used to explain the interaction of the alloying elements during the oxidation process. However, other alloying elements, e.g. Ca and Sr, show a PBR < 1, but provide protection. Sr does not form a thermodynamically more stable oxide compared with Mg and still provide protection. In an investigation from 1953 [101], Mg-Al-Be and Mg-Al-Ca-Be alloys was molten in air without ignition. Thus, the role of Ca on the oxidation resistance was known for long time [102]. However, an explanation on how Ca or CaO is incorporated in to the oxide layer of Mg-Ca has not been clarified. Sakamoto et al. [102] reported that the ignition point increased with Ca additions over the melting point of Mg by adding up to 1 $wt.\%$ Ca. They reported that

the oxide film on the Mg–Ca consists of CaO surface film and below this is a mixture of MgO–CaO. However, Sakamoto et al. [102] did not clarify why this CaO protective film can form on a molten Ca-bearing Mg alloy. Similar results are reported by Ha et al. [14, 58] on the oxide layer of Mg-Ca and Mg-CaO alloys. However, the main reason behind this protection effect is not clarified. The leading hypothesis is based on the PBR, thermodynamic stability of oxide layer or the kinetic of the diffusion and reaction on the oxide layer formation.

Ce and Si do not form a thermodynamically stable oxide compared with MgO, but PBR of the Ce and Si oxides is > 1 and form protective layer better than MgO [86]. The protection of the binary Mg alloys thouge alloying addition is not fully understood and the thermodynamics of the simple oxidation reaction ($xM + yO \Longrightarrow M_xO_y + \Delta G$) should take in to account the enthalpy of mixing and the secondary phase formation. This will contribute to the understanding of complex systems. Fan et al. [98] investigated Mg-Y and Mg-Y-Ce alloys and found that the oxide layer is mainly Y_2O_3, and Ce_2O_3 is not observed. However, if Ce (5 $wt.\%$ Ce / ignition point 647 $°C$) added without Y the ignition resistance increase, but not as large increase as with the addition of Y (3.8 $wt.\%$ Y / ignition point 660 $°C$). The addition of Y and Ce in combination (3 $wt.\%$ Y and 0.68 $wt.\%$ Ce / ignition was not detected up to 900 $°C$) show a significantly higher increase in ignition point in air. The kinetics of the possible reaction and the diffusion of different alloying elements (Wagner [78]) affect the oxide formation (Section 3.2.5) and was also reported Czerwinski [83] for the oxidation of Mg. The ongoing research of Fan et al. [103] consider the oxide layer formation on the melt of the Mg-Y-Ce alloys (3 $wt.\%$ Y and 0.68 $wt.\%$ Ce / no ignition up to 900 $°C$) and proposed a theory on the oxidation kinetics in the layer formation theory. They showed that the outer layer contained a mixture of Y_2O_3 and $Ce_{0.202}Y_{0.798}O_{1.601}$, and the inner layer is mainly Mg and MgO with a little amount of Y_2O_3. This shows an enrichment of RE-containing oxides on top of the Mg alloy melt, which provides improved ignition resistance.

The improved ignition resistance of Mg system is related to a denser or closed oxide layer. At present there is no theory to explain how these alloying additions density the oxide

layer. The approach of using highly reactive metals to improve the oxidation resistance of Mg alloys, Section 3.2.7, is a hypothesis that has not been investigated [104].

3.2.9 Melt protection of Mg alloys

The high affinity of Mg to oxygen and the high vapour pressure of molten Mg [5, 105], makes it necessary to prevent oxidation and burning during Mg production. During the fabrication of Mg, different technologies are used to reduce or prevent the oxidation during melting. This type of oxidation result in the ignition of the melt; which is difficult to handle and is a safety issue. For safe handling of Mg different technologies were developed. It is possible to separate this in 4 groups.

1. pure element powders, e.g. S [4, 5, 106]
2. fluxes, such as salt [3, 4, 106–109] and minerals [4, 106, 108],
3. cover, shielding or protection gases [4, 5, 92, 106, 110–115],
4. or by alloying elements [4, 106], that form a stable layer on the melt.

Beck [5] reported that pure S powder was used as the earliest protective medium for Mg. It was suggested that a MgS formed a protection layer on the Mg melt, which prevent further oxidation. [4, 5, 106]

After this, liquid salt fluxes were used for the Mg melt protection [3–5, 106–109], to separate the melt form the ambient air. The fluxes contain low melting point eutectic compounds and the ingredients of the fluxes are listed in Tab. 3.5. This technology was able to provide a safe handling of Mg melt, but the disadvantages of the fluxes include the detrimental effect on the quality of the casting, equipment and specific boundary for the casting process. The fluxes are not only used to protect the melt from ignition, but also prevent Mg evaporation. The evaporation of Mg change the actual composition of Mg alloy and the condensation of Mg can create safety issues as small Mg crystals can sublimate in colder places in the cast facility and ignite. A small operating temperature range available for fluxes and flux is retained within the ingots, which limits the effectiveness

of the flux. Flux remains in the cast product reduces the quality of the casting and the salt fluxes contaminate the ingots. This contamination increases the corrosion rate of the cast products. The flux also contaminate the scrap, which makes recycling difficult. The most components of commercial fluxes are hydrophilic, after the removal from the casting facility, during the remelting process, this can lead to gas evolution. This gas evolution is extremely dangerous and endangers workers and the cast shop. The melt protection with fluxes lead to multiple issues. Fluxes increase the corrosion of casting equipment is also a reason for the Mg producers avoid using flux in the production. The S and fluxes are highly corrosive and limit the endurance of the casting equipment. Cl-containing salts were a common flux components, and subsequently produce of HCl gas, which is highly corrosive and detrimental to operator health. Emley [4] explained the mechanisms associated with fluxes for the Mg production in more detail. [3, 106–108, 116]

Tab. 3.5: Components of various protective and refining ingredients used in protective fluxes. [3, 4, 107, 108]

Protective base, wt.%						
$MgCl_2$	$CaCl_2$	$NaCl$	KCl			
Inspissation (viscous) agents, $wt.\%$						
$BaCl_2$	BaF_2	MgF_2	CaF_2	MgO	SiO_2	C

The protection gases were used in the beginning in combination with fluxes. These gases prevent ignition of Mg melt. [3, 4, 92, 107, 110, 117] The cover (also called shielding or protection) gas, overcome the disadvantages of fluxes on the Mg casting. The gases could be active, in that the gas react with the Mg melt and form a layer that protect the melt from a direct contact with air and reduce the evaporation of Mg. The second group of protection gases are inert gases like Ar or gases that show low or slow interaction with the Mg melt like N_2 or CO_2. The inert gases are used mostly as a carrier gas for active gases. The active gases have the advantage, that they form a layer on Mg melt. In case of a air draught or re-filling Mg in to the melt the active gases provide short time protection from oxidation up to ignition. A list of different protection gases are shown in Tab. 3.6. The active gases show a higher impact on the Global Warming Potential (GWP) compared with CO_2.

Tab. 3.6: Chemical compounds and names of different protection gases. [3, 92, 107, 110, 117, 118]

	Chemical compounds and names	Atmospheric lifetime [yre]	Global Warming Potential (GWP) in a time period of 100 yrs
Active gas	SF_6	3,200	23,900
	SO_2	several days	0
	$HFC134a$ (CF_3CH_2F)	14.6	1,300
	$HFE7100$ $(C_4F_9OCAH_3)$	no values	390
	$Novec^{TM}612$ $(C_3F_7C(O))$	0.014	≈1
	CH_4	12	24
	N_2O	120	no values
Active gas (experimental)	BF_3	no values	no values
	SO_2F_2	no values	≈1
Carrier Gas	Ar	-	-
	He	-	-
	N_2	-	-
	$dry\ air$	-	-
	CO_2	100 - 150	-

The most commonly used active gases in Mg production are SO_2, $HFCs$ and SF_6 [3, 92, 110, 117]. A small volume of (0.01 to 5.0 $vol.\%$) active gases are used together with the carrier gases. The composition of the protection gases used in the Mg casting process are mostly based on the experience in the cast shop: the casting process, the alloy, the equipment and on economic parameters. The choice for the carrier gases is based mainly on the availability and the cost.

The reasons in keeping the amount of active gas low as possible include:

- High price,
- highly corrosive properties of the gases,
- high Global Warming Potential (GWP) and
- health and safety of the workers.

These points are not applicable for all active gases. The disadvantages of active protection gas is similar to the disadvantages of flux. Gas (as SO_2, HFCs and SF_6) or the reaction product are highly corrosive to the steel used for casting equipment and limit the endurance of the equipment. [3, 92, 108, 119, 120]

The first active gas used in combination with fluxes was SO_2. The problem with SO_2 is that it is highly corrosive to the equipment and it reacts with water to form H_2SO_3. H_2SO_3 can damage the skin and lungs [46]. The impact on the GWP is 0 for SO_2, which make it unique in the group of active gases (Tab. 3.6) [120]. However, the corrosion of the equipment and low Threshold Limit Value (TLV), for exposure to H_2SO_3 (1.5 $\frac{mg}{m^3}$ in germany), makes it unsuitable [3, 46, 92, 106, 108, 119, 121, 122]. The protection of the melt works by a reaction between SO_2 and the Mg melt and which forms protection layer on the melt. Possible reactions in the SO_2 protection system are shown in Eq. 3.8 and 3.9 for N_2 as a carrier gas [109, 119, 123]. In case of CO_2 as a carrier gas, it will form C on the surface, which is comes from the reaction in Eq.3.10 [123].

$$Mg_{(l)} + O_2 + SO_2 \Longrightarrow MgSO_{4(s)} \tag{3.8}$$

$$MgSO_{4(s)} + 4Mg_{(l)} \Longrightarrow 4MgO_{(s)} + MgS_{(s)} \tag{3.9}$$

$$2Mg_{(l)} + CO_2 \Longrightarrow 2MgO_{(s)} + C_{(s)} \tag{3.10}$$

SO_2 protection gas works well while there is oxygen available, if no oxygen available, e.g. in a closed melting system, no protection is provided [121,124]. The possible reaction proposed is shown in Eq. 3.11, there Mg reduces SO_2 [109,119]. Wang and Xiong [121,124] found that the content of air was important during the use of SO_2 as protection gas for AZ91D. They reported that in the beginning the protection layer is composed mostly of MgO and MgS, but over time the content of $MgSO_4$ increases. MgS interacts with O_2 in the carrier gas and provide the melt protection through the formation of $MgSO_4$.

$$Mg_{(l)} + SO_2 \Longrightarrow MgO_{(s)} + (S + SO + S_2O) \tag{3.11}$$

SF_6 was first used in 1977 for the melt protection of Mg. H.J. Müller [107] reported, that SF_6 was used as an experimental gas for the melt protection. Due to the negative impact on the greenhouse effect, the use of fluorinated greenhouse gases likely to be prohibited from 2050 in European Union in general. The Article 13 in the *(EC) No 842/2006* [118], allow to the use of SF_6 below 850 $\frac{kg}{year}$, for the magnesium die-casting and in recycling of magnesium die-casting alloys until 2018. It should be noted, that the emissions from Mg foundries are extremely low compared with the applications in other industrial areas, such as high voltage switching plants [119,125]. SF_6 is one of the standard protection gas used in the Mg fabrication industry [113, 115, 120, 122, 126]. Western world smelters use SF_6 for the protection of primary Mg. China and the former countries of Soviet Union of Russia (e.g. Ukraine and Kazakhstan) use SO_2 [127]. Compared with SO_2, SF_6 is non-toxic, non-corrosive and provides protection for Mg melt [113, 120, 126].

It is possible to use CO_2, N_2, dry air and Ar as carrier gas [109,119]. SF_6 can react with the molten Mg according to the following:

When SF_6 content is < 0.5 $vol.\%$

$$Mg_{(l)} + SF_6 + dry\ air \Longrightarrow MgO_{(s)} + SF_6 \tag{3.12}$$

$SF_6 > 0.5\ vol.\%$

$$Mg_{(l)} + SF_6 + dry\ air \Longrightarrow MgO_{(s)} + MgF_{2(s)} + SO_2 + with\ traces\ of\ SF_6 \tag{3.13}$$

or also

$$Mg_{(l)} + SF_6 + O_2 \Longrightarrow MgF_{2(s)} + SO_2F_2 \tag{3.14}$$

$$MgO_{(l)} + SF_6 \Longrightarrow MgF_{2(s)} + SO_2F_2. \tag{3.15}$$

Cashion [106] proposed a similar reaction with more steps as shown in Fig. 3.12.

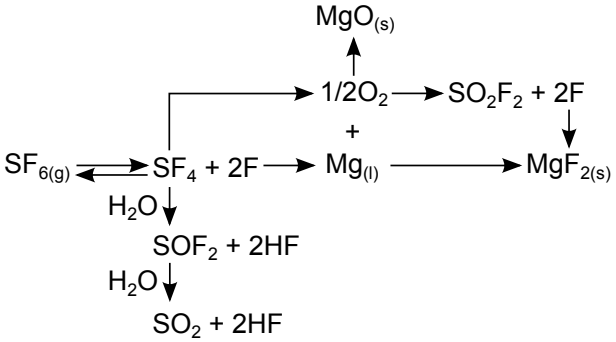

Fig. 3.12: The proposed mechanism for decomposition of SF_6 to form the protective surface film containing MgO and MgF_2. [106]

The protection mechanisms for active gases on the Mg melt is explained in a manner similar to the PBR. This explanation is used to describe the interaction of active protection gases, e.g. SF_6 with Mg. Many publications [113,128–130] report the formation of MgF_2 on the surface of the melt. Ha et al. [114] calculated a PBR of 1.29 for Mg/MgF_2. This explanation is similar to the oxide (Tab. 3.4) formation during high temperature application. The result is a dense layer of MgF_2, which protect the melt from the direct contact with air (O_2 content), CO_2 or N_2. However, the investigations of Cashion [106,113] show, that in the presence of SF_6, the contact angle between solid MgO and molten Mg is reduced. He reported poor wetting of the MgO by Mg melt and a non-adherent surface film when there is no SF_6. Pettersen et al. [128] showed that compared with oxygen and fluorine contents on the surface of Mg sulphur content is low with SF_6. The SEM investigations of Pettersen et al. [128] show that in the surface films the amount of Mg will balance the oxygen and fluorine content as MgO and MgF_2. [126, 128, 131, 132]

Substitutions for SF_6 are available e.g. NOVECTM 612 [122], HFC (e.g. HFCl34a (CF3CHtF) [122] and HFC125 [133, 134]) and more listed in Tab.3.6. The fluorinated protection gases have a comparable effect on the MgO-Mg_2F layer on top of the Mg melt. The F based gases provide the ignition resistance of Mg melt by forming Mg_2F.

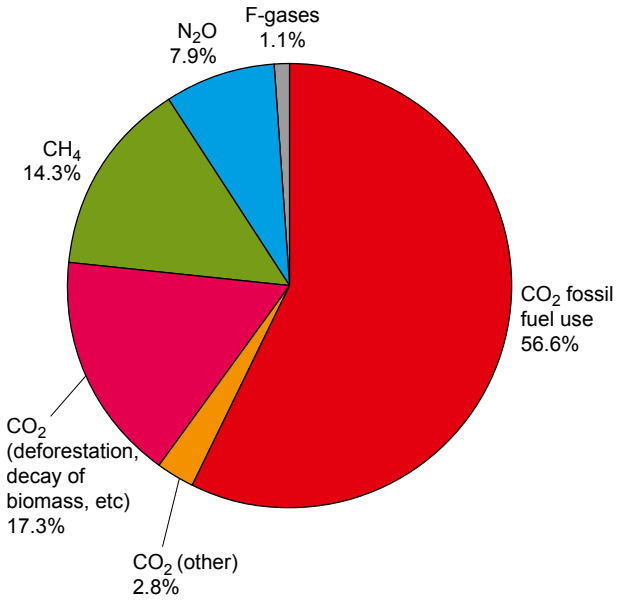

Fig. 3.13: Global greenhouse gas emissions statistics in 2004 [135].

This has led over the time to develop exotic ways to protect the Mg melt from ignition. One of these is the use of solid CO_2, it cools the top of the Mg melt, lowering the vapour pressure and inhibit the air access to the molten Mg. The GWP of solid CO_2 is 1, provided that the production of solid CO_2 is not considered. The disadvantage is the generation of highly toxic carbon monoxide and solid carbon on the interface between melt and CO_2. This technology is patented by Linde AG [136] and not currently used commercially. [122, 137]

Another approach to protecting the Mg alloys during melting and casting process, is to add special alloying elements to improve the ignition resistance. Beck [5] and Emley [4] reported that some alloying elements can reduce the oxidation behaviour of the molten Mg. These elements interact during the oxidation and form a dense oxide layer on the top of the melt. Consequently, the compositions of the Mg alloys can be used to improve the ignition and oxidation resistance of Mg alloys. This created a new type of Mg alloy, named and patented under *ECO-Mg (Environment COnscious magnesium)* [22–24]

which use CaO as a alloying addition or *Non-flammable magnesium alloy* [25] with Y in combination with Ca as alloying elements.

The alloying elements can reduce the oxidation potential and increase the oxidation resistance on the solid and/or liquid Mg [86,87]. The Section 3.2.8 lists some alloying elements which have been reported to successfully reduce the oxidation and improve ignition resistance of Mg alloys in solid and liquid state.

The improvement in the ignition resistance is explained by the formation of thermodynamically stable oxide phases containing the alloying elements with a PBR > 1 [83, 86].

ECO-Mg and *Non-flammable magnesium alloy* have a good potential to be developed for industrial application. The bottleneck with the substitution of gases or fluxes with alloying elements is the production of these alloys. All the alloys start with high purity Mg and high purity alloying elements to produce master alloys or the commercial Mg alloys. Thus, some protection is required to produce this *ECO-Mg* and *Non-flammable magnesium alloys*.

3.3 Physical background of X-ray diffraction

3.3.1 X-ray diffraction

X-ray diffraction (XRD) is a method used for the determination of crystallographic phase. X-ray or other wave forms interact with the material investigated. Due to the angle of the diffraction or reflection, the geometric arrangement of the atoms can be calculated for a given a crystal lattice. The waves scatter from lattice planes separated by the interplanar distance d (Fig.3.14). The path difference between two waves with constructive interference is given by $2d\sin\theta$, where θ is the diffraction or scattering angle. The constructive interference between X-ray with a wavelength (λ) with atomic plane related through the spacing between such atomic planes (d) and angle of interference (2θ). This relation is given by the Bragg equation Eq. 3.16. [75, 138, 139]

$$2d\sin(\theta) = n\lambda \Rightarrow d = \frac{n\lambda}{2\sin(\theta)} \tag{3.16}$$

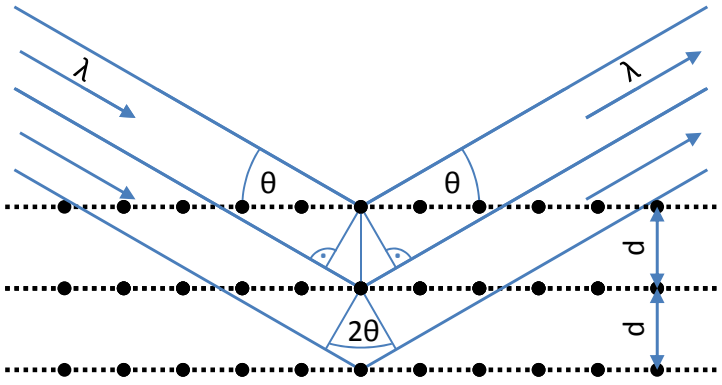

Fig. 3.14: Diffraction and the interplanar distance d in a crystal at the Bragg position.

The Bragg equation describes the relationship between wavelength λ , the angle θ , the order of interference n and the distance d of the lattice planes, which is specified in Eq. 3.16. At a given wavelength (λ) and the angle (θ), as shown in Fig. 3.14, it is possible to calculate the distance (d) of the lattice planes. The Eq. 3.16 shows that at short

wavelengths (λ), the diffraction occurs at lower angles (θ). The interplanar distance (d), can be related to a lattice plane as described by the Miller indices. The formula for this can be described in Eq. 3.17 for cubic structures and in Eq. 3.18 for hexagonal structures.

$$d = \frac{a}{\sqrt{h^2 + k^2 + l^2}} \tag{3.17}$$

$$d = \frac{a}{\sqrt{\frac{4}{3}(h^2 + k^2 + h \cdot k) + \frac{l^2}{(c/a)^2}}} \tag{3.18}$$

Depending on the orientation of the crystal relative to the incident X-ray beam different lattice planes reflect the beam where the crystal is in the Bragg condition. According to the Eq. 3.17 and Eq. 3.18 d is always smaller than or equal to the lattice constants. [75, 138, 139]

$$\frac{n \cdot \lambda}{2d} \leq 1 \tag{3.19}$$

3.3.2 X-rays

X-rays are electromagnetic waves with a wavelength λ between 0.001 to 10 nm. This wavelength is lower in comparison with visible light, λ 430-640 nm, by two to six orders of magnitude. The wavelength λ is directly related to the energy of electromagnetic waves. The conversion of energy to the wavelength is specified in Eq. 3.20 to Eq. 3.22. The photon energy of the X-ray radiation is in the range 5 to 5000 keV. [138–141]

The energy or the wave length of X-ray may be calculated with Eq. 3.20 - 3.22.

$$f = \frac{c}{\lambda} \tag{3.20}$$

in to Eq. for energie E_r

$$E_r = h \cdot f \tag{3.21}$$

$$\lambda = \frac{c \cdot h}{E_r} \Rightarrow \lambda[nm] = \frac{1,2398419}{E_r[keV]} \tag{3.22}$$

The constants for these equations are:

- f Frequency
- c speed of light in vacuum $2,99792458 \cdot 10^8 \frac{m}{s}$
- h Planck constant $6.62606957 \cdot 10^{-34} Js$
- E_r energy $1.60217656535 \cdot 10^{-19} J = 1eV$

The X-ray sources include laboratory scale X-ray tubes or synchrotron sources.

3.3.3 X-ray tube

The basic principle of the X-ray tube is based on the release of X-ray radiation from a cathode. The general set-up is shown in Fig. 3.15. The simple X-ray tube uses thermal emission for electrons. The electrons are accelerated by an external electrical field. The energy or wavelength λ depend on the anode material (mostly a metal) and the accelerating voltage. During interaction with the metal the electrons are decelerated and a different type of radiation is produced. The radiation from this process is normally the X-ray radiation [142]. For investigations the emission of K-α important, as this generate X-rays with a fixed energy as well as wavelength (λ). The high energy electrons are able, to remove a electron from the atomic shell of the metal. The vacancy created is filled with an electron from a higher orbit, and the energy difference is be emitted as a photon. The possible transitions are material dependent. The energy of the emitted X-ray is determined by the anode material according to the Moseley's law and has a fixed value for a given element [143].

X-ray tube provide a range of set-ups for X-ray diffraction (XRD) investigation. The most common applications for X-ray diffraction is:

- d-spacing and structure determination of new phases
- Phase analysis in inhomogeneous materials (powder diffractometry)
- Texture measurements
- Retained stress measurements etc.

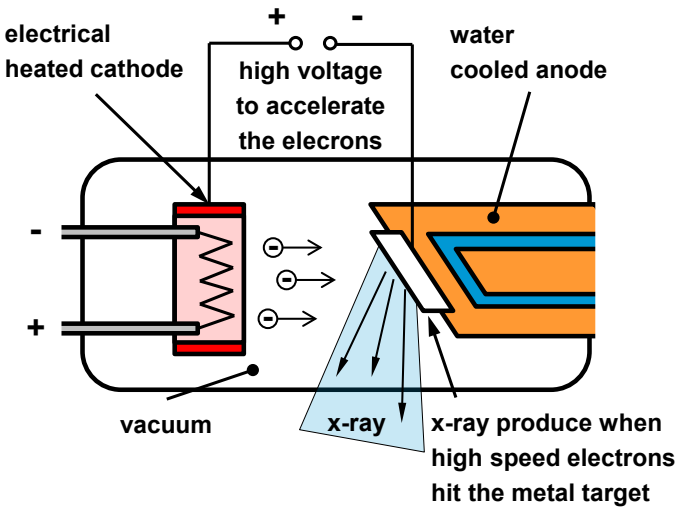

Fig. 3.15: General set-up of a X-ray tube.

3.3.4 Synchrotron

A synchrotron is a brilliant X-ray radiation source. The general synchrotron is composed of straight sections with accelerator and bending magnets, that guide bunches of charged particles (elections or positrons) on a circular trajectory with relativistic speed. The bending magnets change the direction of the charged particles on curved path using a magnetic field. The third generation of synchrotrons use undulator or wigglers for the emission of synchrotron radiation. Undulators and wigglers are tools used to bend the trajectory of the charged particles periodically by magnets. These oscillations produce intense beams of radiation with a low angle deviation. The emitted radiation is guided through a monochromator and focusing device, before the radiation is used for an experiment. [138, 144]

Brilliance of the synchrotron radiation is determined by photons for unit time $[sec]$, source size $[mm^2]$, opening angle $[mrade^2]$ and 0.1 % spectral bandwidth Eq. 3.23. A synchrotron generates radiation with wavelengths of 10^{-12} to 10^{-4} m, this covers the spectra from X-rays up to infra red radiation. For diffraction investigations a synchrotron radiation source must have a wavelength shorter than the expected lattice spacing (Section 3.3). Synchrotron radiation provide these wavelengths, by the adjusting the energy of the beam (Section 3.3.2). In comparison with lab scale X-ray sources, the energy can be adjusted

in the synchrotron and is used mostly with a high energy which correspond to shorter wavelengths. [138, 144, 145]

$$B = \frac{[Photons]}{[sec] \cdot [mm^2(source)] \cdot [mrad^2] \cdot [0.1\% bandwith]} \tag{3.23}$$

High energy X-rays offer larger penetration depths. This is required for the investigation of bulk structures in engineering materials. To investigate processes that can occur rapidly in a engineering materials the hight flux of photons provide a required short acquisition time. This provide the possibility for the *in situ* experiments for time and temperature depended processes using synchrotron radiation. [138, 146]

A list of investigation conducted which used synchrotron diffraction methods are listed below:

- Heat treatment (phase formation or transformation) [146]
- Tensile and compression testing for internal stress, phases changes, texture changes etc. [138, 146–148]
- Stress detection during cutting, welding etc. [138, 146, 149]
- Solidification different alloy systems, e.g. Mg alloys [150–152], Al alloys [153, 154], steels [155], Nd alloys [156] and Zr alloys [157].

CHAPTER 4

Experimental

4.1 *In situ* investigations

During the development of the experimental setup, three different experimental setups were investigated for the *in situ* synchrotron measurement. The changes to the setup include the sample preparation, the furnaces used and the temperature-time-program. The set up with the sample preparation was developed in two earlier experimental investigations. The first experiment provided only a powder after the experiment and not a bulk sample of Mg with 10 $wt.\%$ CaO to verified the *in situ* results [158] with the microstructural evaluation. The second experiment was conducted with gas atomised Mg and Al powders with CaO powder, but the results show the oxide on the metallic powder present the development of a homogenised microstructure [159]. Based on these results the third setup was developed to use in this investigation.

4.1.1 Sample preparation

Pure Mg(99.99 %) was investigated as a reference material to test the setup. The first group of samples contain pure Mg (99.99 %) with CaO powder (Calcium oxide $\geq$ 96 % powder from CARL ROTH). The second set of samples contain the master alloys Mg6Ca and Mg16Ca with 6 $wt.\%$ CaO powder (Calcium oxide $\geq$ 96 % powder from CARL ROTH).

The nominal compositions of the samples investigated are listed as follows:

- Pure Mg
- Pure Mg with 20, 30 and 50 $wt.\%$ CaO powder: Mg20CaO, Mg30CaO and Mg50CaO
- Mg6Ca master alloy with 6 $wt.\%$ CaO powder: Mg6Ca+6CaO
- Mg16Ca master alloy with 6 $wt.\%$ CaO powder: Mg16Ca+6CaO

The pure Mg and the Mg-Ca master alloys were produced by cutting. The CaO powder was dried for 6 h at 350 $°C$ into small chips. This chips were mixed with the CaO powder for 3 min, to create a uniform mixture. The mixture was pressed with a hydraulic press to cylinders with a diameter of 4 mm and a hight of 3 to 4 mm. The applied pressure was 100 MPa and samples were held for 1 min under this pressur. The samples were stored in sealed plastic bags until the *in situ* investigations.

4.1.2 *In situ* synchrotron radiation diffraction measurement

The *in situ* investigations were conducted at DESY (Deutsches Elektronen-Synchotron) in Hamburg Germany. The measurement time was given under the Proposal I-20130330: *In situ diffraction of the melting and the solidification of magnesium alloys containing* CaO in 2013 at PETRA III. The setup in general is illustrated in Fig. 4.1. The source for the synchrotron radiation in all experiments was the PETRA III [145, 160] and the setup was in the measurement hutch P07 of the High Energy Materials Science (HEMS) beamline [145]. The synchrotron radiation diffraction study was conducted with a beam energy of 100 KeV, this can be converted in to a wavelength of $\lambda = 0.0124$ nm. The beam cross section was set to 1 x 1 mm^2.

The experiment was conducted in the induction coil of a furnace built for *in situ* synchrotron radiation measurements, as shown in Fig. 4.2. The furnace chamber and induction coil (gap in the coil) were modified to allow the X-ray beam to pass after interacting only with the sample. The setup was isolated from the surrounding with two windows covered with Kapton foils to allow the passage of beam without interference. The sample

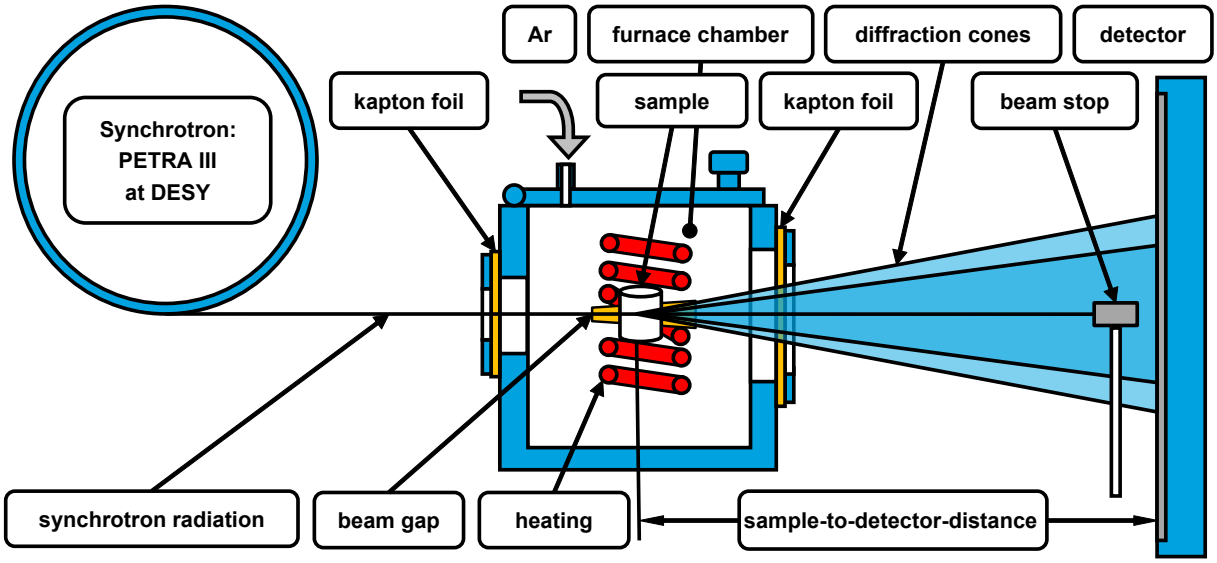

Fig. 4.1: General setup for the *in situ* synchrotron radiation diffraction measurement.

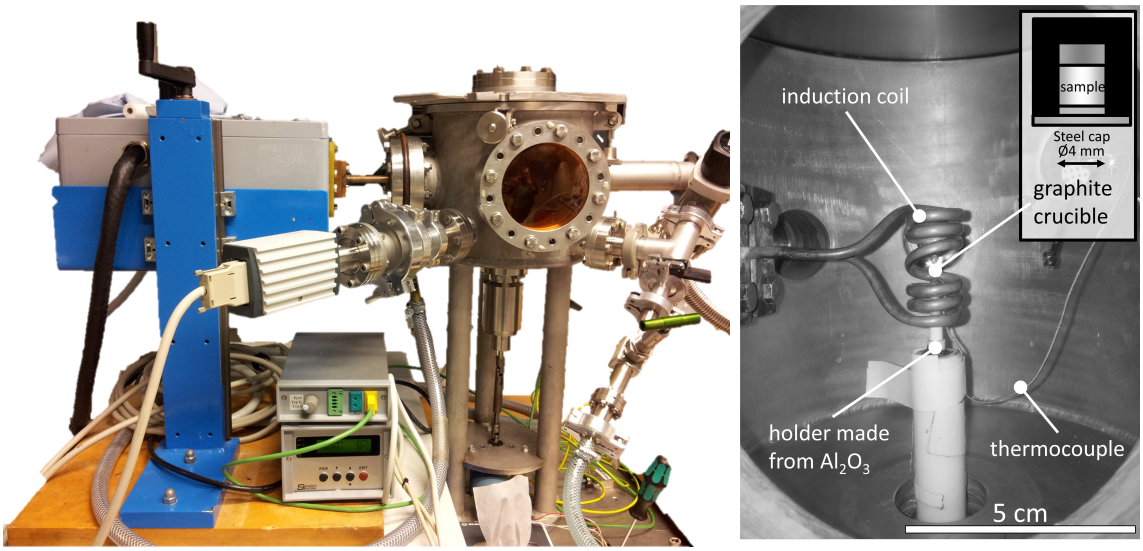

Fig. 4.2: The camber of the induction furnace built for the *in situ* synchrotron radiation measurements on the left and right a schematic of the sample holder with graphite crucible sealed with a steel lid.

were heated in an Ar atmosphere to 750 $°C$ at 10 $\frac{K}{min}$, held at 750 $°C$ for 5 min to ensure melt homogeneity, and then cooled at 10 $\frac{K}{min}$ to 200 $°C$ (fully solidified state) before air-cooling to room temperature. The molten samples were held in position in a graphite crucible with a steel lid. The graphite crucible was inverted (Fig. 4.2 right up in the corn) and the steel lid sealed with a high temperature glue, Thermocoll from KERAMAB N.V. The crucibles were prepared in ambient condition. The temperature-time-curve was controlled with a S type thermocouple welded to the lid of the crucible. The crucible with sample was rotated by 90 ° during acquisition to improve statistics.

The two dimensional (2D) diffraction patterns were recorded in transmission geometry with a PerkinElmer XRD 1622 Flatpanel detector [161] at a sample-to-detector-distance of 1162.7 mm (calibrated with LaB_6 reference), as illustrated in Fig. 4.1. The patterns were recorded every 12 s with a acquisition time of 1 s, together with the heating rate the temperature resolution is 2 $°C$. X-ray line profiles were obtained by azimuthal integration of the 2D diffraction patterns through 360° using FIT2D V12.077 software. For phase identification simulated line profiles were generated with CaRIne 3.1 Crystallography^{TM} with crystal structure data from the Pearson's Crystallography Database [77].

4.2 Composition measurement of the Mg chips

The Mg, Ca and O contents of the pure Mg and the pure Mg-Ca master alloys chips were measured with a TESCAN VEGA III, equipped with an EDAX energy-dispersive X-ray spectrometer (EDXS) operating at 20 kV. For this measurement the chips were pressed with a hydraulic press to cylinders with a diameter of 4.0 mm, under an applied pressure of 500 MPa and held for 1 min under pressure. The three samples of these compacted chips were measured on three different areas on the surface with EDXS for 10 min, to determine the composition of the chips

4.3 Metallographic investigation

4.3.1 Grinding and polishing the *in situ* samples

The samples were embedded in epoxy resin, with DEMOTEC 30, 2/3 powder and 1/3 hardner liquid mixed to form the resin which was left to harden. The specimens were prepared by grinding with SiC paper to 2500 $grit$ at a speed of 150 min^{-1}. In the first step 3 μm diamond paste were used followed by a mixture of 1 μm diamond and OPS^{TM} ($\approx$ 1 μm) anhydrous suspension with at a speed of 80 min^{-1}, for polishing the samples.

4.3.2 Scanning electron microscopy

Microstructures were investigated using a TESCAN VEGA III, operating at 20 kV, equipped with an EDAX energy-dispersive X-ray spectrometer (EDXS) and the local compositions determined with EDXS compositional maps. The Scanning electron microscopy (SEM) investigation was conducted on polished samples. The compositional maps were recalculated with the software Iridium Ultra in $wt.\%$. After the recalculation the maps are saved as ASCII files and converted with ImageJ in to PNG files. The scripts used to convert the ASCII files are provided in the appendix (Section F). The scripts change the picture size and include the scale bar depending on the pixel size of the maps.

CHAPTER 5

Results

5.1 Composition of the Chips

The Mg, Ca and O content of the pure Mg and the Mg-Ca master alloys chips were measured with SEM-EDXS, Tab. 5.1.

Tab. 5.1: The measured composition for pure Mg, Mg6Ca and Mg16Ca chips using SEM-EDXS measurement.

Sample	Composition	Ca $[wt.\%]$	O $[wt.\%]$	Mg $[wt.\%]$
Pure Mg	average	-	2.3 ± 0.5	97.7 ± 19.6
	standard deviation	-	0.2	0.2
Mg6Ca	average	4.9 ± 1.0	3.9 ± 0.8	91.1 ± 18.2
	standard deviation	0.2	0.2	0.3
Mg16CaO	average	15.1 ± 3.0	6.0 ± 1.2	78.9 ± 15.8
	standard deviation	0.6	0.3	0.8

5.2 Pure Mg

The X-ray line profiles from the synchrotron investigation show the melting of pure Mg during heating cycle, Fig. 5.1(a). At the start the peaks from Mg are observed. A small reduction of the intensity and the movement of the peak position to lower 2θ angle, due to the thermal expansion was observed during heating. Once the temperature reached 651.6 $°C$ the intensity of the Mg peaks decreased rapidly with no intensity detected at 654.2 $°C$. Above this temperature the patterns show the diffraction peaks of the graphite crucible and a diffuse background due to molten Mg. During the holding time no change can be detected. The first sets of Mg peaks appear during solidification at 649.1 $°C$ and the solidification ends at 647.0 $°C$, Fig. 5.1(b). There is no statistical distribution of peaks during the cooling (Fig.5.1(b)) indicating, that only a small volume of Mg is in Bragg condition. The detected temperatures for disappearance and appearance of Mg are listed in Tab. 5.2.

Tab. 5.2: Phase changes with temperatures in the sample pure Mg. The abbreviation (H) for heating and (C) for cooling.

Reaction	Experimental data ± 5 [$°C$]
Disappearance of Mg start	651.6 (H)
Disappearance of Mg end	654.2 (H)
Appearance of Mg start	649.1 (C)
Appearance of Mg end	647.0 (C)

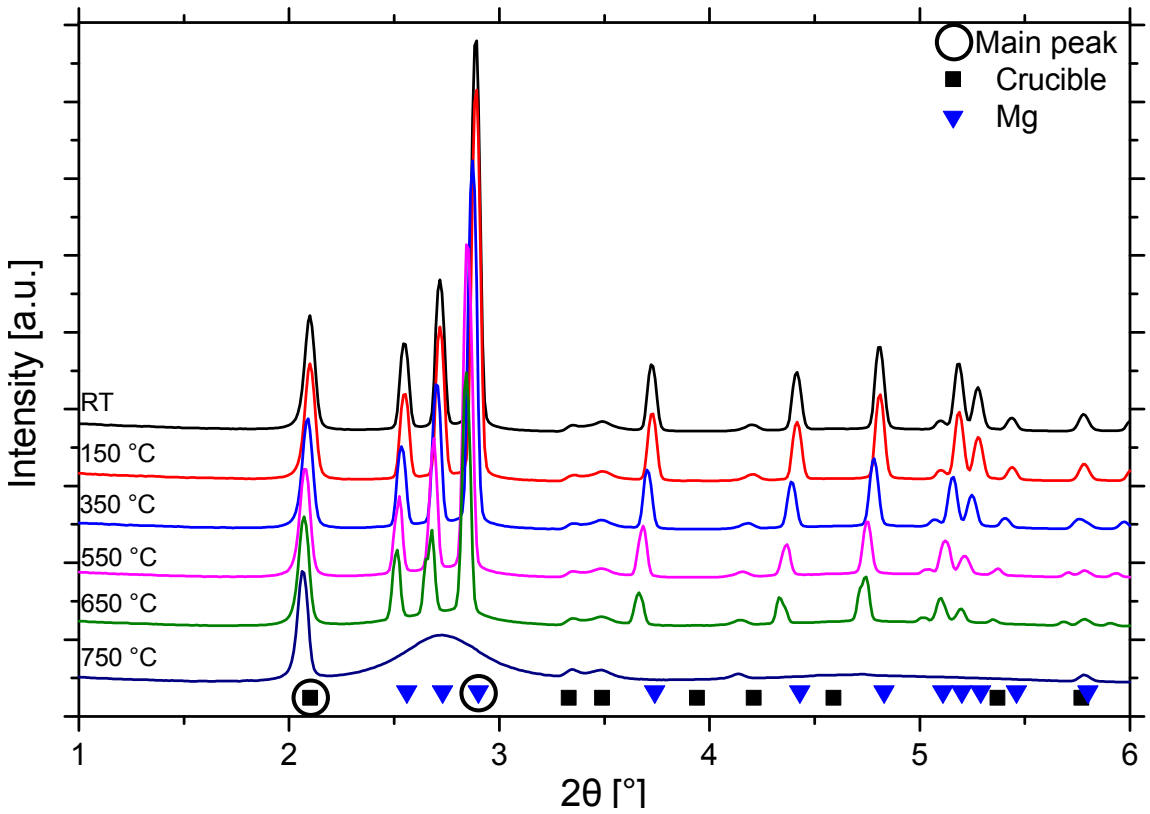

(a) Heating

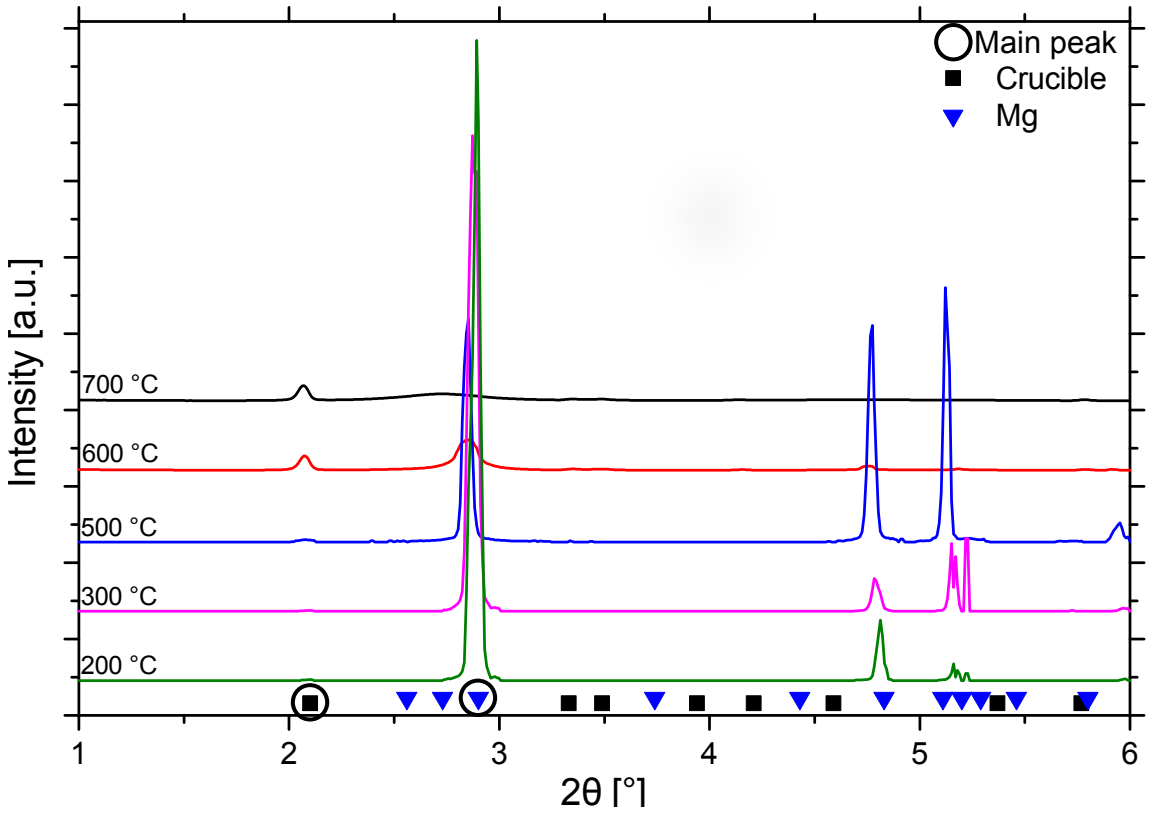

(b) Cooling

Fig. 5.1: Selected line profiles from a) heating and b) cooling process of the pure Mg sample with the observed phases indicated.

5.3 Mg20CaO

The temperature at which, the detected phases, appear or disappear are listed in Tab. 5.3 and the line profiles (LP) at different temperatures are illustrated in Fig. 5.2.

The X-ray line profiles show that peaks due to $Ca[OH]_2$, CaO, Mg and graphite crucible are present in the beginning. During heating the main peak of CaO becomes more visible when heated above 291 $°C$, due to the thermal expansion of Mg. This is followed by the stabilisation of the intensity of CaO peaks up to 396 $°C$ and a second increase in peak intensity at 502 $°C$ to a maximum of intensity. The peak intensity of CaO decreased from 568 $°C$. During heating the peaks of MgO and CaO_2 are detected at a temperature of 340 $°C$. The peaks of $Ca[OH]_2$ starts to disappear at 408 $°C$ and are undetectable at 500 $°C$. The peak of CaO_2 disappeared at the same temperature when the MgO peaks became stable, at 618 $°C$. In the temperature range between 620 and 637 $°C$ the Mg peaks disappear. With the disappearance of Mg the diffuse contrast of the melt was detected. From 664 $°C$ the CaO peaks stabilise and show no further changes in intensity.

During cooling the first peaks of Mg are detected at 570 $°C$ and no intensity changes were detected below 509 $°C$. The Laves phase Mg_2Ca was detected at 511 $°C$ with no further intensity changes below 509 $°C$.

The microstructure of the sample used for the *in situ* investigation was analysed with SEM. The EDXS maps show the distribution of the elements Mg, Ca and O in the solidified sample, Fig. 5.3. From the microstructure the solidification sequence can be understood. The solidification begins with Mg grains and ends finally with an eutectic solidification of a Mg and Ca rich lamellar structure. The O agglomerates in the eutectic region in a form of clusters of oxide particles with a higher concentration of Mg. The final composition was measured using EDXS with 6.8 ± 1.4 $wt.\%$ Ca, 8.7 ± 1.7 $wt.\%$ O and balance Mg. This composition deviates form the nominal content of 14.3 $wt.\%$ Ca, 5.7 $wt.\%$ O and balance Mg.

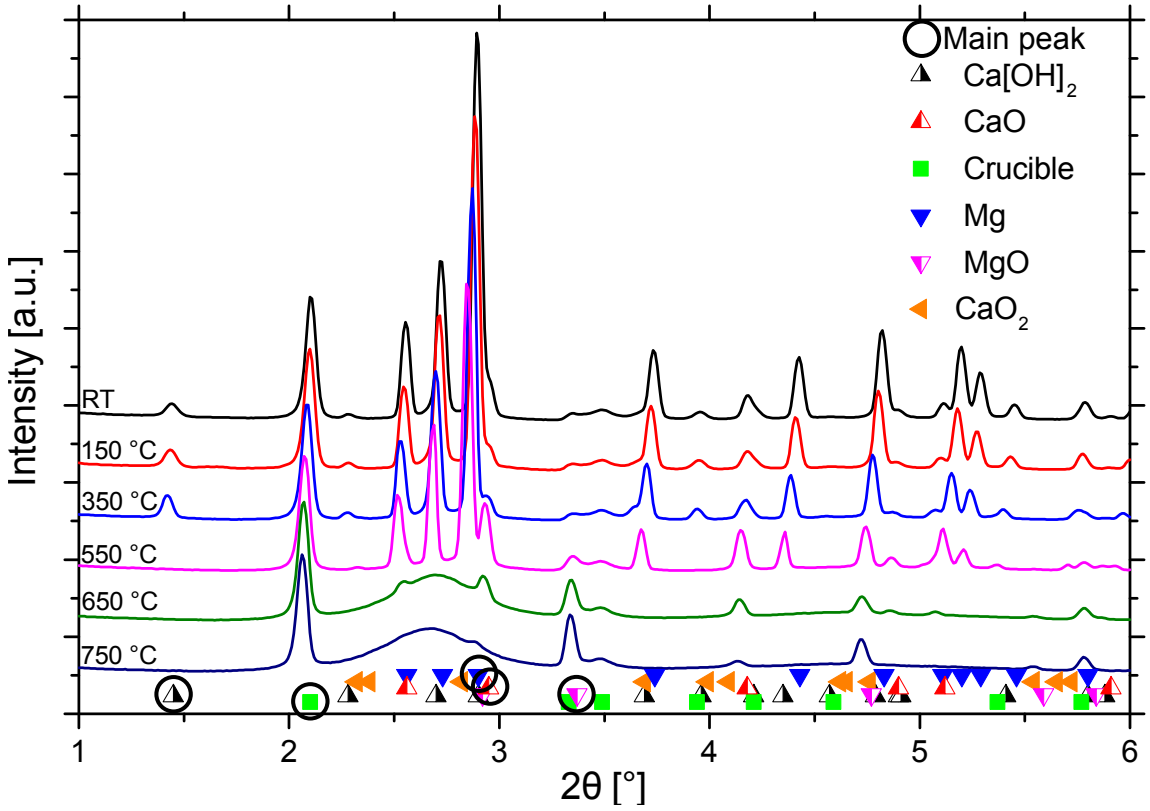

(a) Heating

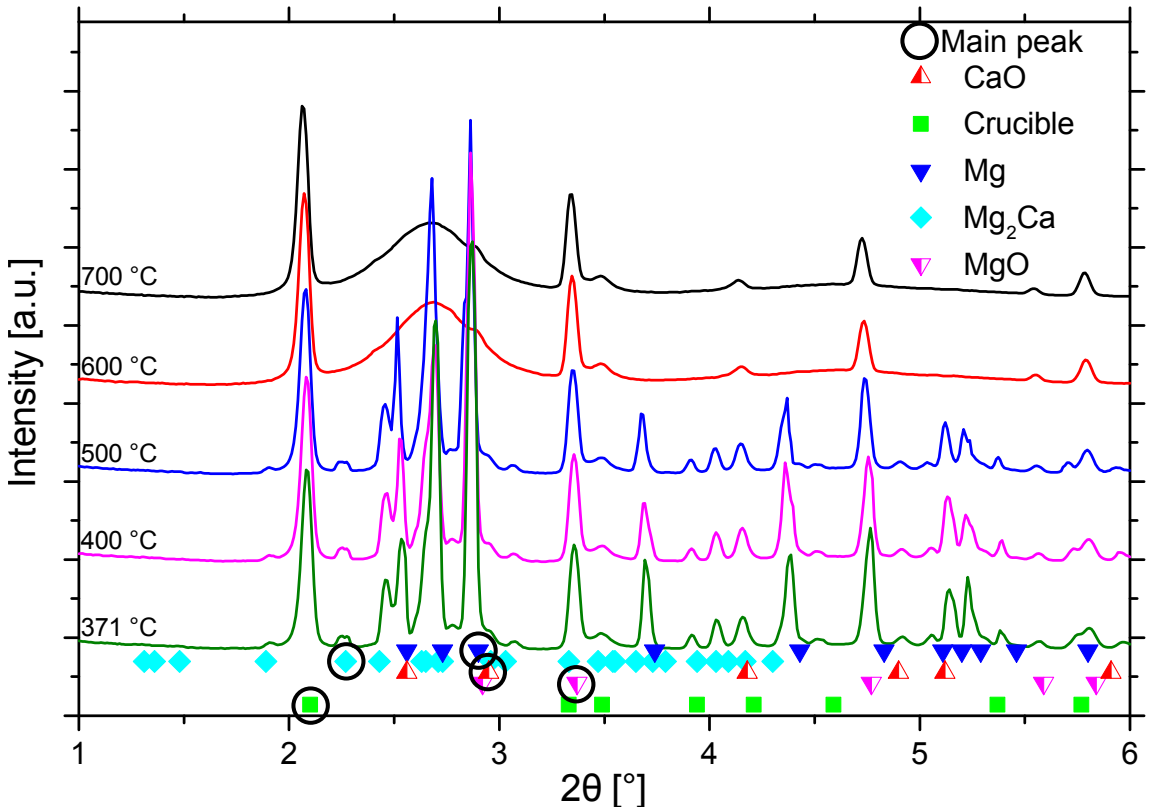

(b) Cooling

Fig. 5.2: Selected line profiles during a) heating and b) cooling of the sample $Mg20CaO$.

Tab. 5.3: Phase changes with temperatures in the sample $Mg20CaO$. The abbreviation (H) for heating and (C) for cooling.

Reaction	Experimental data ± 5 [°C]
Increment of CaO end (stable)	291 (H)
Appearance of CaO_2	340 (H)
Appearance of MgO start	340 (H)
Increment of CaO start 2	396 (H)
Disappearance of $Ca[OH]_2$ start	408 (H)
Disappearance of $Ca[OH]_2$ end	500 (H)
Increment of CaO end 2 (max.)	502 (H)
Decrement of CaO start	568 (H)
Disappearance of CaO_2	618 (H)
Appearance of MgO end (stable)	618 (H)
Disappearance of Mg start	620 (H)
Disappearance of Mg end	637 (H)
Decrement of CaO end (stable)	664 (H)
Appearance of Mg start	570 (C)
Appearance of Mg_2Ca start	511 (C)
Appearance of Mg end	509 (C)
Appearance of Mg_2Ca end	509 (C)

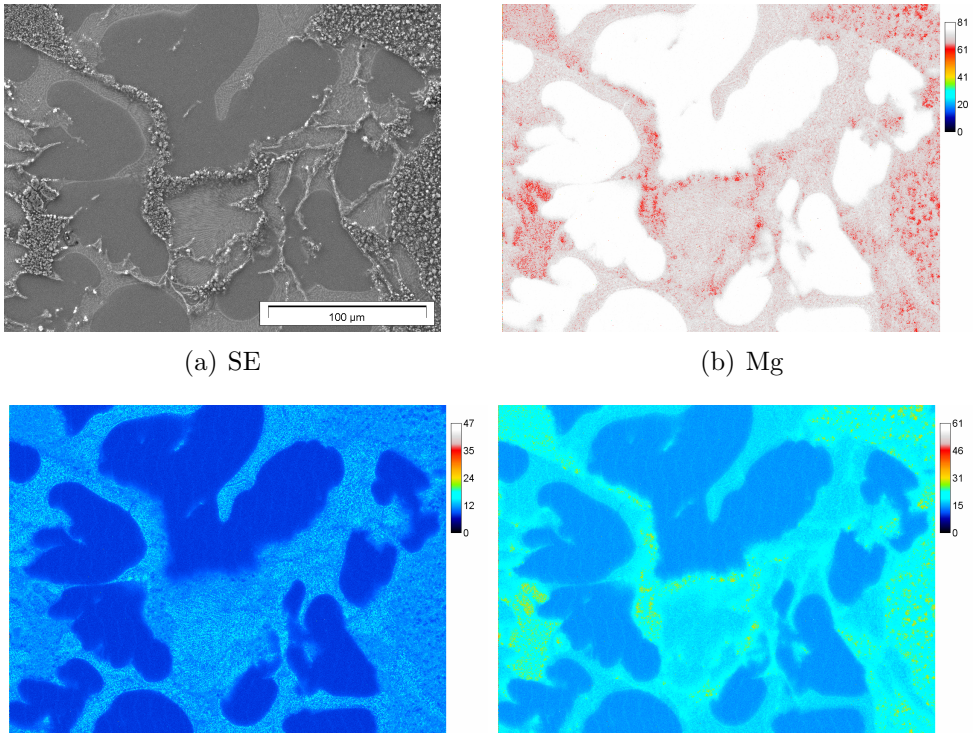

(a) SE (b) Mg

(c) Ca (d) O

Fig. 5.3: The (a) SE micrograph and EDXS maps for (b) Mg, (c) Ca and (d) O of Mg20CaO. (The composition in $wt.\%$.)

5.4 Mg30CaO

The appearance or disappearance of the phases are listed in Tab. 5.4 and the line profiles (LP) for the experiment are illustrated in Fig. 5.4. The LP numbers were used, as the time and temperature of the experiment could not recorded, due to experiment set-up error associated with RAM overflow. The calculation of the actual temperature of the patterns was not possible. The comparison with other temperature-time curves and temperature determined by considering the thermal expansion of the lattice distance of graphite and Mg were not successful in generating the reliable temperature data. However, the results show the phase evolution sequence during heating and cooling.

The X-ray line profiles show that $Ca[OH]_2$, CaO, Mg and graphite from the crucible are present in the beginning. During the heating the peaks of CaO decrease to a minimum intensity by LP 109. Followed by an increase up to the maximum peak intensity at LP 263. During heating the peaks of CaO_2 are detected at LP 132 and disappear at LP 259. The peaks of MgO are detected at LP 163 and increased up to LP 204. Followed by the second increase in the peak intensity of MgO at LP 225 and no intensity changes were detected after LP 339. Followed by the maximum in the peak intensity for CaO at LP 263 and it decreased to a stable of peak intensity at LP 309. During heating the peaks of Mg decrease in intensity between LP 257 and 267. When Mg start to disappear Mg the diffuse contrast of melt was detected. After the disappearance of the Mg peaks the intensity of the CaO peaks become stable at pattern 309 and the intensity of MgO peaks are stable after LP 339. From this LP 339 the CaO and MgO peaks remain stable and show no changes in intensity.

During cooling the first peaks of Mg are detected at LP 406 and and no intensity changes were detected after LP 409. The Laves phase Mg_2Ca was detected at LP 407 with no further intensity changes.

The microstructure of the sample from the *in situ* experiments were investigated with SEM. The EDXS maps illustrate the distribution of the elements Mg, Ca and O in the solidified sample, Fig. 5.5. From the microstructure the solidification sequence is proposed.

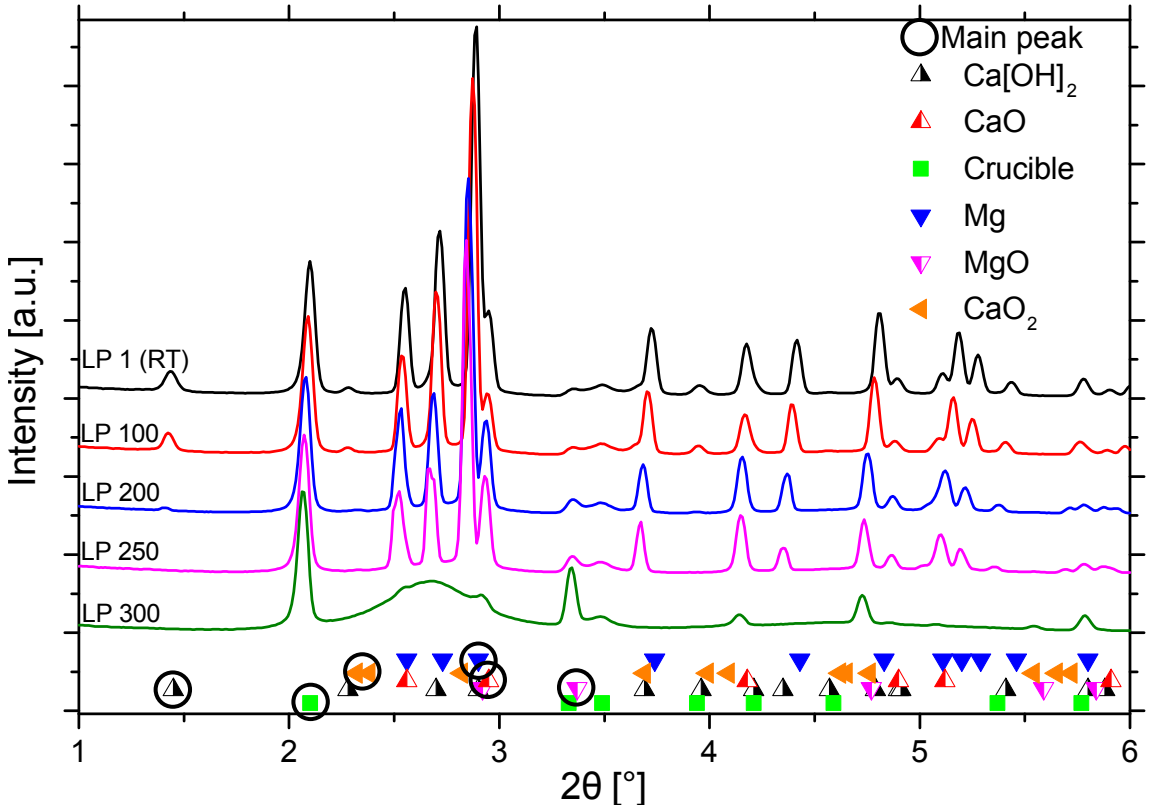

(a) Heating

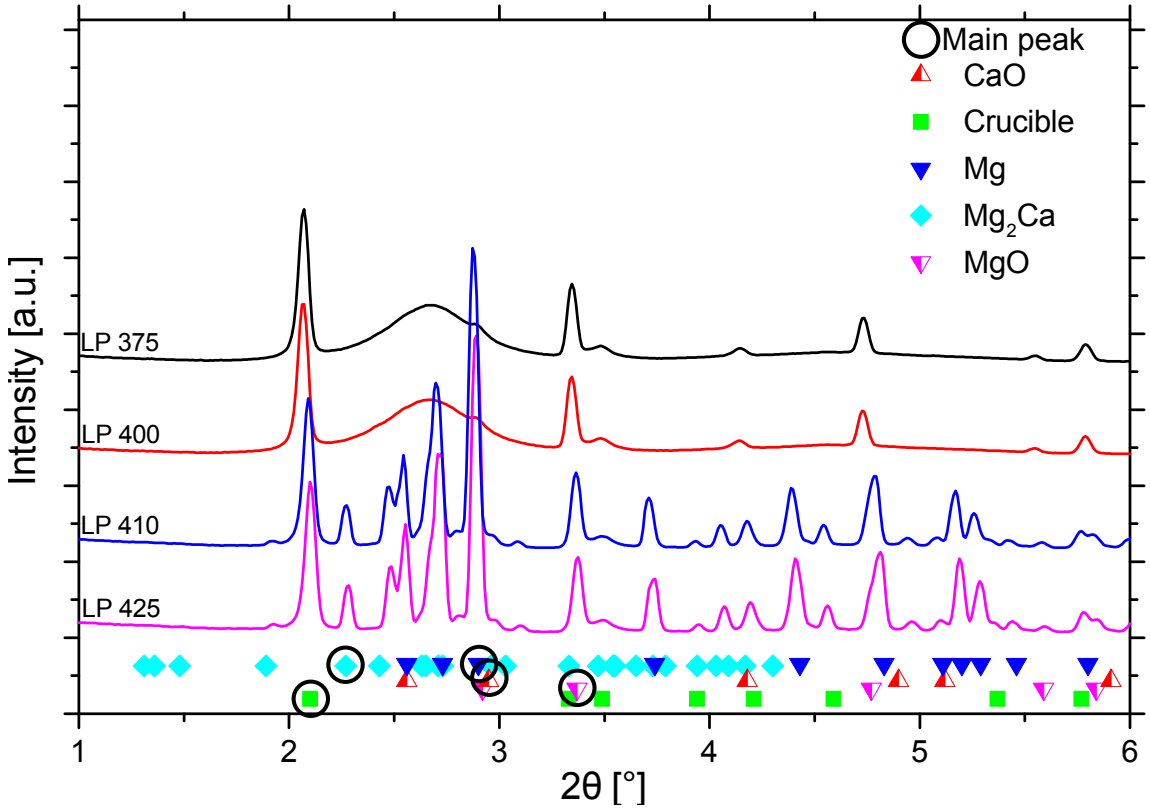

(b) Cooling

Fig. 5.4: Selected line profiles (LP) during a) heating and b) cooling of $Mg30CaO$.

Tab. 5.4: Phase changes with the pattern number in the sample Mg30CaO. The abbreviation (H) for heating and (C) for cooling.

Reaction	Experimental data pattern number
Increment of CaO start	109 (H)
Appearance of CaO_2	132 (H)
Appearance MgO start	163 (H)
Disappearance $Ca[OH]_2$ start	165 (H)
Disappearance of $Ca[OH]_2$ end	204 (H)
Appearance of MgO end (stable)	204 (H)
Increment of MgO start	225 (H)
Disappearance of Mg start	257 (H)
Disappearance of CaO_2	259 (H)
Increment of CaO end (max.)	263 (H)
Decrement of CaO start	263 (H)
Disappearance of Mg end	267 (H)
Decrement of CaO end (stable)	309 (H)
Increment of MgO end (stable)	339 (H)
Appearance of Mg start	406 (C)
Appearance of Mg_2Ca start	407 (C)
Appearance of Mg_2Ca end	407 (C)
Appearance of Mg end	409 (C)

The solidification begins with Mg dendrites and ends with the eutectic solidification of a Mg and Ca rich lamellar structure. The O agglomerates in the eutectic regions as clusters of oxide particles with a higher concentration of Mg in a larger region and smaller regions with a higher concentration of Ca. The final composition was measured using EDXS with 9.4 $\pm$ 1.9 $wt.\%$ Ca, 6.4 $\pm$ 1.3 $wt.\%$ O and balance Mg. This composition deviates from the nominal content of 21.4 $wt.\%$ Ca, 8.6 $wt.\%$ O and balance Mg.

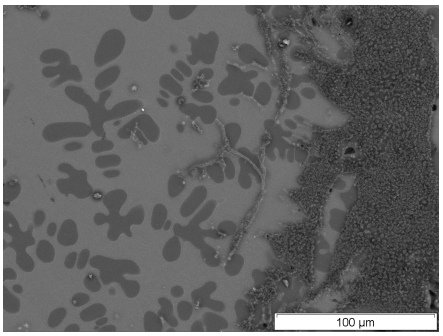

(a) SE

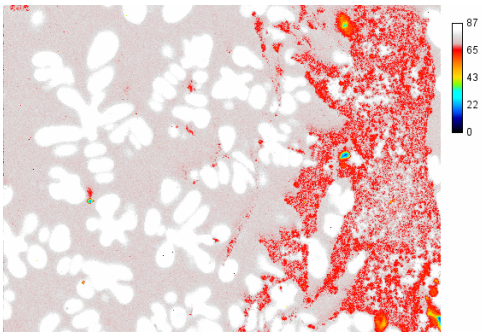

(b) Mg

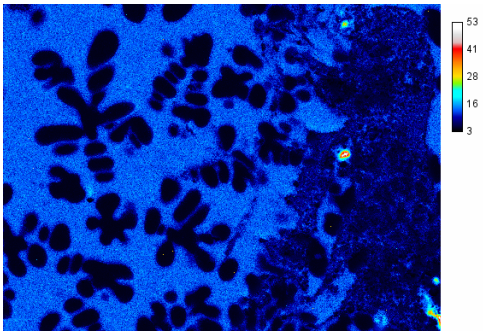

(c) Ca

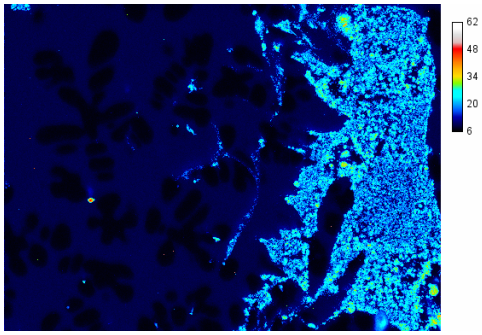

(d) O

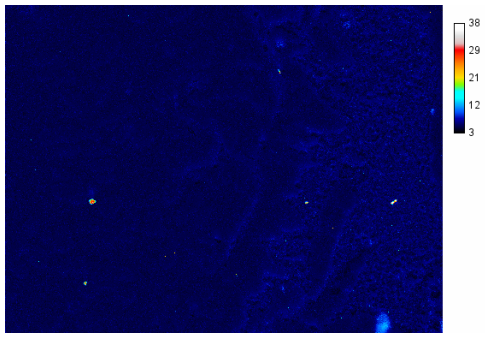

(e) Si

Fig. 5.5: The (a) SE micrograph and EDXS maps for (b) Mg, (c) Ca, (d) O and (e) Si of the Mg30CaO. (The composition in $wt.\%$.)

5.5 Mg50CaO

The diffraction patterns of the Mg50CaO sample are not detected during the *in situ* experiment, due to a failure in the recording process. The microstructure of the Mg50CaO sample was investigated with SEM. The EDXS maps of the microstructure shows the distribution of the elements Mg, Ca, O and Si in the solidified sample, Fig. 5.6. The EDXS maps illustrate a separated microstructure with O rich regions and metal rich regions. From the microstructure in the metal rich regions the solidification sequence can be deciphered. Due to the globular shape of the Mg grains, it is assumed that the solidification begins with Mg grains. The solidification ends with the eutectic solidification of a Mg and Ca rich lamellar structure, which dominated the metal rich regions. The metal rich regions are embedded in the O rich regions. The O rich regions show two areas. The first area with a Ca content between 25 to 35 $wt.\%$ and a Mg content of approximately 45 $wt.\%$ with a lower O content. In the second region only Mg was detected with no Ca. This area contained more O compared with the first region. The O rich regions with Ca and Mg are show some holes and cracks. Some SiO particles from the polishing solution (OPS) adhere inside these holes and cracks, which can be identified by the position of O, Si and SEM SE image, and this is disregarded. The final composition was measured by EDXS with 12.6 $\pm$ 2.5 $wt.\%$ Ca, 12.8 $\pm$ 2.6 $wt.\%$ O and the balance Mg. The Si is from the polishing solution (OPS) on the surface of the polished sample and was not included in the calculations. This composition deviate form the nominal content of 35.7 $wt.\%$ Ca, 14.3 $wt.\%$ O and balance Mg.

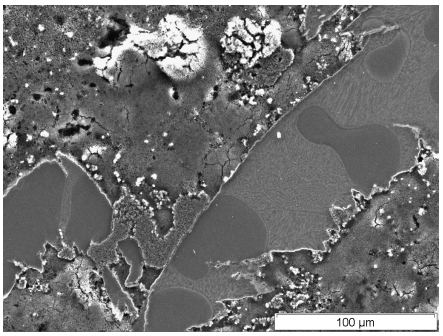

(a) SE

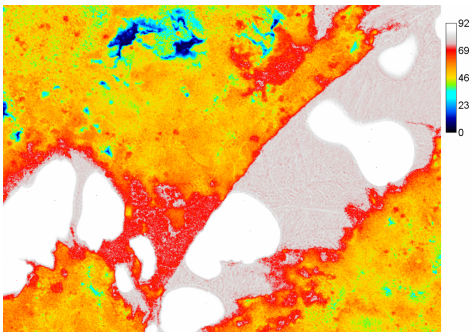

(b) Mg

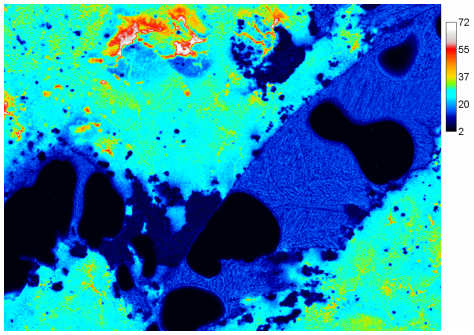

(c) Ca

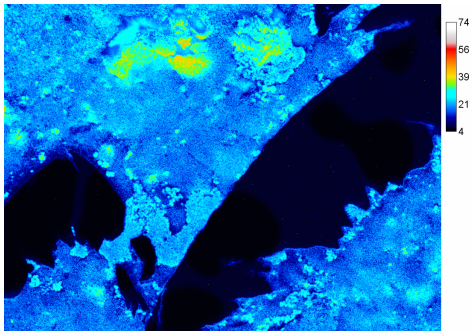

(d) O

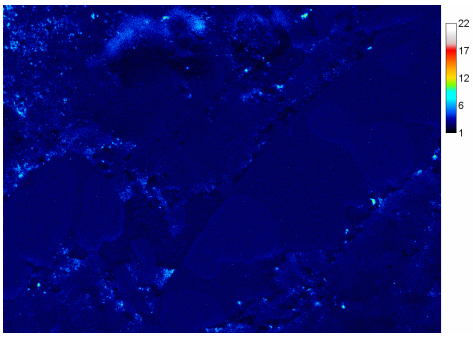

(e) Si

Fig. 5.6: The (a) SE micrograph and EDXS maps for (b) Mg, (c) Ca, (d) O and (e) Si of the Mg50CaO. (The composition in $wt.\%$.)

5.6 Mg6Ca+6CaO

This composition was used to determine data away from the CaO iso composition line. The temperature at which phases, appear or disappear are listed in Tab. 5.5 and the LP at different temperatures are illustrated in Fig. 5.7.

Tab. 5.5: Phase changes with temperatures in the sample Mg6Ca+6CaO. The abbreviation (H) for heating and (C) for cooling.

Reaction	Experimental data $\pm$ 5 [$°C$]
Disappearance $Ca[OH]_2$ start	350 (H)
Appearance of CaO_2	351 (H)
Disappearance of $Ca[OH]_2$ end	433 (H)
Appearance of MgO start	486 (H)
Disappearance of Mg start	504 (H)
Disappearance of Mg_2Ca start	504 (H)
Disappearance of Mg_2Ca end	506 (H)
Increment of CaO end (max.)	589 (H)
Decrement of CaO start	589 (H)
Disappearance of Mg end	602 (H)
Disappearance of CaO_2	667 (H)
Decrement of CaO end (stable)	671 (H)
Appearance of MgO end (stable)	675 (H)
Appearance of Mg start	581 (C)
Appearance of Mg end	504 (C)
Appearance of Mg_2Ca start	504 (C)
Appearance of Mg_2Ca end	504 (C)

The X-ray LP show that $Ca[OH]_2$, CaO, Mg, Mg_2Ca and graphite from the crucible are present at the beginning of the experiment. The peak intensity of $Ca[OH]_2$ decreased from 350 $°C$, followed by the appearance of CaO_2 peaks at 351 $°C$. During heating the peaks of Mg decrease at of 504 $°C$ and completely disappear by 602 $°C$. The peaks of Mg_2Ca decrease at the same temperature as Mg, 504 $°C$ and completely disappear by 506 $°C$. With the disappearance of Mg the diffuse contrast of the melt was detected. The first peaks of MgO were detected at a temperature of 486 $°C$. During heating the intensity of CaO peaks increased and then start to decrease from a temperature of 589 $°C$. The peak of CaO_2 disappeared at 667 $°C$ and CaO peaks became stable at a temperature of 671 $°C$, followed by the stabilisation of the peak intensity of MgO at 675 $°C$.

During cooling the first peaks of Mg were detected at 581 $°C$ and intensity changes was not observed below 504 $°C$. The Laves phase, Mg_2Ca was detected at 504 $°C$ with no further intensity changes.

The microstructure of the sample from the *in situ* experiment was investigated with SEM. The EDXS maps show the distribution of the elements Mg, Ca, Si and O in the solidified sample, Fig. 5.8. The Si is from the polishing solution (OPS) in pits of the polished sample, and can be disregarded, Fig. 5.8(e). From the microstructure the solidification sequence can be understood. The solidification begins with Mg grains and dendrites formation and ends with an eutectic solidification of a Mg and Ca rich lamellar structure. The O agglomerates in the eutectic region and form clusters of mixed Ca and Mg oxide particles with a Ca and Mg rich region. The final composition was, measured using EDXS, 8.2 ± 1.6 $wt.\%$ Ca, 4.8 ± 1.0 $wt.\%$ O and balance Mg. This composition deviates from the nominal content of 10.3 $wt.\%$ Ca, 1.7 $wt.\%$ O and balance Mg.

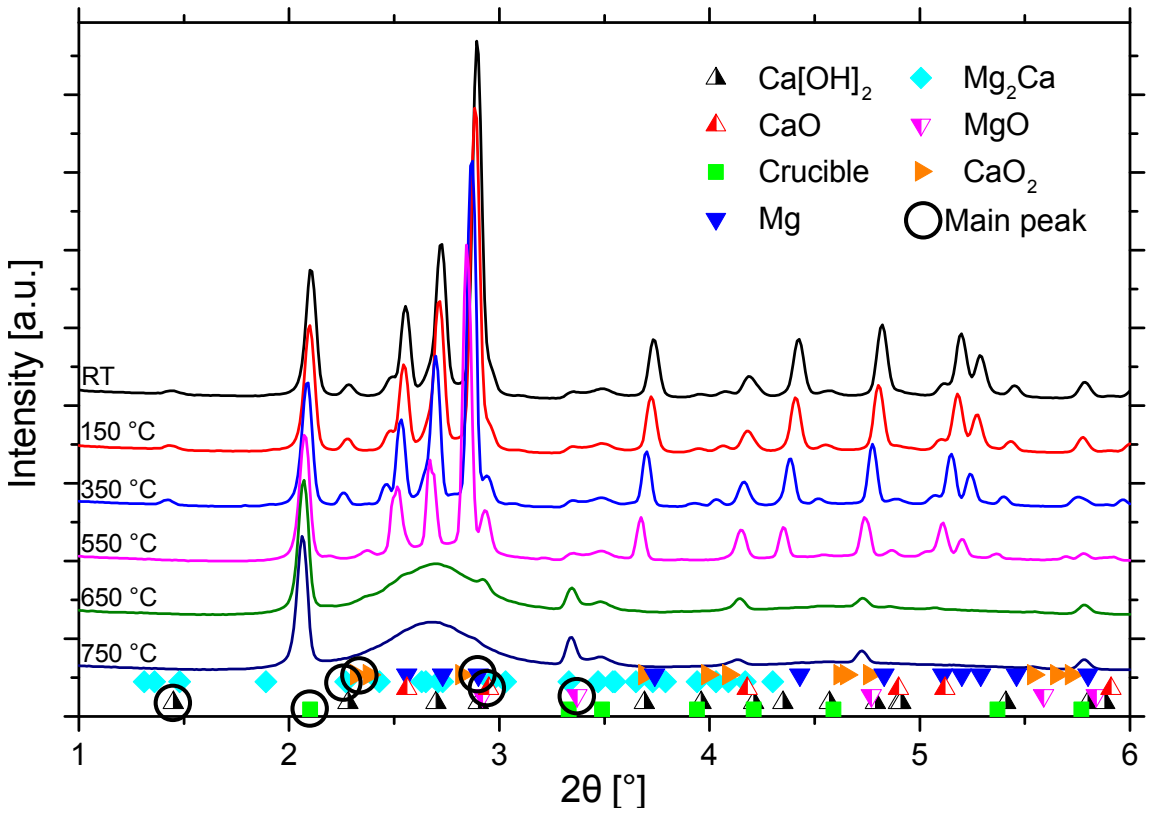

(a) Heating

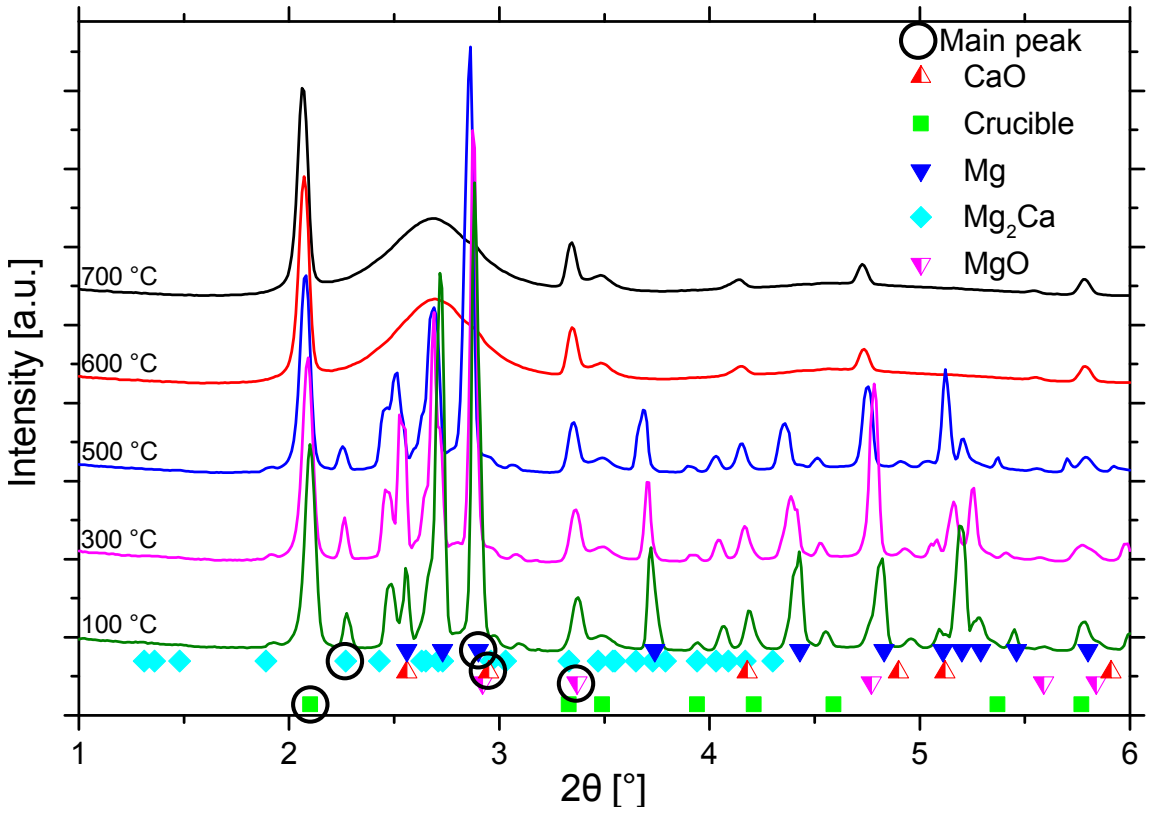

(b) Cooling

Fig. 5.7: Selected line profiles during a) heating and b) cooling of the sample Mg6Ca+6CaO.

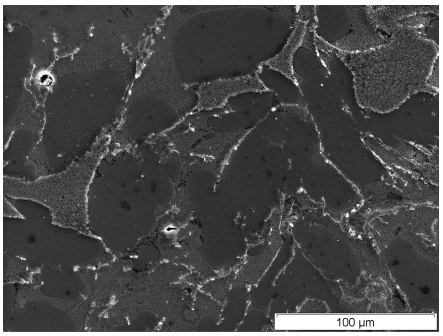

(a) SE

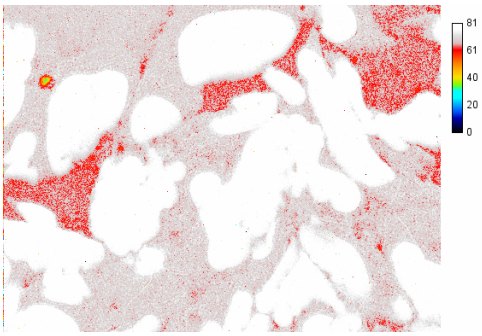

(b) Mg

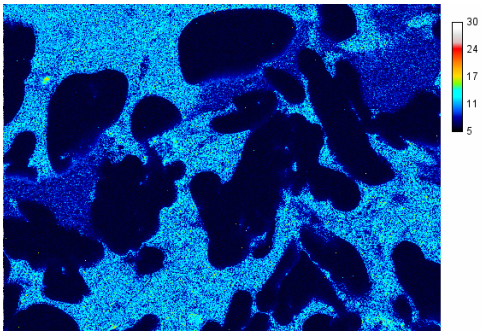

(c) Ca

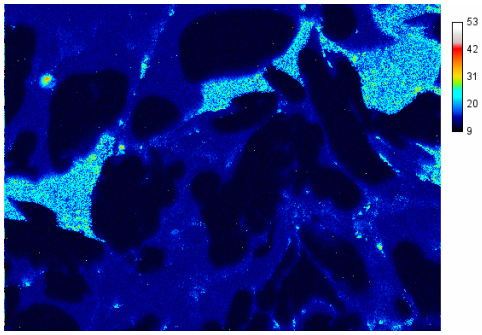

(d) O

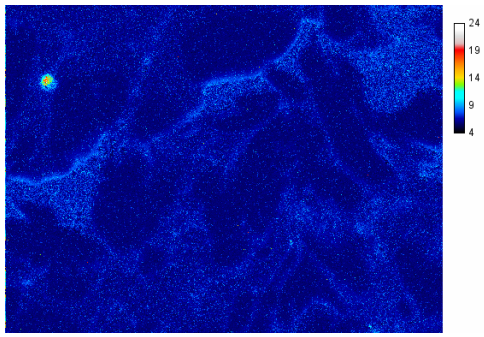

(e) Si

Fig. 5.8: The (a) SE micrograph and EDXS maps for (b) Mg, (c) Ca, (d) O and (e) Si of Mg6Ca+6CaO. (The composition in $wt.\%$.)

5.7 Mg16Ca+6CaO

The temperatures at which phases appear or disappear are listed for Mg16Ca+6CaO in Tab. 5.6 and the LP at different temperatures are illustrated in Fig. 5.9.

Tab. 5.6: Phase changes with temperatures in the sample Mg16Ca+6CaO. The abbreviation (H) for heating and (C) for cooling.

Reaction	Experimental data $\pm$ 5 [$^{\circ}C$]
Disappearance $Ca[OH]_2$ start	234 (H)
Disappearance of $Ca[OH]_2$ end	382 (H)
Appearance of phase CaO_2 start	444 (H)
Decrement of CaO start	481 (H)
Appearance MgO start	481 (H)
Disappearance of Mg_2Ca start	497 (H)
Disappearance of Mg start	497 (H)
Disappearance of Mg_2Ca end	512 (H)
Disappearance of Mg end	574 (H)
Disappearance of CaO_2 end	750 (H)
Decrement of CaO end (stable)	750 (H)
Appearance MgO end (stable)	759 (H)
Appearance of Mg start	533 (C)
Appearance of Mg_2Ca start	510 (C)
Appearance of Mg end	507 (C)
Appearance of Mg_2Ca end	507 (C)

The X-ray line profiles show that $Ca[OH]_2$, CaO, Mg, Mg_2Ca and graphite from the crucible are present in the beginning. During heating the peaks of $Ca[OH]_2$ decrease starting at a temperature of 234 $^{\circ}C$ and disappear from 382 $^{\circ}C$. CaO_2 peaks appear at 444 $^{\circ}C$. The peaks of CaO started to decreases at the same temperature where the MgO peaks were first detected, at 618 $^{\circ}C$. During heating the peaks of Mg and Mg_2Ca decrease from 497 $^{\circ}C$. Followed by the complete disappearance of Mg_2Ca at 512 $^{\circ}C$ and Mg at 574 $^{\circ}C$. A diffuse contrast of the melt was detected with the disappearance of Mg. The peaks of CaO_2 disappeared at the same temperature at which CaO peaks became stable, at 750 $^{\circ}C$. During holding the intensity of MgO peaks became stable at 759 $^{\circ}C$. During cooling the first peaks of Mg was detected at 533 $^{\circ}C$ and no intensity change was detected below 507 $^{\circ}C$. The Laves phase, Mg_2Ca, was detected at 510 $^{\circ}C$ with no further

intensity change below 507 $°C$.

The Fig. 5.10 shows the microstructure of the Mg16Ca+6CaO sample with SEM. The EDXS maps show the distribution of the elements Mg, Ca, O and Si in the solidified sample. From the microstructure the solidification sequence is determined. The solidification begins with Mg grains and ends finally with a eutectic solidification of Mg and Ca rich lamellar structure. The O agglomerates in the eutectic region are clusters of oxide particles. Mg and Ca rich regions in the O rich region can be distinguished. In some regions the O rich particles drop out of the sample during preparation, and generate pits. The final composition was measured using EDXS and found to be with 15.3 ± 3.1 $wt.\%$ Ca, 6.1 ± 1.2 $wt.\%$ O and balance Mg. The Si is from the polishing solution (OPS) on the surface of the polished sample was not used to calculate the composition. This composition deviates from the nominal content of 20.3 $wt.\%$ Ca, 1.7 $wt.\%$ O and balance Mg.

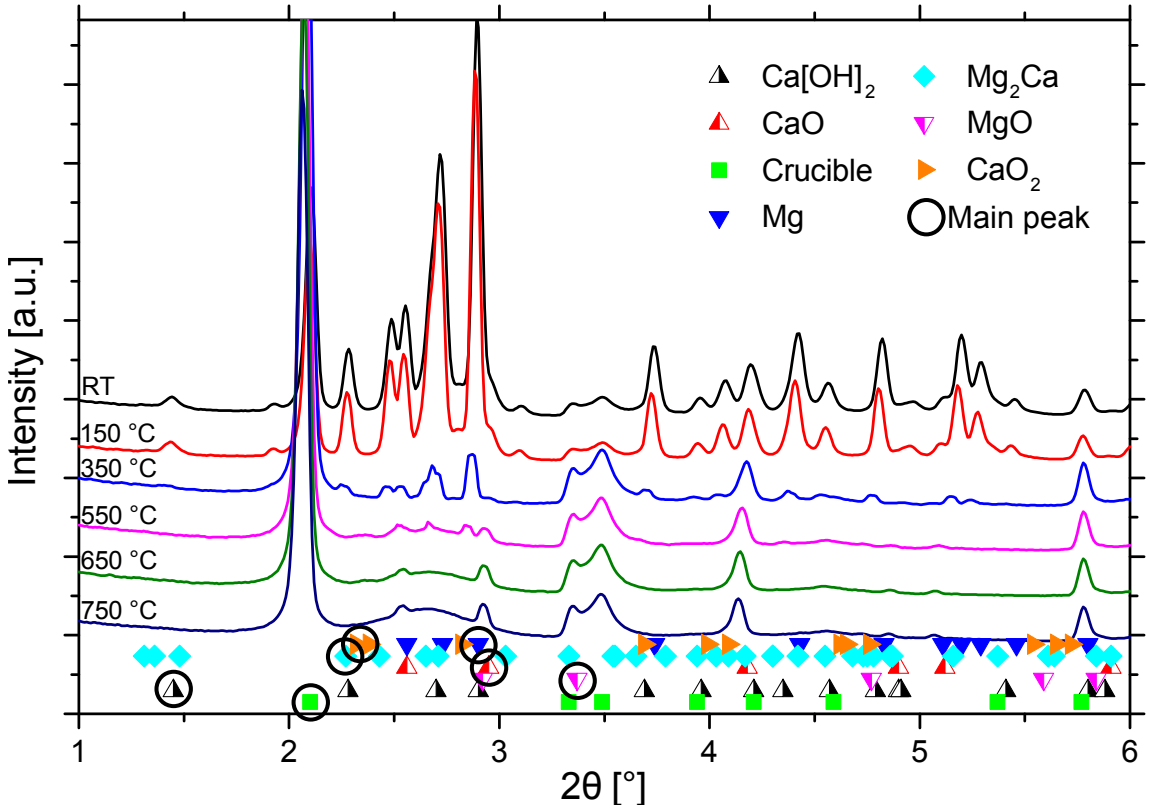

(a) Heating

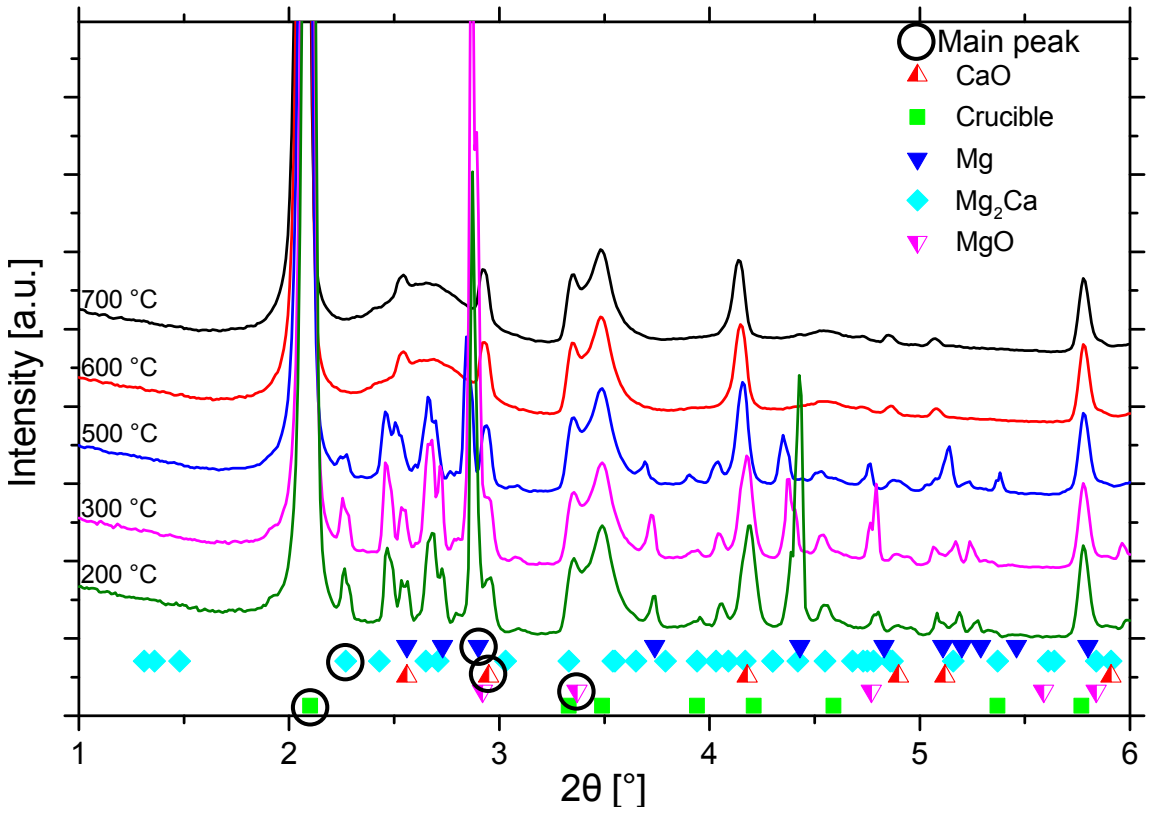

(b) Cooling

Fig. 5.9: Selected line profiles during a) heating and b) cooling of Mg16Ca+6CaO.

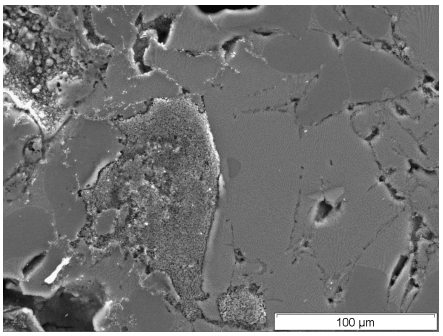

(a) SE

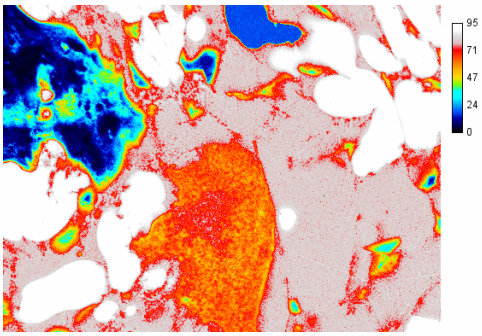

(b) Mg

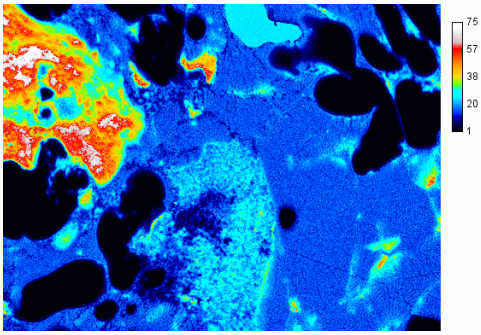

(c) Ca

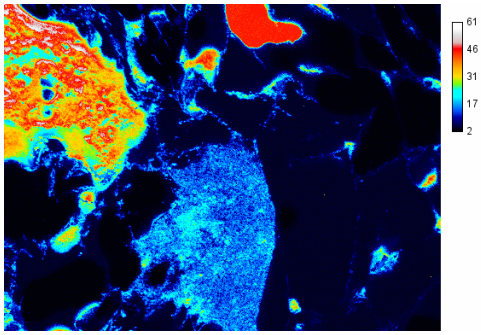

(d) O

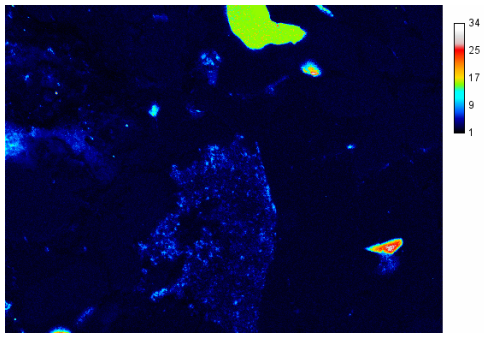

(e) Si

Fig. 5.10: The (a) SE micrograph and EDXS maps for (b) *Mg*, (c) *Ca*, (d) *O* and (e) *Si* of Mg16Ca+6CaO. (The composition in *wt.*%.)

CHAPTER 6

Discussion

6.1 Melting and solidification of pure Mg

Mg melts between 651.6 and 654.2 $^{\circ}C$ and solidifies between 649.1 and 647.0 $^{\circ}C$. According to literature the melting temperature of Mg is at 650 $^{\circ}C$ [29] and the accuracy of measurement is ± 5 $^{\circ}C$ in this experimental setup. The delay in the melting and solidification process is due the kinetics associated with nucleation growth of Mg. This is related to the time that the Mg atoms need to reorganizes themselves for the phase transition from solid to melt and reverse, which results in heating over the required temperature as well as undercooling. It is also possible that the heat flow from the sample through the lid to the thermocouple show a slightly lower temperature. The O content of the pure Mg chips dose not affect the solidification temperature during the heating and cooling. The non statistical distributions of peaks (Fig.5.1) indicate that only few Mg crystals are in Bragg condition. This is related to the small number of nucleation sites in pure Mg, which minimise the number of grains in the measured volume. This is also related to the slower cooling rate and the grain growth that lead to a non-random distribution of grain orientations.

6.2 Reaction during heating

6.2.1 MgxCaO (x = 20 and 30 $wt.\%$)

The X-ray line profiles from the synchrotron investigation show for the samples of Mg20CaO and Mg30CaO, that $Ca[OH]_2$ and CaO are present in the beginning. The CaO was dried before the sample preparation, but $Ca[OH]_2$ forms on CaO due to the humidity in air during the sample production and during storing. This is due to the highly hydrophilic nature of CaO. [46–49]

The dissociation of $Ca[OH]_2$ in all CaO containing samples starts before Mg melts. The dissociation temperature for $Ca[OH]_2$ is at 512 $°C$ [47]. The Tab. 6.1 lists the dissociation temperatures of $Ca[OH]_2$ in Mg20CaO and Mg30CaO samples and are illustrated in Fig. 6.1. The Mg20CaO values show that the dissociation of $Ca[OH]_2$ started before 512 $°C$, at 408 $°C$, and disappear completely by 500 $°C$. The literature values are for $Ca[OH]_2$ only and not in the presence of Mg. It is possible that Mg decrease the temperature for the dissociation of $Ca[OH]_2$, due to a catalytic influence of Mg on the dissociation of $Ca[OH]_2$.

Tab. 6.1: Phase formation temperatures detected during heating from Mg20CaO, and LP numbers for Mg30CaO.

		Mg20CaO	Mg30CaO
$Ca[OH]_2$	Disappearance start	408	165
	Disappearance end	500	204
CaO_2	Appearance	340	132
	Disappearance	618	259
CaO	Disappearance start	568	263
	Stable	664	309
MgO	Appearance	340	163
	Stable	618	204
	Increment	-	225
	Stable	-	339
Mg	Melting starts	620	257
	Melting ends	637	267
		T ± 5 [$°C$]	LP no.

Before $Ca[OH]_2$ dissociates CaO_2 phase was detected. CaO_2 has been reported to be

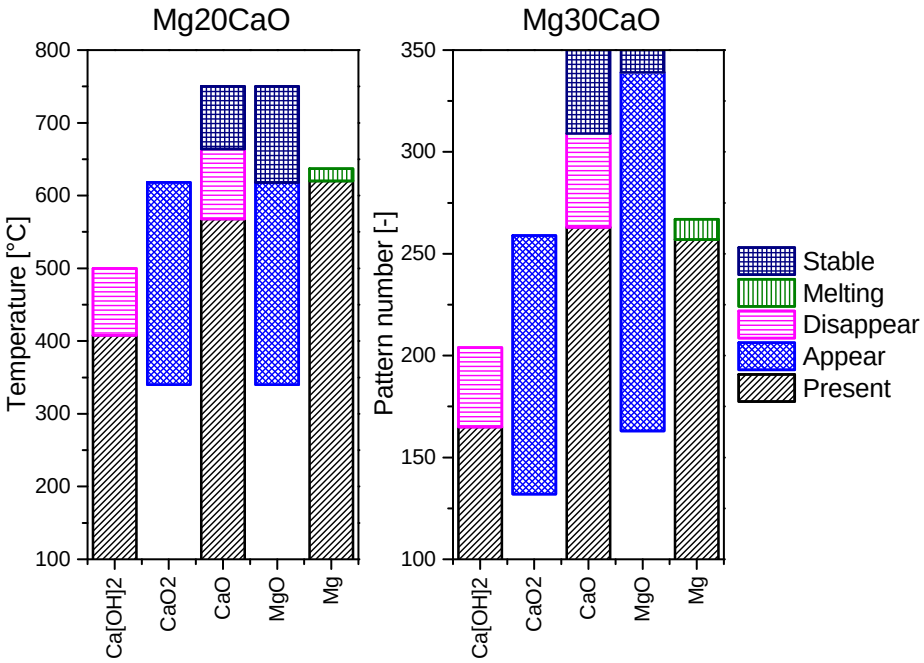

Fig. 6.1: Phase formation detected during heating of Mg20CaO with temperatures and of Mg30CaO with pattern number. Values from Tab. 6.1.

a byproduct of the thermal dissociation of $Ca[OH]_2$ in the presence of P_2O_5 (high O_2 partial pressure) [48]. The temperature delay between the beginning of dissociation of $Ca[OH]_2$ and appearance of CaO_2 is most likely related to the smaller volume of CaO_2 at the start. The peak (0,0,2) at 2.38 ° of CaO_2 is the only peak without any significant overlap with other reflections, but is it close to the peak (1,0,0) at 2.28 ° of $Ca[OH]_2$. The appearance of CaO_2 may be due to interaction with CaO or due to conversion of small amount of $Ca[OH]_2$, the change which is not detected.

When $Ca[OH]_2$ start to dissociate and CaO_2 detected, the first peaks of MgO were also detected. So that Mg react with the O out of $Ca[OH]_2$ and after this with CaO_2. This shows that MgO is more stable than CaO_2. The metastable CaO_2 dissociate into CaO and the free O react with Mg to MgO. These reactions happen at the same time, and it is not possible to distinguish which is the dominant reaction in this reaction chain. In the last step of the dissociation of CaO, the main fraction of CaO dissociate and react to form MgO. The range in which the reaction occur are slightly different in the Mg20CaO compared with Mg30CaO.

The first MgO peaks appear at the same temperature as CaO_2 in the Mg20CaO sample

at 340 °C and the peaks of MgO reach a maximum intensity and is stable at 618 °C. The CaO_2 disappears at the same temperature. According to the literature CaO_2 dissociate below 300 °C [46], but it was detected at 340 °C. In this case CaO_2 forms from the dissociation of $Ca[OH]_2$. The dissolution of CaO started at 568 °C, before the Mg melts at 620 °C and the dissolution speed increased in the molten Mg (up to 637 °C) and peak intensities of CaO became stable (not zero) at 664 °C. In case of Mg30CaO the MgO peaks appear later than the CaO_2 peaks and the dissociation of CaO stopped (not zero) before peaks of MgO became stable. A small amount of CaO stays in the melt of Mg20CaO and Mg30CaO, which is related to kinetics of dissociation as well as saturation of Mg liquid. It is proposed, that in this state a reaction layer enriched with high concentration of MgO forms around CaO particles with a critical layer thickness. This reaction product around the CaO particles decrease the diffusion of Mg ions from the melt to these particles or only a certain amount of CaO can be dissociation in molten Mg.

In case of Mg30CaO the first MgO peaks appear at LP 163. In Mg30CaO show a stabilisation of the peak intensity between LP 204 and 225 with a second increment up to LP 339 this is unlike Mg20CaO where a single increment in the intensity was observed. The fist increment in Mg30CaO occurs in the same range than the dissociation of $Ca[OH]_2$, but the second increment is correlated with the dissociation of CaO_2 and CaO.

According to literature the melting temperature of Mg is 650 °C [29] and the experiment shows melting between 620 and 637 °C for Mg20CaO. The melting range of 17 °C indicates the solid state reaction between Mg and Ca containing phases. After Mg reduced the CaO, Ca diffuse into solid Mg. The Ca in Mg reduce the melting temperature as observed in the binary Mg-Ca system. In contrast to Wiese et. al [158] in this work Mg_2Ca Laves phase was not detected. This relates to the preparation of sample in previous investigations where Mg chips and CaO powder mixture was not compacted. During the reaction between the solid Mg and CaO MgO and Ca form and the Ca diffuse in to the solid Mg. When the Ca concentration is low a solid solution forms, when Ca concentration is above the solubility limit Mg_2Ca Laves phase form. The diffusion in

the non-compacted Mg chips and CaO powder sample observed by Wiese et al. [158] is close to unidirectional diffusion, due to the plate like geometry (2D) of the Mg chips. This decreases the time required to reach the solid solution limit. In this investigation compacted samples are likely to provide a multi-directional diffusion thus only a solid solution forms. Kondoh et al. [1] proposal for the dissociation of CaO in Mg-Al alloys can not be applied in this situation. Kondohs theory proposed the formation of the Laves phase Al_2Ca during in the dissociation of CaO. The present investigation shows that pure Mg is able to dissociate CaO with out the formation of the Laves phase Mg_2Ca. The conclusion from Kondoh et al. [1] is that not the formation of Laves phases that reduce the energy of the system, but the enthalpy of mixtures, that effect the actual phase formation as well the dissociation of CaO.

When it is assumed that the oxides do not effect the melting temperature in the Mg-Ca system, it is possible to determine from the binary Mg-Ca system the amount of Ca, which is in the solid solution in Mg from the temperature at which the liquid forms. For this the Pandat 8.1 software with PanMag8 database was used. The melting range of Mg20CaO was measured to be between 620 $°C$ and 637 $°C$. Melting start at 620 $°C$ at which, a Ca content of approximately 0.1 $wt.\%$ Ca is soluble in Mg. The accuracy of the temperature with ± 5 $°C$ resulted in a accuracy for the Ca content of ± 0.02 $wt.\%$ in this case. The Ca is completely in solution at 637 $°C$ at which the Ca content at the liquidus is 2.2 $wt.\%$ ± 0.9 $wt.\%$. This suggested that in the semi-solid region more Ca is incorporated in to Mg. This is likely to be due to increased diffusion of Ca associated with increased temperature, and the enhancement in the diffusion of Ca to solid Mg through liquid Mg. The amount of Ca in solid solution increased in the melting range by a factor of approximately 22, according to the composition of Ca at the liquidus. The dissociation of CaO during the melting of Mg, increase the amount of Ca dissolved in the system.

6.2.2 MgxCa+6CaO (x = 6 and 16 $wt.\%$)

The X-ray line profiles show, for the samples of Mg6Ca+6CaO and Mg16Ca+6CaO, that $Ca[OH]_2$ and CaO present in the beginning. The $Ca[OH]_2$ forms during sample preparation due to the highly hydrophilic nature of CaO, as explain in Section 6.2. [46–49]

The dissociation of $Ca[OH]_2$ in all Ca and CaO containing samples started and ended before the Mg-Ca alloys melt. The dissociation temperature $Ca[OH]_2$ is lower than 512 $°C$ [47], due to the same reasons as provided in Section 6.2. The Tab. 6.2 lists the dissociation temperatures of Mg6Ca+6CaO and Mg16Ca+6CaO for $Ca[OH]_2$ and these temperatures are illustrated in Fig. 6.2. In Mg6Ca+6CaO the dissociation of $Ca[OH]_2$ started at 350 $°C$ and in Mg16Ca+6CaO at 234 $°C$. The $Ca[OH]_2$ disappeared completely by 433 $°C$ in Mg6Ca+6CaO and at 382 $°C$ in Mg16Ca+6CaO. The literature values are only for the single component $Ca[OH]_2$ and not in a system with Mg. The presence of Mg and Ca are likely to decrease the temperature for the dissociation of $Ca[OH]_2$, due to a catalytic influence of Mg and Ca on the dissociation of $Ca[OH]_2$. Compared with the Mg20CaO the dissociation started and ended at lower temperatures. It is possible that the metallic Ca is more effective than Mg in increasing the driving force for the dissociation. This can explain also that the same amount of CaO and $Ca[OH]_2$ become dissociated faster in the Mg16Ca+6CaO sample than in the Mg6Ca+6CaO sample.

Before $Ca[OH]_2$ started to dissociate CaO_2 phase was detected in the Mg6Ca+6CaO sample. This may be contrasted with the Mg16Ca+6CaO as well Mg20CaO and Mg30CaO samples. In case of the Mg16Ca+6CaO, the CaO_2 phase was detected at a higher temperature than in for Mg20CaO and Mg30CaO samples. As mentioned in Section 6.2, the formation of CaO_2 was reported to be abyproduct of the thermal dissociation of $Ca[OH]_2$ in the presence of P_2O_5 (high O_2 partial pressure) [48]. The temperature delay between the dissociation start of $Ca[OH]_2$ and appearance of CaO_2 is mostly related to low volume of these phase for the diffraction measurements. It is expected that the volume fraction of CaO_2 and of $Ca[OH]_2$ in Mg6Ca+6CaO Mg16Ca+6CaO samples are lower than that observed in the Mg20CaO and Mg30CaO samples, which make the detection during the

Tab. 6.2: Phase formation temperatures detected during heating from Mg6Ca+6CaO and Mg16+6CaO.

		Mg6Ca+6CaO	Mg16Ca+6CaO
$Ca[OH]_2$	Disappearance start	350	234
	Disappearance end	433	382
CaO_2	Appearance	351	444
	Disappearance	667	750
CaO	Disappearance start	589	481
	Stable	671	750
MgO	Appearance start	486	481
	Stable	675	759
Mg	Melting start	504	497
	Melting end	602	574
Mg_2Ca	Disappearance start	504	497
	Disappearance end	506	512
		T $\pm$ 5 $[°C]$	T $\pm$ 5 $[°C]$

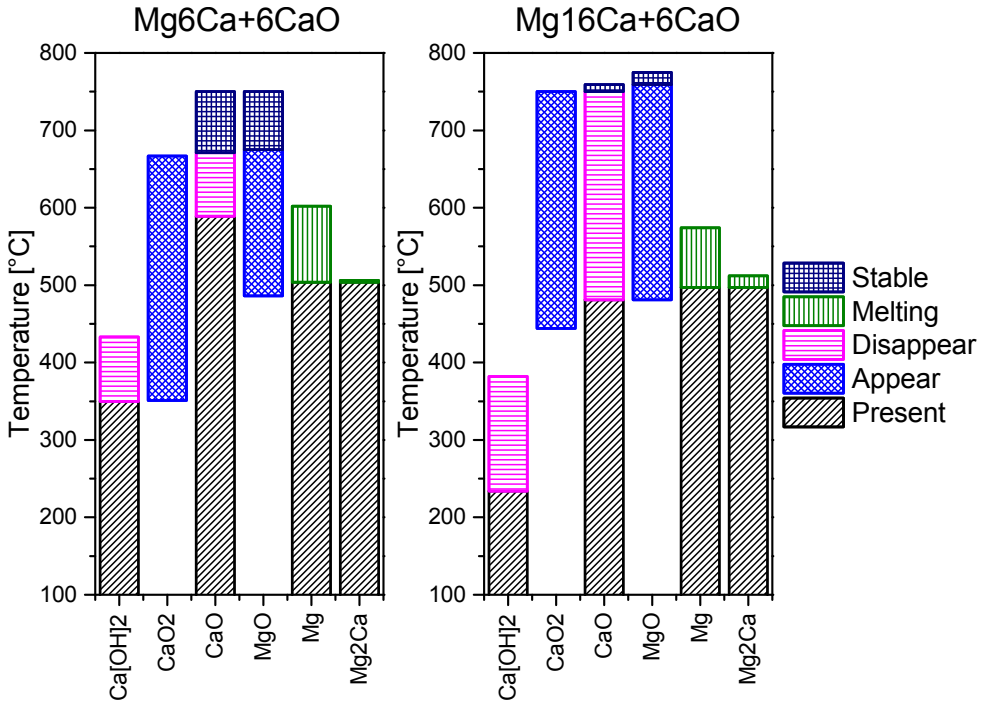

Fig. 6.2: Phase formation detected during heating of Mg20CaO, Mg6Ca+6CaO and Mg16Ca+6CaO. Values from Tab. 6.2.

dissociation or formation of these phases difficult.

The first peaks of MgO were detected in Mg6Ca+6CaO and Mg16Ca+6CaO at higher temperatures, than in the Mg20CaO and were detected after the detection CaO_2. MgO was detected in Mg6Ca+6CaO at 486 $°C$ and in Mg16Ca+6CaO at 481 $°C$, which are relativey close temperatures. These are contrasted with Mg20CaO, as Mg did not react with O from $Ca[OH]_2$ or the amount of MgO formation is below the threshold for the detection, the amount of CaO as well as $Ca[OH]_2$ and CaO_2 are lower than in Mg20CaO. The Mg react with the O out of CaO_2 and CaO. The metastable CaO_2 dissociate in to CaO and the free O react with Mg to MgO. This reactions happen at the same time and it is not possible to distinguish which is the dominant reaction in this reaction chain. The range of temperature at which this reaction occurs is slightly different in the Mg6Ca+6CaO and Mg16Ca+6CaO samples. The CaO_2 dissociation ends at 667 $°C$ in Mg6Ca+6CaO and at 750 $°C$ in Mg16Ca+6CaO, which is a higher temperature than for Mg20CaO at 618 $°C$. According to the literature CaO_2 should dissociate below 300 $°C$ [46]. As CaO_2 forms from the dissociation of $Ca[OH]_2$ at higher temperatures the presence of other phases are likely to stabilises the CaO_2. The first MgO peaks appear in Mg6Ca+6CaO and Mg16Ca+6CaO at similar temperatures. In Mg16Ca+6CaO the peak intensity of MgO stabilises at 675 $°C$ and in Mg16Ca+6CaO during holding at 750 $°C$, which are higher temperature than in Mg20CaO at 618 $°C$. This could be related to a lower diving force for the dissociation of CaO, due to a presence of Ca in the MgxCa+CaO samples.

The dissolution of CaO start at 589 $°C$ in Mg6Ca+6CaO and stabilised (not zero) together with the dissolution of CaO_2 and the stabilisation of MgO at approximately 670 $°C$. The dissolution of CaO started at 481 $°C$ in Mg16Ca+6CaO and stabilised (not zero) together with the dissolution of CaO_2 and the stabilisation of MgO at approximately 750 $°C$. The appearance of CaO_2 in Mg6Ca+6CaO occurs at a lower temperature compared with Mg16Ca+6CaO, this could be due to the higher amount of Mg in Mg6Ca+6CaO compared with Mg16Ca+6CaO. This leads the formation of MgO in Mg6Ca+6CaO and the formation of CaO and MgO due to the CaO_2 dissociation in Mg16Ca+6CaO. So that CaO dissociates in Mg6Ca+6CaO at 598 $°C$ when a larger amount of Mg is molten.

The dissociation speed of CaO is higher and related to the higher diffusion rate in the molten state. In Mg16Ca+6CaO the dissociation start of CaO was detected at the same temperature when first MgO peaks were detected at 481 $°C$. The driving force for the dissociation of CaO is lower due to the higher amount of Ca. The lower melting range leads to a faster increase of the liquid fraction in the sample. When the amount of liquid is higher, the driving force for the diffusion is lager and dissociation speed of CaO increases. The phase formation temperatures for MgO (stabilisation), CaO (stabilisation, not zero) and CaO_2 (dissolution) occurs in both samples at the same temperature, so that the phase formation sequence is the same but it ends at a higher temperature with the higher Ca content. As proposed before, the reaction products from around the CaO particles decreasing the diffusion of Mg from the melt to these particles, which results in relation of CaO particles in the melt.

According to the calculation from Pandat 8.1 software with the PanMag8 database and the literature (Tab. 3.2) [31,33,35,36] the eutectic temperature Mg-Ca system is approximately 516 $°C$. The first melt were detected at 504 $°C$ in Mg6Ca+6CaO and 497 $°C$ in Mg16Ca+6CaO, these temperatures are lower than the eutectic temperature of the binary Mg-Ca system on the Mg rich side. The first detection of the liquid was determined as the appearance of the diffuse background due to molten metal and the decrease in the intensity of Mg and Mg_2Ca peaks. The decreases in the intensity of Mg is only result in a small change in the LP. However, the disappearance of the Mg_2Ca peaks are unique and free of any interpretation. The slight decrease in the intensity of the Mg_2Ca peak could be also related to the dissolution of Mg_2Ca into Mg. The Mg_2Ca peaks disappear at 506 $°C$ in Mg6Ca+6CaO and at 512 $°C$ in Mg16Ca+6CaO. In case of Mg16Ca+6CaO the detected temperature is within the error in measurement ± 5 $°C$ form Section 6.1. However, this can not explain the lower eutectic temperature in the Mg6Ca+6CaO. It is possible that there is slower heat flow from the sample through the lid to the thermocouple thus a lower temperature is detected. It is also possible that the temperature distribution is not uniform, e.g. the outer layer of the sample is warmer and partially molten. This is related to the heat conductivity and the heat flow inside the sample, and non uniform

distribution of metallic phases and oxides with different heat conductisvities.

The increase in the Mg_2Ca Laves phase during the dissociation of CaO could not be verified, due to the high Ca content in Mg6Ca+6CaO and Mg16Ca+6CaO and the presence of Mg_2Ca. Thus, the Ca containing samples could not be used to verify the experimental results of Wiese et al. [158] and of Kondoh et al. [1]. However, the results from Mg20CaO and Mg30CaO with higher CaO contents did not show the formation of Mg_2Ca during heating.

If we assume that the oxides did not affect the melting temperature in the Mg-Ca system, the eutectic temperature in the metallic Mg-Ca is approximately 516 $°C$. The liquidus of Mg6Ca is 613 $°C$ and Mg16Ca is 520 $°C$, this is not in agreement with the measured temperatures. The measured temperatures are slightly lower, at 602 $°C$ for Mg6Ca+6CaO and 574 $°C$ for Mg16Ca+6CaO . This decrease in the liquidus temperature is is likely to be due to the formation of MgO, which increase in the amount of Ca in the melt due to the reduction of CaO, CaO_2 and $Ca[OH]_2$. Due to the reduction of available Mg in the melt with the formation of MgO, the amount of Ca effectively higher in the melt. The result is that the composition is closer to the eutectic composition, which reduced the melting range.

It is possible determine from the binary Mg-Ca system the amount of Ca, which is in solution with Mg at liquidus the temperature. The liquidus temperature of Mg6Ca+6CaO was measured at 602 $°C$, which correspond to a Ca content of approximately 7.4 $wt.\%$. The accuracy of the temperature measurement with ± 5 $°C$ resulted in a accuracy for the Ca content of $-0.7/+0.6$ $wt.\%$ in this case. The liquidus temperature of Mg16Ca+6CaO was measured at 574 $°C$, which correspond to a Ca content of approximately 10.6 $wt.\%$. The accuracy of the temperature measurement with ± 5 $°C$, resulted in a accuracy for the Ca content of $-0.7/+0.6$ $wt.\%$ in this case. The liquidus temperature of Mg6Ca+6CaO is lower than that of pure Mg6Ca, so that the Ca content has increased during heating. This is attributed to the dissociation of CaO in and incorporation of Ca into the alloy. This shows that a Ca content of 6 $wt.\%$ at the start condition compared with the composition of the liquidus with composition with 7.4 $wt.\%$, results in an increment of 1.4 $wt.\%$. The

results form Mg6Ca+6CaO are in a good agreement with the results from Mg20CaO. At the liquidus of Mg20CaO shows the incorporation of CaO into semi-solid Mg in the solid state and a enrichment of Ca in to Mg. In the case of Mg16Ca+6CaO the melting need more time which resulted in a higher melt temperature. Thus, the liquidus temperature correspond to a lower Ca content, compared with that in the binary Mg-Ca system. This due to the Mg_2Ca in the alloy prior to the experiment which has decreased the content of Ca dissolved in Mg significantly.

6.3 Reaction during cooling

6.3.1 MgxCaO (x = 20, 30 and 50 $wt.\%$)

The during solidification of the samples intensity changes was not observed for MgO and CaO, in Mg20CaO and Mg30CaO. This indicate that MgO is more stable than the CaO in the Mg rich corner of the ternary Mg-Ca-O system and it is possible the CaO dissociate up to a certain amount in Mg alloys. A small amount of CaO remained after melting. However, the main oxide phase observed during solidification is MgO, as indicated by the higher intensity of the MgO peaks compared with CaO. A phase transition from CaO to MgO during the solidification under equilibrium conditions is a possible reaction, but a slow solid-state diffusion can resulted in non-equilibrium condition with a major fraction of MgO.

The Tab. 6.3 lists the solidification sequence of the Mg20CaO and Mg30CaO samples with the start and end temperatures as well LP number for various phase formation and this is illustrated in Fig. 6.1. In the case of Mg20CaO and Mg30CaO the solidification begins with Mg and ends with the eutectic solidification of Mg and Mg_2Ca. The final solidification is eutectic reaction related to the disappearance of the background from the molten metal and the appearance of Mg_2Ca. The solidification of Mg20CaO starts at 570 $°C$ with Mg and ends with the formation of Mg_2Ca at 511 to 509 $°C$. The eutectic appearance of Mg_2Ca at approximately 510 $°C$ at a temperature 6 $°C$ lower than that

reported in literature (approximately 516 $°C$, Tab. 3.2) [31, 33, 35, 36]. This temperature difference in forming of Mg_2Ca is likely to be associated with undercooling required to form Mg_2Ca, but it is within the accuracy of measurement, ± 5 $°C$. The explanation in this case is that energy causes barrier to formation of Mg_2Ca to form at a slightly lower temperature compared with eutectic temperature of the Mg-Ca system. The deviation from the eutectic temperature is relatively small to that detected in the binary Mg-Ca system. Due to the failure described in Section 5.4 only the LP number was used to follow the solidification in the sample Mg30CaO. However, the solidification sequence of Mg30CaO starts the formation of Mg and then the eutectic Mg and Mg_2Ca structure forms similarly to the Mg20CaO. Based on the results from Mg20CaO sample the eutectic formation temperature is assumed to be the similar and that O only has a negligible effect on the formation temperature. The presence of MgO reduce the amount of free Mg in the melt by forming MgO. This increased the Ca content in the melt in relation to Mg, which will lower the temperature for the formation of α-Mg, as the rest of the melt has a composition closer to the eutectic composition of the binary Mg-Ca system.

If we assumed that the oxides did not affect the solidification temperature in the Mg-Ca system. It is possible to determine the amount of Ca in solid solution from the binary Mg-Ca system, as described in Section 6.2. The start of the solidification of Mg20CaO was measured at 570 $°C$ and the eutectic solidification of Mg and Mg_2Ca at 510 $°C$. From the start of the solidification of Mg at 570 $°C$, the Ca content in the melt is approximately 11.0 $wt.\%$. If the solidus line at 570 $°C$ was considered the $\alpha - Mg$ forms with a Ca content of ≈ 0.2 $wt.\%$. The accuracy of the temperature with ± 5 $°C$ resulted in a accuracy for the Ca content of $-0.5/+0.6$ $wt.\%$ in this case. The eutectic formation of the metallic phases was detected at 510 $°C$, at the eutectic temperature the Ca of the remaining liquids is content is 16.3 $wt.\%$.

The nominal composition of the samples deviate from that measured using SEM-EDXS. The measurement with EDXS, contain inaccuracies associated with the measuring of light elements, e.g. O. Due to the small sample size from synchrotron radiation experiment, other analytical techniques such as inductively coupled plasma optical emission spec-

Tab. 6.3: Phase formation during cooling for Mg20CaO with temperatures and for Mg30CaO with pattern number. Illustrated in Fig. 6.1.

		Mg20CaO	Mg30CaO
Mg	Solidification start	570	406
	Solidification end	509	409
Mg_2Ca	Solidification start	511	407
	Solidification end	509	407
		T $\pm$ 5 [$°C$]	LP no.

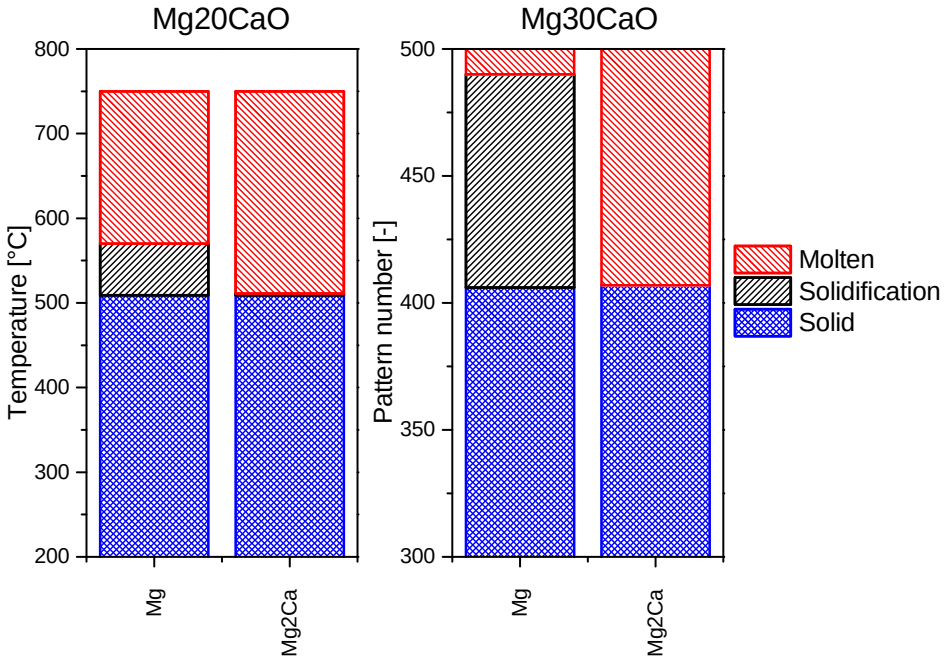

Fig. 6.3: Detected phase formation during heating of Mg20CaO and Mg30CaO. Values from Tab. 6.1.

troscopy (ICP-OES) could not be used to accurately determine the O concentration. In all three samples the measured Ca content was lower than the nominal composition. The deviation between nominal and measured content of O for the Mg20CaO higher than that expected but for Mg30CaO and Mg50CaO lower than that expected from the nominal composition. The higher O content of the Mg20CaO compared with the nominal composition is related to the higher O content of the pure Mg chips. However, the lower O content of the Mg30CaO and Mg50CaO samples compared the nominal composition is related to the formation of $Ca[OH]_2$ and possible loss of CaO during the sample production, given the Ca content is lower than expected. The lower Ca content in Mg20CaO sample is also due to possible loss of CaO during during preparation.

Tab. 6.4: The nominal and measured of the compositions for Mg20CaO, Mg30CaO and Mg50CaO samples. Deviations between nominal and measured compositions are also indicated.

Sample	Composition	Ca [$wt.\%$]	O [$wt.\%$]	Mg [$wt.\%$]
Mg20CaO	nominal	14.3	5.7	80.0
	measured	6.8 ± 1.4	8.7 ± 1.3	84.5
	deviation	-7.5	3.0	4.5
Mg30CaO	nominal	21.4	8.6	70.0
	measured	9.4 ± 1.9	6.4 ± 1.3	84.2
	deviation	-12.0	-2.2	14.2
Mg50CaO	nominal	35.7	14.3	50.0
	measured	12.6 ± 2.5	12.8 ± 2.6	74.6
	deviation	-23.1	-1.5	24.6

$Ca[OH]_2$ was found at the beginning of the *in situ* experiment. If the $Ca[OH]_2$ formed before weighing, the amount of Ca will be lower and the amount of O higher. For an example 20 $wt.\%$ CaO in Mg has 14.3 $wt.\%$ of Ca and 5.7 $wt.\%$ of O, but 20 $wt.\%$ $Ca[OH]_2$ in Mg contains only 10.8 $wt.\%$ of Ca, 8.6 $wt.\%$ of O and 0.5 $wt.\%$ of H. However, this can not fully explain the lower content of Ca, but the slight increase in O. The ratio between the Ca and O contents for CaO should be approximately 5:2 (in $wt.\%$) and for $Ca[OH]_2$ approximately 5:4 (in $wt.\%$). In all three samples the final content of O is higher than the that, calculated from based on CaO but not as high as that from $Ca(OH)_2$. The argument is that the CaO is not the only source of O in these samples. In the case of Mg30CaO the amount O is so high, that approximately $\frac{4}{5}$ of the Ca is from

$Ca[OH]_2$ and approximately $\frac{1}{5}$ of the Ca from CaO. All samples are produced on the same day, so that the deviation in the $Ca[OH]_2$ and CaO contents for the samples should be not so high. The higher O concentration could be also related to the oxidation of the pure Mg chips during the production and storage these samples, due to the large surface area of the pure Mg chips and the strong driving force for the oxidation.

The lower amount of Ca in the measured composition can be explained by the loss of CaO during the preparation of these samples. Due to the size difference between the pure Mg chips and the CaO powder, the CaO separate easily form the Mg chips. During filling the CaO particles disperse.

If the values is the Tab. 6.4 are used, the total concentration of Ca is 6.8 $wt.\%$, O is 8.7 $wt.\%$ and balance Mg in Mg20CaO sample. With the supposition that O forms only MgO and available from only CaO value for Ca and the rest are Mg and Ca, the concentration was calculated to be Mg 91.3 $wt.\%$ and Ca 8.7 $wt.\%$. As mentioned the EDXS measurement are inaccurate for elements for O. The actual concentration of O higher in the Mg20CaO sample than measured by EDXS, and content of Ca is higher in the Mg-Ca alloy.

The *in situ* results are in agreement with the SEM investigations. The microstructures of Mg20CaO and Mg30CaO samples shows globular to dendritic Mg and the eutectic lamellar structure of Mg and Mg_2Ca. This microstructure is characteristic of the Mg rich side of the binary Mg-Ca system [16, 21, 36]. For the Mg20CaO and Mg30CaO samples of the O agglomerates in the eutectic region in a form of clusters of oxide particles. The EDXS maps show a higher concentration of Mg in the O rich region compared with the O free region in the eutectic structure. Together with the synchrotron X-ray radiation diffraction results these oxide rich regions are identified as major MgO and minor residue of CaO. The location of the oxides within the eutectic regions is due to the primary solidification of Mg. The Mg nuclei grow and the oxide particles agglomerate in the liquid side of solidification front. This moves the oxide particles out of the Mg grains and clusters of these particles form in the melt. Below the eutectic temperature the rest of the melt solidify and encompass the oxide particles between the eutectic structure.

Compared with the samples Mg20CaO and Mg30CaO the Mg50CaO sample shows a different microstructure. The microstructure of the Mg50CaO is mainly dominated by a region with a high content of O. Two types of O rich regions could be determined. One O rich region has a Ca content between 25 to 35 $wt.\%$ and a Mg content of approximately 45 $wt.\%$ with a lower O content. This indicates that this region contain Ca, which seem to be mainly in the form of eutectic with CaO. Due to the higher amount of O compared with the Mg20CaO and Mg30CaO sample, the volume fraction of oxide is higher and is more uniformly distributed. However, as *in situ* measurement was not successful for this sample, and it is not clear if the content of CaO in the solidified sample higher than in the other samples. The second O rich region contained a higher O content with mainly Mg, so that this region mainly consisted of MgO and a minor fraction of CaO.

The samples Mg30CaO and Mg50CaO show a higher content of Ca and O compared to the Mg20CaO sample and a region with mainly CaO in the microstructures. This indicates that a higher amount of CaO can not fully dissociated in the Mg melt and explain the compact CaO agglomerations after the melting.

The metallic regions are embedded with O rich regions. This metallic regions shows globular Mg and the characteristic eutectic lamellar structure containing Mg and eutectic formation of Mg and Mg_2Ca, which is in agreement with the Mg rich side of the binary Mg-Ca system [16, 21, 36]. In this sample the Ca content is higher, which explains the higher volume fraction of the lamellar regions of Mg and Ca.

6.3.2 MgxCa+6CaO (x = 6 and 16 $wt.\%$)

The during solidification of the samples, after holding at 750 $°C$ for 5 min, there is no intensity change for MgO and CaO. This indicates, as with Mg20CaO and Mg30CaO, MgO is more stable than the CaO in the Mg rich corner of the ternary Mg-Ca-O system and it is possible the CaO dissociate up to a certain amount in Mg alloys. A small amount of CaO remain after melting during solidification. However, the main oxide observed during solidification is MgO, as indicated by the higher intensity of the MgO peaks compared with CaO. However, significant intensity decrease was not observed for

CaO peak in Mg16Ca+6CaO as for Mg6Ca+6CaO. A phase transition from CaO to MgO during the solidification under equilibrium conditions is a possible reaction, but a slow solid-state diffusion can resulted in non-equilibrium condition with a major fraction of MgO. As the samples were rotated during the measurement the information is not limited to single view of the sample but provide better statistics of the amount of various phases.

The Tab. 6.5 lists the solidification sequence of the Mg6Ca+6CaO and Mg16Ca+6CaO samples with the start and end temperatures for various phase formation and is illustrated in Fig. 6.4. In the case of Mg6Ca+6CaO and Mg16Ca+6CaO the solidification begins with Mg and ends with the eutectic solidification of Mg and Mg_2Ca, which was detected with *in situ* synchrotron measurements. This is in agreement with the measurements for Mg20CaO and Mg30CaO. The final solidification is an eutectic reaction, related to the disappearance of the background from the molten metal and the appearance of Mg_2Ca. The solidification of Mg6Ca+6CaO starts at 581 $°C$ with Mg and ends with the formation of Mg_2Ca at 504 $°C$, and for Mg16Ca+6CaO at 533 $°C$ and ends between 510 to 507 $°C$. The literature report the eutectic temperature on the Mg rich side of the Mg-Ca system to be approximately 516 $°C$ (Tab. 3.2) [31,33,35,36]). In case of Mg16Ca+6CaO the first formation of the Mg_2Ca occurs with in the range of temperature error (± 5 $°C$). However, the temperature at which Mg_2Ca forms is likely to be associated with non equilibrium cooling. The eutectic transformation of Mg and Mg_2Ca should not show a solidification range according to the phase diagram, but due to energy barriers associated with nucleation and growth of Mg and Mg_2Ca phases this is observed. As result the solidification need more time, which resulted in a lower temperature for the full solidification. According to the results from Mg6Ca+6CaO and Mg16Ca+6CaO and also from Mg20CaO the eutectic formation temperature is assumed to be the same and that O only has a negligible effect on the formation temperature. The Ca content in the melt in relation to Mg is higher due to formation of MgO, which will lower the temperature for the formation of α-Mg, and the rest of the melt has a composition closer to the eutectic composition of the binary Mg-Ca system.

The start of the solidification of Mg6Ca+6CaO occurs at 32 $°C$ lower than the liquidus at 602 $°C$. This temperature difference is outside of the temperature accuracy (± 5 $°C$), but could be explained by the ongoing reduction of CaO after melting. If we assume, that the oxides did not effect the solidification temperature in the Mg-Ca system, it is possible to determine the amount of Ca from the binary Mg-Ca system, as described in Section 6.2. The start of the solidification of Mg of Mg6Ca+6CaO was measured at 570 $°C$, Ca content in the melt is approximately 11.1 $wt.\%$. The accuracy of the temperature measurement is ± 5 $°C$, resulting in an inaccuracy in the Ca content of $-0.6/+0.5$ $wt.\%$. This indicates a increment of the Ca content in the melt by 5.1 $wt.\%$.

In the case of Mg16Ca+6CaO first solidification was measured at 533 $°C$, corresponding to a Ca content in the melt of approximately 14.8 $wt.\%$. The temperature accuracy of ± 5 $°C$ the accuracy of the Ca content is ± 0.5 $wt.\%$. This indicates a decrease in the Ca content in the melt by 1.2 $wt.\%$. This can not be explained by the ongoing reduction of CaO and CaO_2 after melting, but the start of the solidification occurs at a lower liquidus temperature during cooling compared with melting. This difference is approximatively 41 $°C$. The decrease in the solidification temperature indicates a higher content of Ca in the liquid, compared with that present during the melting.

Tab. 6.5: Phase formation temperatures during cooling for Mg6Ca+6CaO and Mg16+6CaO.

		Mg6Ca+6CaO	Mg16Ca+6CaO
Mg	Solidification start	581	533
	Solidification end	504	507
Mg_2Ca	Solidification start	504	510
	Solidification end	504	507
		$\pm$ 5 [$°C$]	$\pm$ 5 [$°C$]

The nominal composition of the samples deviate from that measured using SEM-EDXS. The nominal composition is the composition of alloy chips (Tab. 5.1) and of CaO. The measurement with EDXS is inaccurate O, as mention in a previous Section. However, the nominal and measured (Tab. 6.6) Ca and O contents for Mg6Ca+6CaO sample is in a good agreement. In the Mg16Ca+6CaO sample the content of Ca measured was lower, than the nominal composition. The deviation between nominal and measured O

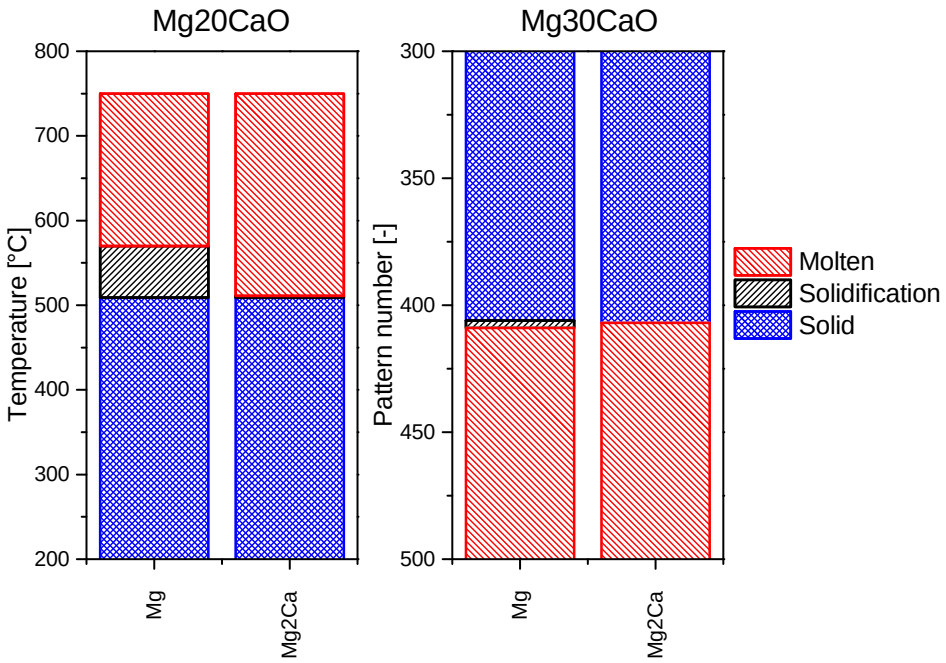

Fig. 6.4: Detected phase formation temperatures during cooling of Mg6Ca+6CaO and Mg16+6CaO. Values from Tab. 6.5.

content higher than that expected from the nominal composition. This deviation from the nominal composition is related to the formation of $Ca[OH]_2$ and the loss of CaO during the sample production, as explain in Section 6.3.1.

Tab. 6.6: The nominal and measured compositions for the Mg6Ca+6CaO and Mg16Ca+6CaO samples. Deviations between nominal and measured compositions are also indicated.

Sample	Composition	Ca $[wt.\%]$	O $[wt.\%]$	Mg $[wt.\%]$
Mg6Ca+6CaO	nominal	9.9	1.7	88.4
	measured	8.2 ± 1.6	4.8 ± 1.0	87.0
	deviation	-1.7	3.1	-1.4
Mg16Ca+6CaO	nominal	19.3	1.7	79.0
	measured	15.3 ± 3.1	6.1 ± 1.2	78.6
	deviation	-4.0	4.4	-0.4

As described for the Mg20CaO and Mg30CaO samples, $Ca[OH]_2$ was present from the beginning of the *in situ* experiment. The presence of $Ca[OH]_2$ decrease the amount of Ca and increased the amount of O in the sample. However, this can not fully explain the lower content of Ca, but the slight increase in O through a small amount of $Ca[OH]_2$. The ratio between Ca and O can not be used as with the MgxCaO samples, to determine the amount of CaO and $Ca(OH)_2$ found, as the samples contain Ca from the beginning. This

make the calculation of the O source impossible. The higher O concentration could be also related to a oxidation of the Mg-Ca chips during the production and storage of these samples, as measured by EDXS. The lower amount of Ca in the measured composition can be explained by the loss of CaO during the preparation of these samples (described in Section 6.3.1).

However, the Ca content of Mg6Ca+6CaO is approximately 11.1 $wt.\%$ (at the liquidus temperature) in the melt. If the values form the Tab. 6.6 are used, the total concentration of Ca is 8.2 $wt.\%$, O is 4.8 $wt.\%$ and balance Mg. With the same correction as before (Section 6.3.1), the concentration of the metallic Mg and Ca are calculated to Mg 90.7 $wt.\%$ and Ca 9.3 $wt.\%$. Compared with the composition from the binary Mg-Ca system to the Ca concentration in Mg from Mg6Ca+6CaO is lower according to the second method. The actual concentration of O was higher in Mg6Ca+6CaO sample than that measured with EDXS, the Ca content is higher in the metallic region. This is the case, if the O content is approximately 10.3 $wt.\%$ the Ca content in metallic region is 11.1 $wt.\%$.

In case of Mg16Ca+6CaO the first Mg solidification was measured at 533 $°C$, a Ca content in the melt is 14.8 $wt.\%$ and relatively close to measured composition. The accuracy of the temperature measurement with ± 5 $°C$ resulted in an accuracy of Ca content at ± 0.5 $wt.\%$ in this case. This indicates a decrease in the Ca content by 1.2 $wt.\%$. This can not explain the reduction of CaO and CaO_2 after melting, but the start of the solidification occurs at a temperature 41 $°C$ lower than the liquidus during heating. The decrease in the solidification temperature indicate a higher content of Ca in the liquid, compared with that during melting. With the same a correction as before, the concentrations of Mg and Ca in the metallic region are calculated to be Mg 81.9 $wt.\%$ and Ca 18.1 $wt.\%$. Compared with the composition from the binary Mg-Ca system the Ca concentration in the metallic region of Mg16Ca+6Ca is higher with the second method. The actual concentration of O is lower in the Mg16Ca+6CaO sample than that measured with EDXS, the Ca content is lower than the concentration in the metallic region. The methods used to calculate the Ca content using the liquidus temperature or with the correction of concentration by the

formation of only MgO using a fixed value for Ca in the metallic region can not be used to evaluate each other, due to the higher deviation as described for Mg20CaO.

The *in situ* results from the MgxCa+6CaO samples are in agreement with the SEM investigations. The microstructure of MgxCa+6CaO samples show globular formation of Mg and the eutectic lamellar structure of Mg and Mg_2Ca. This microstructure is characteristic of the Mg rich side of the binary Mg-Ca system [16,21,36]. In each sample O agglomerates in the eutectic region in a form of clusters of oxide particles. The EDXS maps show a higher concentration of Mg in the O rich region of Mg6Ca+6CaO compared with the O free region in the eutectic structures. Together with the synchrotron X-ray radiation diffraction results, these oxide rich regions are identified as mainly MgO and a minor fraction of CaO. However, the O rich region of Mg16Ca+6CaO show also a high amount of Ca and Mg in the same region. Also the decrease in the intensity of CaO peaks decrease is not as strong as with the other samples. This make the identification difficult. It is not clear whether only MgO, CaO or both was observed in the microstructure. As illustrated in the results section (Fig. 5.10) the Mg rich regions have a concentration of 50 $wt.\%$ Mg and 35 $wt.\%$ Ca, so that the main oxide is MgO. One O rich region has a Ca content between 40 to 75 $wt.\%$ and a Mg content of approximately 10 $wt.\%$ with a high O content. This indicates that a higher amount of CaO can not fully dissociated in the Mg melt and explain the compact CaO agglomerations after the melting in the Mg16Ca+6CaO sample. The location of oxides is in the eutectic regions resulted from the primary solidification of Mg, as described previously.

6.4 Thermodynamic calculations

6.4.1 Calculations in comparison with experimental results

Thermodynamic databases are developed by the Institute of Metallurgy - Thermochemistry & microkinetics group in TU Clausthal based only on the thermodynamic data for CaO and MgO from Hillert and Xizhen [54] and Gourishankar et al. [2]. The first ther-

modynamic calculation is based on the thermodynamic data for CaO and MgO from Hillert and Xizhen [54] (DB1) and the second thermodynamic calculation is based on the thermodynamic data for CaO and MgO from Gourishankar et al. [2] (DB2). In the case of Gourishankar et al. [2] CaO is measured to be thermodynamically less stable than MgO (Fig. 3.3).

Due to the experimental set-up two different O_2 partial pressure are possible depending on whether the crucible is sealed or not. If the crucible is sealed the O_2 pressure increases up to 4 bar during heating but if the crucible is not sealed the O_2 pressure remains at 1 bar. The calculations are performed at 1 bar. However, the results obtained for an O_2 pressure of 4 bar are same as that at 1 bar.

The Fig. 6.5 shows the calculated isothermal phase diagram sections based on DB1 and DB2 for the Mg rich corner of the Mg-Ca-O system at 700, 600 and 500 $°C$. During the solidification at a given composition the solidification sequence is different in the two data bases used. The calculation based on DB1 shows a solidification sequences for the compositions in the Mg rich corner of the Mg-Ca-O system. This thermodynamic calculation of Mg-Ca-O system shows that CaO and MgO are stable in the melt. In the Mg rich corner of the Mg-Ca-O system the CaO is unstable and only MgO could be found in the liquid. This thermodynamic calculation indicates that at low concentrations of Ca and O, MgO forms in the liquid, so that MgO is more stable than CaO in the Mg rich corner. However, DB1 propose that MgO is more stable than the CaO in the melt. The equilibrium calculation of solidification sequence with DB2 is in agreement with the experimental solidification results from the *in situ* measurements. The thermodynamic calculations based on DB1 illustrate the solidification of the Mg rich end of the Mg-Ca-O system by a non-equilibrium solidification. According to the experimental results from the solidification the peak intensity due to MgO does not change, which indicates that in the solid state MgO is more stable than CaO or cannot react to CaO due to a slow solid state diffusion. The above thermodynamic calculations propose a transformation of CaO to MgO. However, the microstructure investigation and the *in situ* measurements of the solidification show that the solidification ends with a eutectic reaction ($L \longrightarrow$

$Mg + Mg_2Ca + (MgO)$) at much higher temperatures. The thermodynamic calculations based on DB1 illustrate the solidification of the Mg rich end of the Mg-Ca-O system by a non-equilibrium solidification. However, this may result when microstructures with a region with mainly CaO in the samples exists (higher content of Ca and O e.g. in Mg30CaO, Mg50CaO and Mg16Ca+CaO). This indicates that CaO can only dissociated up to a certain amount in molten Mg. The calculations are in agreement with the SEM investigations of the samples Mg30CaO, Mg50CaO and Mg16Ca+CaO with compact CaO agglomerations after the melting and solidification. In the beginning of experimental solidification primary Mg forms and at the end of the solidification eutectic $Mg + Mg_2Ca$ Laves phase forms at 516.5 $°C$. This is similar to the solidification in the binary Mg-Ca system, except for the presence of MgO. As proposed, Mg react with O to MgO, this is in agreement with the thermodynamic calculations. This will increase the Ca content in the melt in relation to Mg, which will lower the temperature for the formation of α-Mg, as the melt has a composition closer to the eutectic composition of the binary Mg-Ca system.

The formation temperatures during the solidification, from thermodynamic calculations based on DB2 (using equilibrium conditions) are shown in comparison with the experimental results for Mg20CaO, Mg6Ca+6CaO and Mg16Ca+6CaO in Tab. 6.7. The compositions for this calculations are taken from the compositions measured with EDXS as plotted in Tab. 6.4 and 6.6. The data calculated for Mg30CaO and Mg50CaO samples are not listed, as experimental temperatures for the formation of various phases are unknown.

The comparison between the phase transformation temperatures from the *in situ* experiment and the thermodynamic calculations based on DB2 for Mg20CaO, Mg6Ca+6CaO and Mg16Ca+6CaO shows good agreement. For the Mg20CaO sample the primary Mg formation were calculated at 591 $°C$, which is 21 $°C$ higher than that detected in the experiment. The eutectic temperature for the Mg20CaO and Mg6Ca+6CaO samples were detect at a lower temperature than that calculated. The lower formation temperatures detected with *in situ* experiment are attributed to non-equilibrium nature of solidification, especially associated with the initial energy barrier for nucleation of primary Mg.

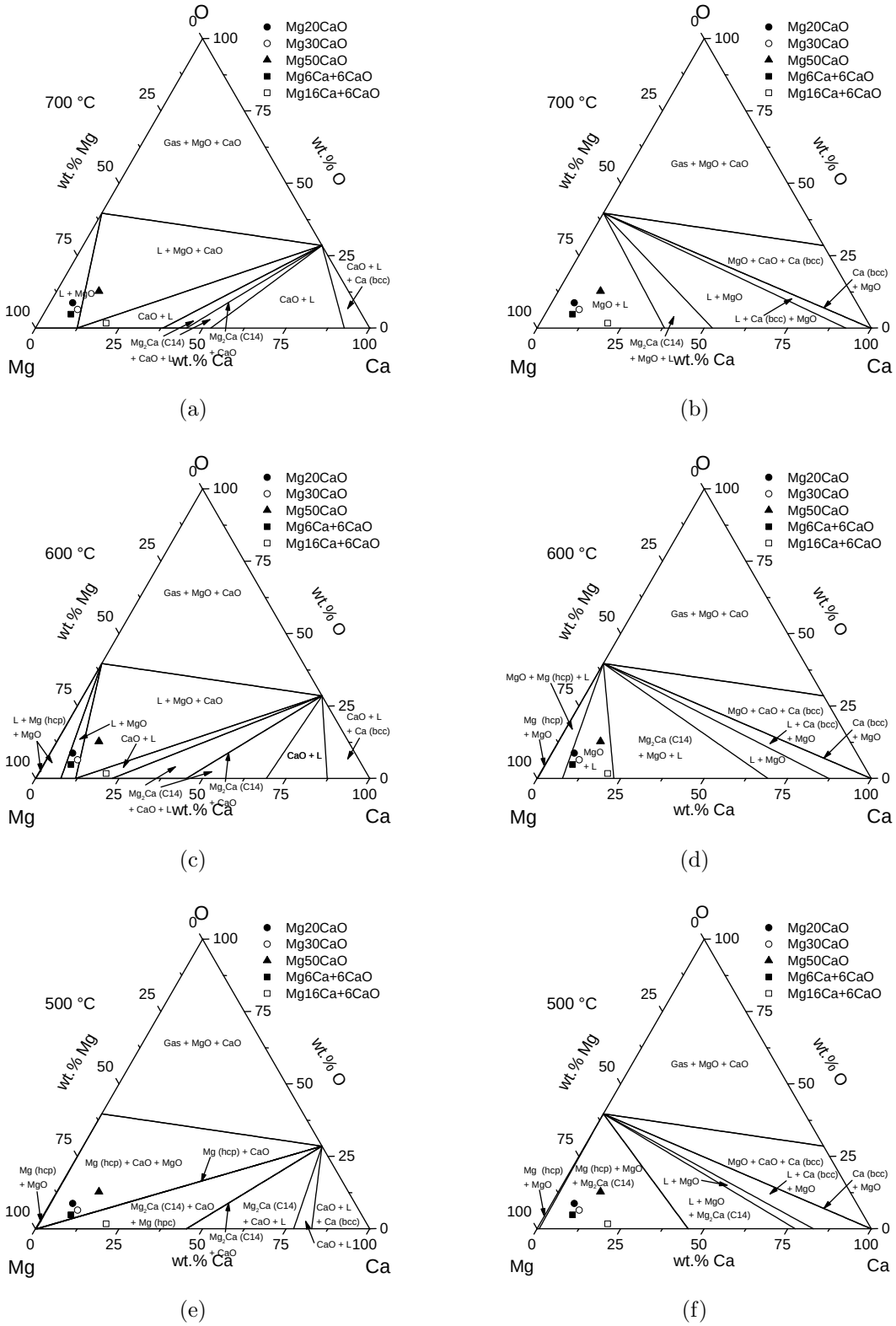

(a) (b) (c) (d) (e) (f)

Fig. 6.5: Calculated isothermal sections of the ternary *Mg-Ca-O* system, based on the thermodynamic data for *CaO* and *MgO* from (a, c, e) Hillert [54] (DB1) and from (b, d, f) Gourishankar et al. [2] (DB2). At (a, b) 700 °*C*, (c, d) 600 °*C* and (e, f) 500 °*C*. The measured composition of the samples indicated. All calculations are at P = 1 *bar*. The database DB1 and DB2 are developed by Institute of Metallurgy - Thermochemistry & microkinetics group in TU Clausthal.

Tab. 6.7: The nominal and measured compositions for the Mg20CaO, Mg6Ca+6CaO and Mg16Ca+6CaO with the phase transformation temperatures from the *in situ* experiment (exp.) and the thermodynamic calculation (calc.) based on DB2. The accuracy of the temperature measurement for the *in situ* experiment is ± 5 $°C$.

Nominal	Mg20CaO		Mg6Ca+6CaO		Mg16Ca+6CaO	
Measured	Mg6.8Ca8.7O		Mg8.2Ca4.8O		Mg15.3Ca6.1O	
	calc.	exp.	calc.	exp.	calc.	exp.
$MgO + L \longrightarrow Mg + MgO + L$	591.0	570.0	585.7	581.0	-	530.0
$Mg + MgO + L \longrightarrow Mg_2Ca + Mg + MgO$	516.5	509.0	516.5	504.0	-	507.0
$MgO + L \longrightarrow Mg_2Ca + MgO + L$	-	-	-	-	541.2	-
$Mg_2Ca + MgO + L \longrightarrow Mg + Mg_2Ca + MgO$	-	-	-	-	516.5	-
	T [$°C$]					

Additional factor that may contribute include the possible thermal gradients in the specimen. Liquidus temperature is detected, within in the accuracy of the measurements at approximately 581 $°C$ for the Mg6Ca+6CaO. The measured liquidus temperature and the eutectic temperature of the Mg20CaO and Mg6Ca+6CaO samples validated the calculations, as there is good agreement between the calculated values and measured values. In case of Mg16Ca+6CaO the calculated solidification (based on DB2) starts with Mg_2Ca and the eutectic formation of $Mg_2Ca + Mg$ occurs at a temperature of 516.5 $°C$. This is because of the composition of Ca is above the eutectic composition of Mg-Ca system, with a Ca content of 16.3 $wt.\%$. A deviation in the solidification sequence is mainly related to composition measured with EDXS, where there is some inaccuracy with the measurement due to light elements, e.g. O. A higher O or Ca content as measured by EDXS is related to a higher Ca content in the liquid, which change the solidification and the primary formation of Mg_2Ca. These results show that the measurement of the composition with EDXS is inaccurate for a sample composition close to the tie line. With a lower content of O or Ca the solidification path becomes similar to the experimental results observed for Mg16Ca+6CaO.

The thermodynamic calculation for the Mg30CaO and Mg50CaO samples show primary Mg formation and eutectic $Mg_2Ca + Mg$ formation. This is in agreement with the microstructural investigations of these samples and with the solidification sequence observed.

The investigation shows that the theory of Kondoh et al. [1] for the CaO dissociation in Mg-Al alloys by the formation of the Laves phase Al_2Ca cannot be applied to an Al free system. They proposed that the formation of the Laves phase is the reason for the dissociation of CaO. The experiments and the calculations show that the formation of Mg_2Ca is not a prerequisite for the dissociation of CaO, but the Laves phase occurs above the solid solution limit of Ca in Mg. The thermodynamic calculations explain the solid state formation of Mg_2Ca in the investigations of Wiese et al. [158]. The conclusion from Kondoh et al. [1] is that the formation of Laves phases did not reduce the energy of the system, but the enthalpy of mixtures affected the actual phase formation as well the dissociation of CaO.

Using the cross section of Mg-Ca-O phase diagram at 0.1 $wt.\%$ O, the role of MgO can be explained. Fig. 6.6(a) illustrates the binary Mg-Ca system (PanMagnesium 8) and cross section of Mg-Ca-O phase diagram at 0.1 $wt.\%$ O, based on the thermodynamic data for CaO and MgO from b) Hillert [54] (DB1) and from c) Gourishankar et al. [2] (DB2). There are some similarities between the cross sections of Mg-Ca-O at 0.1 $wt.\%$ O and the binary Mg-Ca system. As proposed, the MgO reduced the amount of metallic Mg in the melt, which lead to a higher Ca concentration in the liquid. The thermodynamic calculation using DB2, shows that MgO is more stable than CaO up to a Ca content of 93 $wt.\%$ (Fig. 6.6(c)). This tie line moves to lower concentration of approximately 12 $wt.\%$ Ca with the thermodynamic data based on DB1 (Fig. 6.6(b)). These calculations shows that CaO is not stable at high Mg concentrations.

In the case of the DB1 calculations of the Mg rich side of the Mg-Ca-O system all MgO react with the Ca to CaO during the solidification. This react from MgO to CaO during the solidification was not determined in the *in situ* experiment. However, a phase transition from CaO to MgO during the solidification under equilibrium conditions is a possible reaction, but a slow solid state diffusion can resulted in non-equilibrium

condition with a major fraction of MgO. This results in a similar solidification as in the binary Mg-Ca system in a non-equilibrium condition, except for the presence of MgO and CaO. The position of the tie line also indicates a residue of CaO after the melting and solidification process with a high content of Ca, e.g. in the samples Mg30CaO, Mg50CaO and Mg16Ca+CaO.

The calculations based on DB1 and DB2 are both in agreement with the experimental results. The calculations based on DB1 are in a agreement with a non-equilibrium condition during the solidification, as described previously. The calculations based on DB2 are in a agreement with a equilibrium condition during the solidification. However, the experimental results are until now not sufficient to decide which database is more reliable.

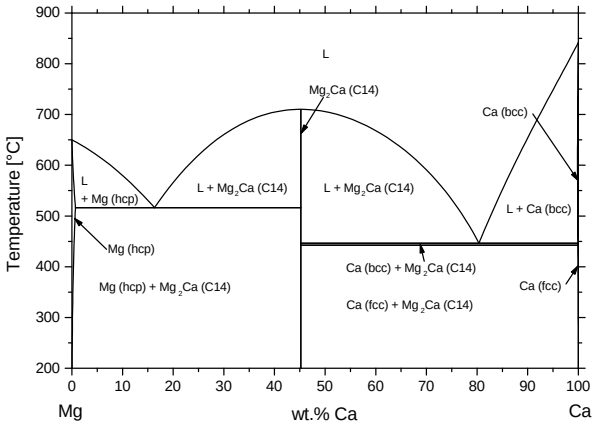

(a)

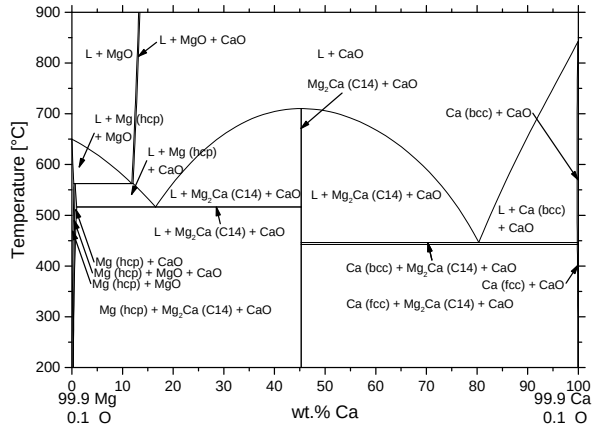

(b)

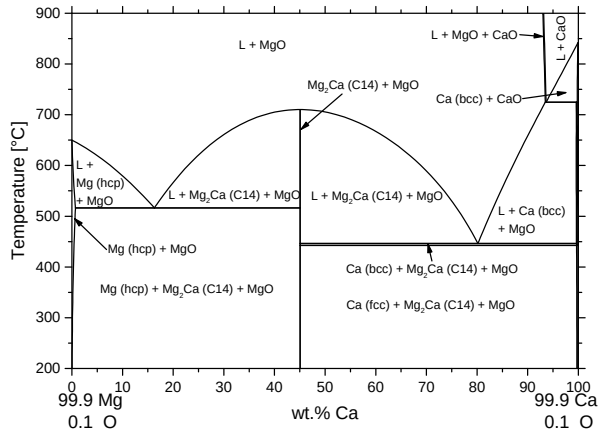

(c)

Fig. 6.6: Calculated a) binary *Mg-Ca* system (PanMagnesium 8) and phase diagram section *Mg-Ca-O* with 0.1 *wt.*% *O*, based on the thermodynamic data for *CaO* and *MgO* from b) DB1 [54] (DB1) and from c) Gourishankar et al. [2] (DB2). The databases DB1 and DB2 were developed by Institute of Metallurgy - Thermochemistry & microkinetics group in TU Clausthal.

6.4.2 The proposed effect on the oxide layer formation of Mg-Ca alloys

The theory on oxide layer formation on alloys at high temperature propose the formation of a mixed oxide [72, 73], in the case of a oxide system as MgO-CaO with a no solid solution of the oxides. This system will form a sequence of MgO and CaO in a layered structure [46, 54, 67–71] in Mg-Ca alloys. The oxide layer structure is not been fully investigated previously.

The thermodynamic calculations based on DB1 and DB2 at 500 $°C$, Fig. 6.5, shows that in the solid-state a layer of MgO and CaO form at high O concentrations. During oxidation of Mg rich Mg-Ca alloys, this is the condition near the surface. As a result the top layer should contain MgO and CaO for the calculation based on DB1 and DB2.

According to the literature [58,65,102] only MgO and CaO are involved in the oxide layer formation. The calculation based on DB1 and DB2 shows the same oxide layer formation. It is now possible to formulate a theory on how CaO improve the oxidation resistance on Mg-Ca alloys.

The theory proposes the formation of a MgO and CaO side by side on Mg-Ca alloys. The PBR of Mg/MgO is 0.81 which is < 1 and Ca/CaO is 0.64, which can not applied to explain the protective effect on Mg. However, if we propose the formation of pure CaO on Mg as well Mg-Ca alloys, it will result in a PBR of Mg/CaO of 1.20. Based on this idea the Eq. 3.7 was modified to Eq. 6.1. This calculation is for PBR ≥ 1, which should protect Mg-Ca alloys in the presence of O from the atmosphere [72, 76]. When the oxide layer consists of a mixture of MgO and CaO (Fig. 6.7) the large volume of CaO will compensate for the shrinkage due to MgO formation. The volume fraction of CaO and MgO required for the PBR to be 1, to a provide protective oxide layer. If the Eq. 6.2 was used the volume fraction of CaO should be approximately 0.49 in the oxide layer for PBR ≈ 1. The calculation for the CaO content in this oxide layer is 47.3 $wt.\%$ CaO which require 33.8 $wt.\%$ (19.5 $at.\%$) Ca and 31.8 $wt.\%$ (30.4 $at.\%$) Mg.

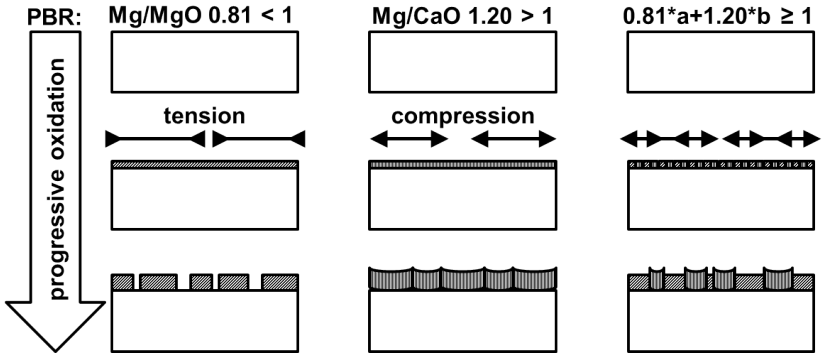

Fig. 6.7: Evolution of the oxide layer for PBR of Mg/MgO 0.81, Mg/CaO 1.20 and the combination of Mg/MgO and $Mg/CaO \geq 1$.

$$PBR_{Mg/CaO} = \frac{V_{CaO}}{V_{Mg}} = \frac{M_{CaO} \cdot \rho_{Mg}}{n_{CaO} \cdot M_{Mg} \cdot \rho_{CaO}} = 1.20 \tag{6.1}$$

$$PBR_{combination} = Mg/MgO * x + Mg/CaO * y = 0.81 * x + 1.2 * y \tag{6.2}$$

This is partly in agreement with the investigation of You et al. [65], who show a combination of Mg/MgO and Mg/CaO for Mg-Ca alloys. The phases and elements detected with XRD and Auger electron spectroscopy (AES) in the oxide layer are only MgO and CaO at 440, 480 and 500 $°C$ for Mg1.5Ca and Mg5Ca alloys [65]. The AES results for the oxidation at 500 $°C$ are illustrated in Fig. 6.8 [65]. In contrast to the oxide layer formation on pure Mg with a constant concentration of Mg and O in Mg-Ca contending alloys a layered structure contending Ca and Mg was detected. The top layer composed of Ca and O followed by a layer with a average content of 39 $wt.\%$ Mg, 26 $wt.\%$ Ca and balance O. The last layer is composed of in average 10 $wt.\%$ Mg, 45 $wt.\%$ Ca and balance O, after which Mg-Ca alloys was detected.

The O diffuse through the MgO and CaO layer according to Wagner [78]. However, the reason for the CaO top layer could be the higher ΔG compared with MgO during the initial stage of the oxidation. The second oxide layer can be explained by impoverishment of Ca in the early stage of the oxidation. If the oxidation speed slows, due to the formation of an oxide layer, Ca has more time to diffuse to the oxide/metal interface. The results of You et al. [65] are not entirely in a agreement to the proposed combination of the PBR

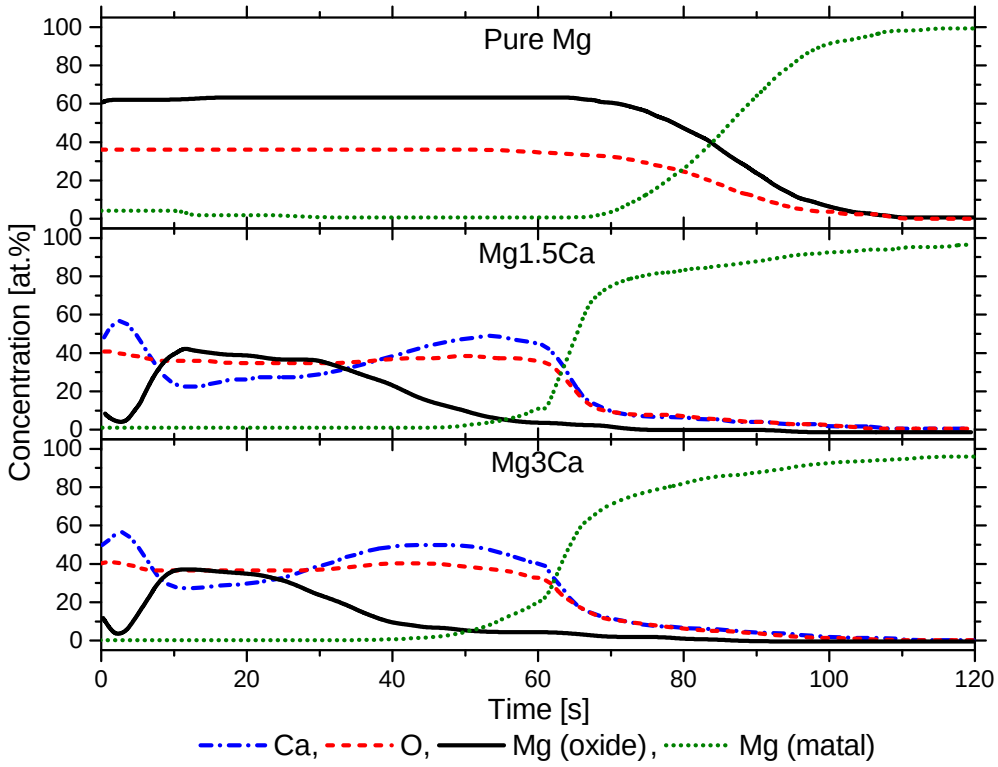

Fig. 6.8: The oxide layer for the oxidation at 500 $°C$, adopted from You et al. [65].

from Mg/MgO and Mg/CaO, but indicate a mixture of the Mg and Ca oxide in the oxide layer. With a PBR 1.20 of Mg/CaO it should form a protective layer followed by a oxide layer with 39 $wt.\%$ Mg, 26 $wt.\%$ Ca and balance O, which resulted in a combined PBR of 1.05. In the oxide layer at the oxide/metal interface with 10 $wt.\%$ Mg, 45 $wt.\%$ Ca has a PBR of 1.06. For all these combinations the PBR between Mg/CaO and Mg/MgO is > 1, which is protective as proposed by Pilling and Bedworth [76]. This PBR can explain the protective effect of Ca on Mg-Ca alloys. However, this theory could not be proved in this work, but should be the focus of the research on the oxidation of solid Mg-Ca alloys.

CHAPTER 7

Conclusions

Mg is able to reduce CaO which is the opposite of the commonly ascribed view, and this reduction occurs already in the solid state. The solidification results from the *in situ* synchrotron radiation diffraction experiments agree with microstructure investigations in the as-solidified samples. The previous investigations show that CaO is reduced by Mg or Mg-Al alloys, but do not explain the exact mechanisms behind this reduction. This thesis show that CaO is not stable compared to MgO for alloys in the in the Mg-rich corner of the Mg-Ca-O system. The common Ellingham diagram cannot be applied to explain the dissociation of CaO in the ternary system because liquid solution phases are not considered in any calculation based on stoichiometric phases only.

The *in situ* synchrotron radiation diffraction experiments on Mg-xCaO and Mg-xCa-yCaO determined the temperature range and the state (whether liquid or solid) in which the dissociation of CaO will occur and which phases form during this process. It was possible to follow the dissociation of the phases and the phase formation during the solidification.

The experimental results from the solidification sequence were used to validated thermodynamic calculations of Prof. R. Schmid-Fetzer and Dr. A. Kozlov (Institute of Metallurgy form Thermochemistry & microkinetics in TU Clausthal). In this calculation number of different literature values for the thermodynamic data of CaO and MgO were used to calculate the ternary phase diagram Mg-Ca-O. The common Ellingham diagrams are not reliable, as shown by the thermodynamic calculations based on different thermodynamic

data for CaO and MgO (Chase 1985 [52], Hillert and Xizhen [54] and Gourishankar et al. [2]) and with experimental results. This work shows the interaction between Mg and Ca and their oxides, when it forms and its role during melting and solidification. The result from the calculations is that the change in standard Gibbs free energy (ΔG) for CaO and MgO of Gourishankar et al. [2] is not a prerequisite for the dissociation of CaO. The MgO form through a reaction between Mg with O and reduce the amount of metallic Mg according to the oxygen content in the melt, which leads to a higher Ca concentration in the liquid. In the end the melt solidifies in a manner similar to the binary Mg-Ca system.

Kondoh et al. [1] theory for the CaO dissociation in Mg-Al alloys by the formation of the Laves phase Al_2Ca can not be applied to Al free systems. This is because they proposed that the formation of the Laves phases is the reason for the dissociation of CaO. The experiments and the calculations show that the formation of Mg_2Ca is not a prerequisite for the dissociation of CaO, but the Laves phase occurs above the maximum solubility of Ca in Mg. However, the enthalpy of mixing play an important role together with the change in standard Gibbs free energy (ΔG) of the phase formation. The thermodynamic calculations are able to explain the solid state formation of Mg_2Ca in the investigations by Wiese et al. [158].

We propose the formation of pure CaO on Mg as well Mg-Ca alloys, it will resulted in a PBR of Mg/CaO of 1.20. If the oxide layer composed of a mixture of MgO and CaO the expansion during the formation of CaO will compensated by the shrinkage due to MgO formation. At a volume fraction of CaO of approximately 0.49 in the oxide layer when the PBR is ≈ 1. This is in agreement with the investigations of You et al. [65], who shows a PBR > 1 at 500 $^{\circ}C$ for Mg1.5Ca and Mg5Ca alloys by calculating the PBR from the measured concentration. The proposed theory for the protective effect of Ca on Mg alloys are compensation of the volume change in the formation of MgO and CaO.

CHAPTER 8

Future work

8.1 Investigation of the oxide layer structure

Ongoing investigations on the oxide layer structure on Mg-Ca alloys should be a focus of Mg research to understand detail in the protective nature of Ca on Mg. The protective nature Ca on Mg melt can lead to the possible substitution of protection gas, that have a high Global Warming Potential (GWP) e.g. SF_6 or harmful by products e.g. SO_2; with Ca or CaO. The understanding of the interactions between Ca and Mg will show the amount of Ca required and the temperature range for effective protection. If the results show mechanism by which the Ca change the oxide layer formation, it is possible to transfer this knowledge to other Mg alloy systems e.g. rare earth (RE) elements, Zn, Sn etc.

This investigation did not indicate that alloying elements can fully substitute the protection gas, however it will improve the knowledge of oxidation of Mg alloys. This can be a useful tool for the development of new Mg alloys for high temperature applications. Understanding the role of Ca in protecting Mg alloys is useful for the design of high temperature applications where oxidation of the component may be a problem, e.g. combustion engines.

8.2 Expansion of the thermodynamic calculations to Mg-X-O system

The expansion of the thermodynamic calculations of Mg-X-O system for commercial alloying elements, can improve the knowledge of the oxidation resistance of Mg-X alloys from thermodynamic knowledge. This research topic can be a useful tool in designing new Mg alloys for high temperatures application. Together with the investigations, on the oxide layer formation on Mg alloys, the thermodynamic calculations have the ability to do provide explanation of the protective nature of the alloying addition.

Bibliography

[1] K. Kondoh, J. Fujit, J. Umeda, H. Imai, K. Enami, M. Ohara, and T. Igarashi. Thermo-dynamic analysis on solid-state reduction of CaO particles dispersed in Mg–Al alloy. *Materials Chemistry and Physics*, 129:631–640, 2011.

[2] K. V. Gourishankar, M. K. Ranjbar, and G. R. St. Pierre. Revision of the enthalpies and gibbs energies of formation of calcium oxide and magnesium oxide. *Journal of Phase Equilibria*, 14(5):601–611, 1993.

[3] H. E. Friedrich and B. L. Mordike. *Magnesium Technology / Metallurgy, Design Data, Applications*. 1. Springer-Verlag, Berlin, Heidelberg, Germany, 2006.

[4] E. F. Emley. *Principles of magnesium technology*. 1. Pergamon Press / Oxford, New York, 1966.

[5] A. Beck. *Magnesium und seine Legierungen*. 2. Springer-Verlag / Berlin, 1939/2001.

[6] R. v. Mises. Mechanik der plastischen Formänderung von Kristallen. *ZAMM - Journal of Applied Mathematics and Mechanics / Zeitschrift für Angewandte Mathematik und Mechanik*, 8(3):161–185, 1928.

[7] M. Ö. Pekgüleryüz, K. U. Kainer, and A. A. Kaya, editors. *Fundamentals of magnesium alloy metallurgy*. Woodhead Publishing Series in Metals and Surface Engineering. Woodhead Publishing, 2013.

[8] C. Kammer. *Magnesium Taschenbuch*. 1. Aluminium-Verlag, 2000.

[9] M. Merkel and K.-H. Thomas. *Taschenbuch der Werkstoffe: mit 143 Tabellen*. 7. Fachbuchverlag Leipzig im Carl Hanser Verlag / München, 2008.

[10] W. Weißbach and M. Dahms. *Werkstoffkunde / Struktur,Eigenschaften, Prüfung*. 16. Viewege / Braunschweig, 2007.

[11] G. Levi, S. Avraham, A. Zilberov, and M. Bamberger. Solidification, solution treatment and age hardening of a Mg 1.6 wt.% Ca 3.2 wt.% Zn alloy. Technical report, Department of Materials Engineering, Technion-Israel Institute of Technology, 2005.

[12] Y. Wan, G. Xiong, H. Luo, F. He, Y. Huang, and X. Zhou. Preparation and characterization of a new biomedical magnesium-calcium alloy. Technical report, School of Materials Science and Engineering, Tianjin University / School of Mechanical and Electrical Engineering, East China Jiaotong University, 2008.

[13] Y. C.Lee, A. K. Dahle, and D. H. St.John. The Role of Solute in Grain Refinement of Magnesium. *Metallurgical and Materials Transactions A*, 31A:2895–2906, 2000.

[14] S.-H. Ha, J.-K. Lee, H.-H. Jo, S.-B Jung, and S. K. Kim. Behavior of CaO and Calcium in Pure Magnesium. *Rare Metals*, 25:150–154, 2006.

[15] J. D. Hanawalt, C. E. Nelson, and J. A. Peloubert. Corrosion studies of magnesium and its alloys. *Transactions of the American Institute of Mining and Metallurgical Engineers, Incorporated*, 147:273–299, 1942.

[16] H. R. B. Rad, M. H. Idris, M. R. A. Kadir, and S. Farahany. Microstructure analysis and corrosion behavior of biodegradable Mg-Ca implant alloys. *Materials and Design*, 33:88–97, 2012.

[17] W. Blum, Y. J. L, X. H. Zeng, B. von Großmann, C. Haberling, and H.-G. Haldenwanger. *Creep Resistance and Creep Kinetics of Mg-alloys*, pages 62–67. Wiley-VCH Verlag GmbH & Co. KGaA, 2005.

[18] R. Ninomiya, T. Ojiro, and K. Kubota. Improved heat resistance of Mg-Al alloys by the Ca addition. *Acta Metallurgica et Materialia*, 43(2):669–674, 1995.

[19] X. N. Gu, W. Zheng, Y. Cheng, and Y. F. Zheng. A study on alkaline heat treated Mg-Ca alloy for the control of the biocorrosion rate. *Acta Biomaterialia*, 5(7):2790–2799, 2009.

[20] X.-N. Gu and Y.-F. Zheng. A review on magnesium alloys as biodegradable materials. *Frontiers of Materials Science in China*, 4(2):111–115, 2010.

[21] P.-R. Cha, H.-S. Han, G.-F. Yang, Y.-C. Kim, K.-H. Hong, S.-C. Lee, J.-Y. Jung, J.-P. Ahn, Y.-Y. Kim, S.-Y. Cho, J. Y. Byun, K.-S. Lee, S.-J. Yang, and H.-K. Seok. Biodegradability engineering of biodegradable Mg alloys: Tailoring the electrochemical properties and microstructure of constituent phases. *Scientific Reports*, 3:1–6, 2013.

[22] S .K. KIM and J. H. SEO. Magnesium-based alloy for high temperature and manufacturing method thereof, 2014. US Patent 8,808,423.

[23] S. K. Kim. *Magnesium Alloys - Design, Processing and Properties / Design and Development of High-Performance Eco-Mg Alloys*. 1. InTech, Rijeka, Croatia, frank czerwinski edition, 2011.

[24] J.-K. Lee and S. K. Kim. Development of Novel Environment-friendly Magnesium Alloys. *Advanced Materials Research*, 47-50:940–943, 2008.

[25] Y. M. Kim, H. S. Kim, B. S. You, and C. D. Yim. Non-flammable magnesium alloy with excellent mechanical properties, and preparation method thereof, 2013. US Patent App. 13/510,989.

[26] Dead Sea Magnesium (DSM) Ltd., 2014.

[27] N. Baar. Über die Legierugen des Molybdäns mit Nickel, Mangans mit Thallium und des Calciums mit Magnesium, Thallium, Blei, Kupfer und Silber. *Zeitschrift für anorganische Chemie*, 70:352–394, 1911.

[28] R. Pàris. Le systeme magnesium-calcium. *Publications scientifiques et techniques du Ministare de l'Air*, 1:39–41, 1937.

[29] M. W. Chase. Heats of Transition of the Elements. *Journal of Phase Equilibria (Bulletin of Alloy Phase Diagrams)*, 4:96–124, 1983.

[30] M. Aljarrah and M. Medraj. Thermodynamic modeling of the Mg-Ca, Mg-Sr, Ca-Sr and Mg-Ca-Sr systems using the modified quasichemical model. *CALPHAD*, 32:240–251, 2008.

[31] J. L. Haughton. Alloys of magnesium. Part 6: The construction of the magnesium-rich alloys of magnesium and calcium. *Jornal of the Institute of Metals*, 61:241–246, 1937.

[32] W. Klemm and F. Dinkelacker. Über das Verhalten des Magnesiums zu Calcium, Strontium und Barium. *Zeitschrift für anorganische Chemie*, 255:2–12, 1947.

[33] A. A. Nayeb-Hashemi and J. B. Clark. The Ca-Mg (Calcium-Magnesium) system. *Journal of Phase Equilibria*, 8(1):58–65, 1987.

[34] R. Agarwal, J. J. Lee, H. L. Lukas, and F. Sommer. Calorimetric measurements and thermodynamic optimization of the Ca-Mg system. *Zeitschrift für Metallkunde/Materials Research and Advanced Techniques*, 86:103–108, 1995.

[35] H. Vosskühler. Der Aufbau der magnesiumreichen Magnesium-Kalzium-Legierungen / The phase diagram of magnesium-rich Mg-Ca alloys. *Zeitschrift fur Metallkunde*, 29:236–237, 1937.

[36] H. Nowotny, E. Wormnes, and A. Mohrnheim. Untersuchungen in den Systemen Aluminium-Kalzium, Magnesium-Kalzium und Magnesium-Zirkon / Investigation on the Al-Ca, Mg-Ca, and Mg-Zr systems. *Zeitschrift fur Metallkunde*, 32:39–42, 1940.

[37] R. H. Taylor, S. Curtarolo, and G. L. W. Hart. Guiding the experimental discovery of magnesium alloys. *PHYSICAL REVIEW B*, 84:1–17, 2011.

[38] H. Witte. Die Kristallstruktur des $CaMg_2$. *Naturwissenschaften*, 25:795, 1937.

[39] C. O. Brubaker and Z.-K. Liu. A computational thermodynamic model of the Ca-Mg-Zn system. *Journal of Alloys and Compounds*, 370(1–2):114 – 122, 2004.

[40] Y. Zhong, K. Ozturk, J. O. Sofo, and Z.-K. Liu. Contribution of first-principles energetics to the Ca-Mg thermodynamic modeling. *Journal of Alloys and Compounds*, 420:98–106, 2006.

[41] Y. Zhong, J. O. Sofo, A. A. Luoc, and Z.-K. Liu. Thermodynamics modeling of the Mg-Sr and Ca-Mg-Sr systems. *Journal of Alloys and Compounds*, 421:172–178, 2006.

[42] H. Zhang, Y. Wang, S. Shang, L.-Q. Chen, and Z.-K. Liu. Thermodynamic modeling of Mg-Ca-Ce system by combining first-principles and CALPHAD method. *Journal of Alloys and Compounds*, 463:294–301, 2008.

[43] S. Wasiur-Rahman and M. MedrajCorresponding. Critical assessment and thermodynamic modeling of the binary Mg-Zn, Ca-Zn and ternary Mg-Ca-Zn systems. *Intermetallics*, 17:847–864, 2009.

[44] W. Bulian and E. Fahrenhorst. Über die Löslichkeit von Kalzium in Magnesium / Solubility of calcium in magnesium. *Metallforschung*, 1:70, 1946.

[45] E. C. Burke. Solid solubility of calcium in magnesium. *J. Met. Trans. AIME*, 203:285–286, 1955.

[46] T. Bachmann et al. Römpp online. Georg Thieme Verlag, 2014.

[47] P. E. Halstead and A. E. Moore. The thermal dissociation of calcium hydroxide. *J. Chem. Soc.*, pages 3873–3875, 1957.

[48] C.l Brosset and N.-G. Vannerberg. Formation of Calcium Superoxide. *Nature*, 177:238–238, 1956.

[49] E. V. Ballou, P. C. Wood, L. A. Spitze, and T. Wydeven. The Preparation of Calcium Superoxide from Calcium Peroxide Diperoxyhydrate. *Industrial & Engineering Chemistry Product Research and Development*, 16(2):180–186, 1977.

[50] O. Caspar and W. Dötsch. Erdalkalimetallperoxid-Produkt, 1996.

[51] I. Barin, O. Knacke, and O. Kubaschewski. *Thermochemical properties of inorganic substances*, volume 1. Springer-Verlag Berlin Heidelberg, 1977.

[52] M. W. Chase, C. A. Davies, J. R. Downey, D. J. Frurip, R. A. McDonald, and A. N. Syverud. *JANAF Thermochemical Tables Third Edition*, volume 14. Journal of Physical and Chemical Reference Data, 1985.

[53] M. Binnewies and E. Milke. *Thermochemical Data of Elements and Compounds, Second, Revised and Extended Edition*, volume 2. Wiley-VCH Verlag GmbH, 2002.

[54] M. Hillert and W. Xizhen. Thermodynamic calculation of the cao-mgo system. *Calphad*, 13(3):267–271, 1989.

[55] S.-L.Cheng, G.-C. Yang, J.-F. Fan, Y.-J. Li, and Y.-H. Zhou. Effect of Ca and Y additions on oxidation behavior of AZ91 alloy at elevated temperatures. *Trans. Nonferrous Met. Soc. China*, 19:299–304, 2008.

[56] D.-H. Choi, B.-W. Ahn, S.-K. Kim, Y.-M. Yeon, Y.-J. Kim, S.-K. Park, and S.-B. Jung. Microstructure Evaluation of Friction Stir Welded AZ91 with CaO Mg Alloy. *Materials Transactions*, 52:802–805, 2011.

[57] D.-H. Choi, S.-K. Kim, and S.-B. Jung. The microstructures and mechanical properties of friction stir welded AZ31 with CaO Mg alloys. *Journal of Alloys and Compounds*, 554:162–168, 2013.

[58] S.-H. Ha, J.-K. Lee, and S. K. Kim. Effect of CaO on Oxidation Resistance and Microstructure of Pure Mg. *Materials Transactions*, 49:1081–1083, 2008.

[59] Y.-B. Huang, I.-S. Chung, B.-S. You, W.-W. Park, and B.-H. Choi. Effect of Be Addition on the Oxidation Behavior of Mg-Ca Alloys at Elevated Temperature. *METALS AND MATERIALS International*, 10:7–10, 2004.

[60] D.-I. Jang, Y.-O. Yoon, S.-B. Jung, and S. K. Kim. Effect of CaO on AZ31 Mg Strip Castings. *Materials Transactions*, 49:976–979, 2008.

[61] S. K. Kim, J.-K. Lee, Y.-O. Yoon, and H.-H. Jo. Development of AZ31 Mg alloy wrought process route without protective gas. *Journal of Materials Processing Technology*, 187-188:757–760, 2007.

[62] J.-K. Lee and S. K. Kim. Effect of CaO composition on oxidation and burning behaviors of AM50 Mg alloy. *Trans. Nonferrous Met. Soc. China*, 21:23–27, 2011.

[63] J.-K. Lee and S. K. Kim. Effect of CaO Addition on the Ignition Resistance of Mg-Al Alloys. *Trans. Nonferrous Met. Soc. China*, 52:1483–1488, 2011.

[64] N. D. Nam, M. Z. Bian, M. Forsyth, M. Seter, M. Tan, and K. S. Shin. Effect of calcium oxide on the corrosion behaviour of AZ91 magnesium alloy. *Corrosion Science*, 64:263–271, 2012.

[65] B.-S. You, W.-W. Park, and I.-S. Chung. The effect of Calcium additions on the oxidation behavior in Magnesium Alloys. *Scripta mater.*, 42:1089–1094, 2000.

[66] O. Knacke, O. Kubaschewski, and K. Hesselmann. *Thermochemical Properties of Inorganic Substances*, volume 2. Springer-Verlag, Berlin, 1991.

[67] S. Serena, M. A. Sainz, S. de Aza, and A. Caballero. Thermodynamic assessment of the system ZrO2–CaO–MgO using new experimental results: Calculation of the isoplethal section MgO·CaO–ZrO2. *Journal of the European Ceramic Society*, 25(5):681–693, 2005.

[68] R. C. Doman, J. B Barr, R. N. McNally, and A. M. Alper. Phase Equilibria in the System CaO—MgO. *Journal of the American Ceramic Society*, 46(7):313–316, 1963.

[69] G. A. Rankin and H. E. Merwin. THE TERNARY SYSTEM CaO-Al2O3-MgO. *Journal of Physical Chemistry B*, 38(3):568–588, 2001.

[70] O. Ruff, F. Ebert, and U. Krawczynski. Beiträge zur Keramik hochfeuerfester Stoffe. VII. Die binären Systeme: MgO-CaO, MgO-BeO, CaO-BeO. *Zeitschrift für anorganische und allgemeine Chemie*, 213(4):333–335, 1933.

[71] M. Y. Lavrentiev, N. L. Allan, G. D. Barrera, and J. A. Purton. Ab Initio Calculation of Phase Diagrams of Oxides. *Journal of Physical Chemistry B*, 105(17):3594–3599, 2001.

[72] R. Bürgel, H. J. Maier, and T. Niendorf. *Handbuch Hochtemperatur-Werkstofftechnik - Grundlagen, Werkstoffbeanspruchungen, Hochtemperaturlegierungen und -beschichtungen*. 4. Vieweg+Teubner Verlag, 2011.

[73] G. C. Wood. High-temperature oxidation of alloys. *Oxidation of Metals*, 2:11–57, 1970.

[74] R. A. Cottis, M. J. Graham, R. Lindsay, S. B. Lyon, J. A. Richardson, J. D. Scantlebury, and F. H. Stott, editors. *Volume 1: Shriers Corrosion: Basic Concepts, High Temperature Corrosion*, volume 4 of *ASM handbook 3*. ELSEVIER, 2010.

[75] G. Gottstein. *Physikalische Grundlagen der Materialkunde*. 3. Springer-Verlag Berlin Heidelberg, 2007.

[76] N. B. Pilling and R. E. Bedworth. The oxidation of metals at high temperatures. *J. Inst. Met*, 29:529–591, 1923.

[77] P. Villars and K. Cenzual. *Pearson's Crystal Data - Crystal Structure Database for Inorganic Compounds (on CD-ROM), Release 2013/14*. ASM Internationa, 2013.

[78] C. Wagner. Theoretical Analysis of the Diffusion Processes Determining the Oxidation Rate of Alloys. *The Electrochemical Society*, 99:369–380, 1952.

[79] C. Xu and W. Gao. Pilling-Bedworth ratio for oxidation of alloys. *Material Research Innovations*, 3(4):231–235, 2000.

[80] R. A. Rapp. The high temperature oxidation of metals forming cation-diffusing scales. *Metallurgical Transactions A*, 15:765–782, 1984.

[81] I. Anžel. High temperature oxidation of metals and alloys. *Metalurgija*, 13:325–336, 2007.

[82] V. Fournier, P. Marcus, and I. Olefjord. Oxidation of magnesium. *Surface and Interface Analysis*, 34:494–497, 2002.

[83] F. Czerwinski. Oxidation Characteristics of Magnesium Alloys. *JOM*, 64(12):1477–1483, 2012.

[84] P. Boris. A STUDY OF THE FLAMMABILITY OF MAGNESIUM. *FEDERAL AVIATION AGENCY*, pages 1–24, 1964.

[85] A. Kielbus, T. Rzychon, and R. Przeliorz. Oxidation Behaviour of WE54 and Elektron 21 Magnesium Alloys. *Defect and Diffusion Forum*, 312-315:483–488, 2006.

[86] Y. M. Kim, C. D. Yim, H. S. Kim, and B. S. You. Key factor influencing the ignition resistance of magnesium alloys at elevated temperatures. *Scripta Materialia*, 65(11):958 – 961, 2011.

[87] F. Czerwinski. Overcoming Barriers of Magnesium Ignition and Flammability. *Advanced Materials and Processes*, 172:28–31, 2014.

[88] B. H. Choi, I. M. Park, B. S. You, and W. W. Park. Effect of Ca and Be Additions on High Temperature Oxidation Behavior of AZ91 Alloys. *Materials Science Forum*, 419-422:639–644, 2003.

[89] W. Spiegelberg, S. Ali, and S. Dunstone. The Effects of Beryllium Addition of Magnesium and Magnesium Containing Alloys. In Barry L.Mordike and F. Hehmann, editors, *Magnesium Alloys and Their Applications*, pages 259–273, Garmisch-Partenkirchen, Germany, 1992. DGM Informationsgesellschaft Verlag.

[90] X. Zeng, Q. Wang, Y. Lü, W. Ding, Y. Zhu, C. Zhai, C. Lu, and X. Xu. Behavior of surface oxidation on molten Mg–9Al–0.5Zn–0.3Be alloy. *Materials Science and Engineering A*, 301(2):154 – 161, 2001.

[91] Z. Xiaoqin, W. Qudong, L. Yizhen, Z. Yanping, D. Wenjiang, and Z. Yunhu. Influence of beryllium and rare earth additions on ignition-proof magnesium alloys. *Journal of Materials Processing Technology*, 112(1):17–23, 2001.

[92] G. Schindelbacher, H. Rockenschaub, A. Sigmund, and P. Wohlmuth. Effektivität und Schutzwirkung von verschiedenen Gasgemischen bei Magnesiumschmelzen / Effectivity and Protection of different Protecting Gas Mixtures on Magnesium Melts. *2. Ranshofener Leichtmetalltagen*, pages 62–65, 2002.

[93] B.-H. Choi, B.-S. You, W.-W. Park, Y.-B. Huang, and I.-M. Park. Effect of Ca addition on the oxidation resistance of AZ91 magnesium alloys at elevated temperatures. *Metals and Materials International*, 9(4):395–398, 2003.

[94] D. B. Lee. High temperature oxidation of AZ31 + 0.3 wt.%Ca and AZ31 + 0.3 wt.%CaO magnesium alloys. *Corrosion Science*, 70:243 – 251, 2013.

[95] A. R. Mirak, C. J. Davidson, and J. A. Taylor. Characterisation of fresh surface films formed on molten Mg-Nd alloy protected by different atmospheres. *Applied Surface Science*, 301:91–98, 2014.

[96] X. M. Wang, X. Q. Zeng, G. S. Wu, S. S. Yao, and L. B. Li. Surface oxidation behavior of MgNd alloys. *Applied Surface Science*, 253(22):9017–9023, 2007.

[97] W. Xuemin, W. Weidong, T. Yongjian, Z. Xiaoqin, and Y. Shoushan. Early high temperature oxidation behaviors of Mg-10Gd-3Y alloys. *Journal of Alloys and Compounds*, 474(1–2):499–504, 2009.

[98] J. F. Fan, G. C. Yang, S. L. Chen, H. Xie, M. Wang, and Y. H. Zhou. Effect of rare earths (Y, Ce) additions on the ignition points of magnesium alloys. *Journal of Materials Science*, 39(20):6375–6377, 2004.

[99] N. V. Ravi Kumar, J. J. Blandin, M. Suéry, and E. Grosjean. Effect of alloying elements on the ignition resistance of magnesium alloys. *Scripta Materialia*, 49(3):225–230, 2003.

[100] X. M. Wang, X. Q. Zeng, Y. Zhou, G. S. Wu, S. S. Yao, and Y. J. Lai. Early oxidation behaviors of Mg-Y alloys at high temperatures. *Journal of Alloys and Compounds*, 460(1–2):368–374, 2008.

[101] R. A. U. Huddle, J. Laing, A. C. Jessup, and E. F. Emley. Improvements in or relating to alloys of magnesium, 1953.

[102] M. Sakamoto, S. Akityama, and K. Ogi. Suppression of ignition and burning of molten Mg alloys by Ca bearing stable oxide film. *Journal of Materials Science Letters*, 16(12):1048–1050, 1997.

[103] J. F. Fan, S.L. Cheng, H. Xie, W. X. Hao, M. Wang, G. C. Yang, and Y. H. Zhou. Surface oxidation behavior of Mg-Y-Ce alloys at high temperature. *Metallurgical and Materials Transactions A*, 36(1):235–239, 2005.

[104] F. Czerwinski. Surface Reactivity of Magnesium Alloys in Solid and Liquid States. *Materials Science Forum*, 765:698–702, 2013.

[105] E. A. Gulbransen. The Oxidation and Evaporation of Magnesium at Temperatures from 400 to 500°C. *The Electrochemical Society*, 87:589–599, 1945.

[106] S. P. Cashion. *The Use of Sulphur Hexafluoride (SF6) for Protecting Molten Magnesium*. PhD thesis, University of Queensland, Department of Mining, Minerals and Materials Engineering, Australia, 1998.

[107] H. J. Mülller. *Handbuch der Schmelz- und Legierungspraxis für Leichtmetalle*. 3. F.A. Verlag Schiele u. Schöne / Berlin, 1977.

[108] A. W. Brace and F. A. Allen. *Magnesium casting technology*. Reinhold Publishing Corporation New York / London: Chapman and Hall, 1957.

[109] F.-W. Bach. Integrierter Umweltschutz in der Gießereiindustrie; Umwelt- und werkstoffgerechte Magnesiumschmelzehandhabung. Technical report, Institut für Werkstoffkunde, Universität Hannover, 2005.

[110] J. E. Hillis. The International Program to Identify Alternatives to SF_6 for Magnesium Melt Protection. *The International Magnesium Association*, pages 1–11, 2002.

[111] S. Bartos, J. Marks, R. Kantamaneni, and C. Laush. Measured SF_6 Emissions From Magnesium Die Casting Operations. In Howard I. Kaplan, editor, *Magnesium Technology 2003*, pages 23–27. TMS (The Minerals, Metals and Materials Society), 2003.

[112] K. Aarstad, G. Tranell, G. Pettersen, and T. A. Engh. VARIOUS TECHNIQUES TO STUDY THE SURFACE OF MAGNESIUM PROTECTED BY SF_6. In Howard I. Kaplan, editor, *Magnesium Technology 2003*, pages 5–10. TMS (The Minerals, Metals and Materials Society), 2003.

[113] S. P. Cashion, N. J. Ricketts, and P. C. Hayes. The mechanism of protection of molten magnesium by cover gas mixtures containing sulphur hexafluoride. *Light Metals*, 2:43–47, 2002.

[114] W. Ha and Y.-J. Kim. Effects of cover gases on melt protection of Mg alloys. *Alloys and Compounds*, 422:208–213, 2006.

[115] S. Cashion and N. Ricketts. The use of SO_2 as a cover gas for molten magnesium. In Howard I. Kaplan, editor, *Magnesium Technology 2003*, pages 77–81. TMS (The Minerals, Metals and Materials Society), 2000.

[116] M. M. Avedesian, editor. *ASM specialty handbook / Magnesium and magnesium alloys*. 1. ASM Internationl, 1999.

[117] G. Tranell, M. Syvertsen, K. Bech, and B. Øye. Alternnatives to SF_6/SO_2 from magnesium melt protection - Final report of the IMA-SINTEF collaboration projekct. Technical report, SINTEF Materials Technology, N-7465 Trondheim, Norway, 2004.

[118] European Union. REGULATION (EU) No 517/2014 OF THE EUROPEAN PARLIAMENT AND OF THE COUNCIL / on fluorinated greenhouse gases and repealing Regulation (EC) No 842/2006. *Official Journal of the European Union*, 2014.

[119] H. W. Dörsam. Magnesium Melting/Casting and Remelting in Foundries. In K. U. Kainer, editor, *Magnesium Technology 2000*, pages 99–105. TMS (The Minerals, Metals and Materials Society), 2000.

[120] N. Ricketts and S. Cashion. The Use of SO_2 as a Cover Gas for Molten Magnesium and the Sulphur Dome Effect. In *7. Magnesium Abnehmer Seminar*, Aalen, Germany, 1999. IMA (International Magneium Association).

[121] X.-F.i Wang and S.-M. Xiong. Protection behavior of SO_2-containing cover gases to molten magnesium alloy. *Transactions of Nonferrous Metals Society of China*, 21:807–813, 2011.

[122] M. Holtzet and A. Bobrowski. Magnesium melt protection by covering gas. *archives of Foundry Engineering*, 8:131–136, 2008.

[123] L. Weizhong, G. Qiu, C. Fu, L. Honghui, and Z. Zhenhua. Protective behavior of an SO_2/CO_2 gas mixture for molten AZ91D alloy. *CHINA FOUNDRY*, 9:226–230, 2012.

[124] X. Wang and S. Xiong. Characterization of the Protective Surface Films Formed on Molten AZ91D Magnesium Alloy in SO_2/Air Atmospheres in a Sealed Furnace. *Journal of Materials Science and Technology*, 30:353–358, 2014.

[125] W. Schwarz and A. Leisewitz. Emissionen und Minderungspotential von HFKW, FKW und SF_6 in Deutschland. Technical report, Öko-Recherche Büro für Umweltforschung und -beratung GmbH Frankfurt/Main, Umweltforschungsplan des Bundesministers für Umwelt, Naturschutz und Reaktorsicherheit Forschungsbericht 298 41 256, 1999.

[126] S. P. Cashion, N. J. Ricketts, and P. C. Hayes. Characterisation of protective surface films formed on molten magnesium protected by air/SF_6 atmospheres. *Light Metals*, 2:37–42, 2002.

[127] B. Palmer. SF_6 Emissions from Magnesium. *Background Paper of: IPCC Good Practice Guidance and Uncertainty Management in National Greenhouse Gas Inventories SF_6 Emissions*, pages 217–226, 2000.

[128] G. Pettersen, E. Øvrelid, G. Tranell, J. Fenstad, and H. Gjestland. Characterisation of the surface films formed on molten magnesium in different protective atmospheres. *Materials Science and Engineering A*, 332:285–294, 2002.

[129] S.-M. Xiong and X.-L. Liu. Microstructure, Composition, and Depth Analysis of Surface Films Formed on Molten AZ91D Alloy under Protection of SF_6 Mixtures. *Metallurgical and Materials Transactions A*, 38A:428–434, 2007.

[130] X.-F. Wang and S.-M. Xiong. Protection behavior of fluorine-containing cover gases on molten magnesium alloys. *Transactions of Nonferrous Metals Society of China*, 20:1228–1234, 2010.

[131] H. Putz, J. C. Schön, and M. Janse. Investigation of the energy landscape of Mg_2OF_2. *Computational Materials Science*, 11:309–322, 1998.

[132] W. Hinz and P.-O. Knuth. Investigation of the energy landscape of MgO-MgF_2-SiO_2. *The American Mineralogist*, 45:1198–1210, 1960.

[133] G. You, S. Long, and R. Li. Effective Protection of Magnesium Melt Surface from Oxidation Using HFC125-Containing Shielding Gas. *Materials Science Forum*, 546-549:119–122, 2007.

[134] G. You, S. Dou, X. Zhang, J. Qi, X. Zeng, and S. Long. Corrosivity of HFC125 as Shielding Gas for Magnesium Melt under High Temperature. *Materials Transactions*, 52:1108–1110, 2011.

[135] B. Metz, O.R. Davidson, P. R. Bosch, R. Dave, and L. A. Meyer. *Contribution of Working Group III to the Fourth Assessment Report of the Intergovernmental Panel on Climate Change*. Cambridge University Press, 2007.

[136] P. Christoph and A. Jurmann. Verfahren zum Schützen der Oberfläche einer Magnesiumschmelze / Method for protecting the surface of a magnesium melt by means of carbon dioxide, 2002. DE10038543A1 14.02.20023.

[137] A. Karger, F.-W. Bach, and C. Pelz. Protective System for Magnesium Melt. *Materials Science Forum*, 488-489:85–88, 2005.

[138] W. Reimers, A. R. Pyzalla, A. Schreyer, and H. Clemens. *Neutrons and Synchrotron Radiation in Engeineering Materials Science, From Fundamentals to Material and Component Characterization*. 1. Wiley VCH Verglag Weinheim, 2008.

[139] W. Kleber, H.-J. Bautsch, and J. Bohm. *Einföhrung in die Kristallographie*. 18. Verlag Technik Berlin, 1998.

[140] W. C. Röntgen. Eine neue Art von Strahlen. *WÜRZBURG. VERLAG UND DRUCK DER STAHEL'SCHEN K. B. HOF- UND UNIVERSITÄTS-BUCH- UND KUNSTHANDLUNG*, 1896.

[141] H. Kuchling. *Taschenbuch der PHYSIK*. 19. Fachbuchverlag Leipzig im Hansser Verlag, 2007.

[142] H. Boersch, C. Radeloff, and G. Sauerbrey. Über die an Metallen durch Elektronen ausgelöste sichtbare und ultraviolette Strahlung. *Zeitschrift für Physik*, 165(4):464–484, 1961.

[143] H. Mosely. Atomic Models and X-Ray Spectra. *Nature*, 92:554–554, 1914.

[144] J. Als-Nielsen and D. McMorrow. *Elements of Modern X-ray Physics*. 2. John Wiley & Sons, 2011.

[145] Deutsche Elektronen-Synchrotron DESY. Desy, 2014.

[146] P. Staron, T. Fischer, T. Lippmann, A. Stark, S. Daneshpour, D. Schnubel, E. Uhlmann, R. Gerstenberger, B. Camin, W. Reimers, E. Eidenberger, H. Clemens, N. Huber, and A. Schreyer. In Situ Experiments with Synchrotron High-Energy X-Raysand Neutrons. *Advanced Engineering Materials*, 13:658–663, 2011.

[147] Y. Miao, K. Mo, Z. Zhou, X. Liu, K.-C. Lan, G.Zhang, M. K. Miller, K. A. Powers, J. Almer, and J. F. Stubbins. In situ synchrotron tensile investigations on the phase responses within an oxide dispersion-strengthened (ODS) 304 steel. *Materials Science and Engineering: A*, 625:146–152, 2015.

[148] C. H. J. Davies, S. B. Yi, J. Bohlen, K. U. Kainer, and H. G. Brokmeier. Synchrotron Radiation Investigation of Twinning in Extruded Magnesium Alloy AZ31. *Materials Science Forum*, 495-497:1633–1638, 2005.

[149] S. S. Babu, J. W. Elmer, J. M. Vitek, and S. A. David. Time-resolved X-ray diffraction investigation of primary weld solidification in Fe-C-Al-Mn steel welds. *Acta Materialia*, 50(19):4763–4781, 2002.

[150] D. Tolnai, C. L.Mendis, A.Stark, G. Szakács, B.Wiese, K. U. Kainer, and N. Hort. In situ synchrotron diffraction of the solidification of Mg4Y3Nd. *Materials Letters*, 102-103:62–64, 2013.

[151] D. Tolnai, C. L. Mendis, A. Stark, G. Szakács, B. Wiese, K. U. Kainer, and N. Hort. *In Situ Synchrotron Diffraction of the Solidification of Mg-RE Alloys*, pages 253–257. John Wiley & Sons, Inc., 2013.

[152] G. Szakács, B. Wiese, C. L. Mendis, D. Tolna, A. Stark, N. Schel, M. Nair, K. U. Kainer, and N. Hort. *In Situ Synchrotron Radiation Diffraction during Solidification of Mg4Y and Mg4YxGd Alloys (x = 1,4 wt.%)*, pages 213–218. John Wiley & Sons, Inc., 2014.

[153] N. Iqbal, N. H. van Dijk, S. E. Offerman, M. P. Moret, L. Katgerman, and G. J. Kearley. Real-time observation of grain nucleation and growth during solidification of aluminium alloys. *Acta Materialia*, 53(10):2875–2880, 2005.

[154] O. Shuleshova, D. Holland-Moritz, W. Löser, G. Reinhart, G. N. Iles, and B. Büchner. Metastable formation of decagonal quasicrystals during solidification of undercooled Al-Ni melts: In situ observations by synchrotron radiation. *EPL (Europhysics Letters)*, 86(3):36002, 2009.

[155] A. Bénéteau, P. Weisbecker, G. Geandier, E. Aeby-Gautier, and B. Appolaire. Austenitization and precipitate dissolution in high nitrogen steels: an in situ high temperature X-ray synchrotron diffraction analysis using the Rietveld method. *Materials Science and Engineering A*, 393(1–2):63–70, 2005.

[156] T. Volkmann, J. Strohmenger, J. Gao, and D. M. Herlach. Observation of a metastable phase during solidification of undercooled Nd-Fe-B alloy melts by in situ diffraction experiments using synchrotron radiation. *Applied Physics Letters*, 85(12):2232–2234, 2004.

[157] K. Hajlaoui, T. Benameur, G. Vaughan, and A. R. Yavari. Thermal expansion and indentation-induced free volume in Zr-based metallic glasses measured by real-time diffraction using synchrotron radiation. *Scripta Materialia*, 51(9):843–848, 2004.

[158] B. Wiese, C. L. Mendis, D. Tolnai, A. Stark, N. Schell, H. P. Reichel, R. Brückner, K. U. Kainer, and N. Hort. CaO dissolution during melting and solidification of a Mg-10 wt.% CaO alloy detected with in situ synchrotron radiation diffraction. *Journal of Alloys and Compounds*, 618(0):64–66, 2015.

[159] B. Wiese, C. L. Mendis, D. Tolnai, G. Szakács, A. Stark, N. Schell, H. P. Reichel, R. Brückner, K. U. Kainer, and N.Hort. *In Situ Synchrotron Radiation Diffraction during Melting and Solidification of Mg-Al Alloys Containing CaO*, pages 191–195. John Wiley & Sons, Inc., 2014.

[160] K. Balewski, W. Brefeld, W. Decking, Y. Li, G. K. Sahoo, and R. Wanzenberg. PETRA III: A New High Brilliance Synchrotron Radiation Source At DESY. *Proceedings of EPAC 2004, Lucerne, Switzerland*, pages 2302–2304, 2004.

[161] PerkinElmer LAS (Germany) GmbH, 2014.

APPENDIX A
List of Figures

List of Figures

APPENDIX B
List of Tables

List of Tables

APPENDIX C
List of Abbreviations

ASTM	American Society for Testing and Materials
AES	Auger Electron Spectroscopy
DESY	Deutsches Elektronen-Synchotron
DSC	Differential Scanning Calorimetry
DTA	Differential Thermal Analysis
ECO-Mg	Environmently COnscious magnesium
EDXS	Energy-dispersive X-ray spectroscopy
GWP	Global Warming Potential
HEMS	High Energy Materials Science
ICP-OES	Inductively coupled plasma optical emission spectroscopy
LP	Line profiles
PBR	Pilling-Bedworth ratio
PETRA III	Positron-Elektron-Tandem-Ring-Anlage 3
SEM	Scanning electron microscopy
T	Temperature
TLV	Threshold Limit Value
XRD	X-ray diffraction
2D	Two-dimensional

APPENDIX D
List of Symbols

B	Brilliance of radiation
c	Speed of light in vacuum $299792458\frac{m}{s}$
c_D	Concentration of element D
D	Diffusion coefficient
d	Interplanar distance
E	Modulus of elasticity
E_r	Energy radiation
f	Frequency
h	Planck constant $6.62606957 \cdot 10^{-34} Js$
J	Diffusion flux
k_+	Oxidation constant + function (l linear, p parabolic or kl catastrophic linear)
M_+	Molecular mass, + metal or oxide
n	Order of interference
n_m	Number of metal atoms per one molecule of the oxide
r	Reaction speed
R	Universal gas constant ($8.314\ \frac{J}{K \cdot mol}$)
r_0	Proportional constant of the reaction speed
V_+	Molecular volume, + metal or oxide
x	Distance
ΔG	Change in Gibbs free energy
ΔG^a	Change in free activation energy
$\Delta G^a_{(mol)}$	Change in Gibbs free energy per mol
λ	Wavelength
μ	Chemical potential
ρ_+	Density, + metal or oxide
θ	Angle of diffraction

APPENDIX E

Scripts to integrate the *in situ* 2D pattern by FIT2D V12.077

BEGINNING OF GUI MACRO FILE:
EXIT
POWDER DIFFRACTION (2-D)
INPUT
#IN
O.K.
O.K.
MASK
THRESHOLD MASK
YES
1
EXIT
INTEGRATE
X-PIXEL SIZE
200
Y-PIXEL SIZE
200
DISTANCE
1162.717
WAVELENGTH
0.124
X-BEAM CENTRE
1023.471
Y-BEAM CENTRE
1035.056
O.K.
O.K.
OUTPUT
CHIPLOT
FILE NAME
#OUT
O.K.
EXIT
MACROS / LOG FILE

APPENDIX F

Scripts to convert the ASCII files of EDXS maps into PNG files

The compositional maps a recalculated with the software Iridium in *wt.*%. After the recalculation the maps are saved as a ASCII files and converted with ImageJ in to PNG files. The scripts change the picture size and include the scale bare depending on the pixel size of the maps.

F.1 512 pixel wide map

```
dir1 = getDirectory("Choose Source Directory ");
dir2 = getDirectory("Choose Destination Directory ");
list = getFileList(dir1);
setBatchMode(true);
for (i=0; i¡list.length; i++) {
file = dir1 + list[i];
run("Text Image... ", "open=&file");
run("Canvas Size...", "width=572 height=383 position=Top-Left");
run("royal"); // Color Code
run("Calibration Bar...", "location=[Upper Right] fill=None label=Black number=5 decimal=0 font=12 zoom=1");
};
run("Images to Stack", "use");
run("Image Sequence... ", "format=PNG name=Stack start=1 digits=4 use save=[dir2]");
setBatchMode(false);
```

F.2 1024 pixel wide map

```
dir1 = getDirectory("Choose Source Directory ");
dir2 = getDirectory("Choose Destination Directory ");
list = getFileList(dir1);
setBatchMode(true);
for (i=0; i¡list.length; i++) {
```

```
file = dir1 + list[i];
run("Text Image... ", "open=&file");
run("Canvas Size...", "width=1122 height=766 position=Top-Left");
run("royal");
run("Calibration Bar...", "location=[Upper Right] fill=None label=Black number=5 decimal=0 font=12 zoom=2");
};
run("Images to Stack", "use");
run("Image Sequence... ", "format=PNG name=Stack start=1 digits=4 use save=[dir2]");
setBatchMode(false);
```